Biswajeet Panda, David Mazé, Diego Millerand, Lucas Corrêa and Longlong Wang

Reachability–Stability Trade-offs in Rover–Manipulator Systems: The Role of Mobility Architecture

Faculty of Engineering and Applied Sciences
Robotics MSc

Group Project
Academic Year: 2025–2026

Supervisors:
Dr Saurabh Upadhyay,
Dr Leonard Felicetti and
Dr Gilbert Tang

April 2026

Faculty of Engineering and Applied Sciences

Robotics MSc

Group Project

Academic Year: 2025–2026

Biswajeet Panda, David Mazé, Diego Millerand, Lucas Corrêa and Longlong Wang

Reachability–Stability Trade-offs in Rover–Manipulator Systems: The Role of Mobility Architecture

Supervisors:

Dr Saurabh Upadhyay,

Dr Leonard Felicetti and

Dr Gilbert Tang

April 2026

This group thesis is submitted in partial fulfilment of the requirements for the degree of Robotics MSc

Academic Integrity Declaration

I declare that:

- the project submitted has been written by my group.
- the project submitted has not been previously submitted to this university or any other.
- that all content, including primary and/or secondary data, is true to the best of my knowledge.
- that all quotations and references have been duly acknowledged according to the requirements of academic research.

I understand that to knowingly submit work in violation of the above statement will be considered by examiners as academic misconduct.

Contents

List of Figures

List of Tables

List of Abbreviations

ALD	Analytical Laboratory Drawer
APXS	Alpha Particle X-ray Spectrometer
ATHLETE	All-Terrain Hex-Limbed Extra-Terrestrial Explorer
CNSA	China National Space Administration
CoM	Centre of Mass
DH	Denavit–Hartenberg
DOF	Degree(s) of Freedom
EL3	European Large Logistics Lander
ESA	European Space Agency
GAP	Ground Adaption Process
GRF	Ground Reaction Force
IDD	Instrument Deployment Device
ISRO	Indian Space Research Organisation
ISRU	In-Situ Resource Utilisation
JAXA	Japan Aerospace Exploration Agency
JPL	Jet Propulsion Laboratory
MAHLI	Mars Hand Lens Imager
MAV	Mars Ascent Vehicle
MB	Mössbauer Spectrometer
MER	Mars Exploration Rover
MI	Microscopic Imager
MPC	Model Predictive Control
MSL	Mars Science Laboratory
MSR	Mars Sample Return
NASA	National Aeronautics and Space Administration
nFASM	Normalised Force-Angle Stability Measure
PIXL	Planetary Instrument for X-ray Lithochemistry
PSR	Permanently Shadowed Region
RAT	Rock Abrasion Tool
RB	Rocker-Bogie
ROS	Robot Operating System

SHA	Sample Handling Arm
SHERLOC	Scanning Habitable Environments with Raman and Luminescence for Organics and Chemicals
URDF	Unified Robot Description Format
VISPA	Versatile In-Space and Planetary Arm
ZMP	Zero Moment Point

Chapter 1

Introduction

Planetary exploration missions increasingly rely on robotic systems capable of operating in remote, hazardous, and unstructured environments. In particular, renewed interest in lunar exploration, driven by initiatives such as NASA's Artemis program [1], has highlighted the need for robotic systems capable of performing complex surface interaction tasks on the Moon. Among the various robotic platforms proposed for planetary missions, rover–manipulator systems have emerged as a promising solution [2–4]. By combining the mobility of planetary rovers with the dexterity of robotic arms, these systems enable a wide range of surface operations, including scientific sampling, instrument deployment, equipment manipulation, and geological inspection. Previous planetary missions, particularly NASA's Mars rover missions [5], demonstrate how robotic manipulators integrated with mobile platforms can significantly extend the operational capabilities of robotic exploration systems. Despite these advantages, integrating a manipulator onto a mobile rover platform introduces fundamental engineering challenges. Unlike fixed-base manipulators commonly used in industrial environments [6, 7], rover–manipulator systems operate on mobile bases that are not rigidly anchored to the ground. When the manipulator extends to reach distant targets, the overall centre of mass (CoM) of the system shifts relative to the rover's support polygon. If this shift exceeds the stability limits of the platform, tip-over risks may occur. Consequently, the reachable workspace of a rover-mounted manipulator is not determined solely by its kinematic structure, but also by the stability characteristics of the entire rover–manipulator system [8]. The problem becomes even more complex in planetary environments where terrain conditions are highly variable. Sloped and uneven terrain can alter the effective support polygon and change the projection of the system's centre of mass on the ground. Under such conditions, the feasible workspace of the manipulator is constrained not only by the arm geometry but also by terrain-induced stability limits and rover configuration [9]. Therefore, understanding how rover design, manipulator configuration, and terrain conditions jointly influence reachable workspace is essential for the design of robotic systems intended for lunar surface operations. Existing research has investigated several aspects of rover–manipulator systems. A substantial body of work

focuses on planetary rover mobility mechanisms, including wheeled, wheeled–legged, and legged platforms designed to improve terrain adaptability and traversal performance [9,10]. Other studies concentrate on robotic manipulator design and workspace analysis, typically evaluating kinematic reachability or manipulability characteristics of robotic arms [11,12]. In addition, various stability evaluation methods have been developed for mobile robots and mobile manipulators. Geometry-based approaches commonly assess stability by examining the position of the system's centre of mass relative to the support polygon [13,14], while moment-based [15, 16] and contact-force-based [17, 18] methods analyse tipping conditions using force or torque balance. However, these research directions are often investigated independently. Manipulator studies frequently analyse the intrinsic kinematic workspace of robotic arms without considering the influence of rover base geometry or terrain conditions. Conversely, rover stability studies typically analyse tip-over risks for mobile platforms but do not explicitly relate these stability constraints to the reachable workspace of integrated rover–manipulator systems. As a result, there remains limited understanding of how rover configuration, manipulator design, and terrain characteristics interact to determine the feasible workspace that can be safely utilised for manipulation tasks. To address this challenge, this study investigates how rover configuration, manipulator design, and terrain conditions influence the feasible reachable workspace of rover–manipulator systems operating on the lunar surface. A dual-model evaluation framework is proposed. First, a geometry-based stability model is used to determine the stability-constrained reachable workspace of the system. Second, a moment-based model is introduced to estimate the load tolerance associated with interaction tasks. Using this framework, different rover–manipulator configurations are analysed under representative terrain conditions, and their reachable workspace is quantified in terms of characteristic length, area, and volume while accounting for self-occlusion caused by the rover structure. The proposed approach provides a systematic basis for comparing rover–manipulator configurations and for understanding the trade-offs between reachability, stability, and operational capability in planetary robotic systems.

Chapter 2

Literature Review

This chapter reviews the technical foundations underpinning the design and evaluation of planetary mobile manipulator systems, with particular emphasis on the coupled relationship between mobility platform, manipulator architecture, and static stability. The central research question addressed by this study — *which combination of planetary mobility mechanism, arm configuration, and base placement maximises the reachable workspace while maintaining static stability on representative terrain?* — requires a synthesis of knowledge spanning rover mobility, robotic manipulation, and stability analysis. The review is therefore structured around five complementary themes.

Section 2.1 examines wheeled rover platforms, tracing the evolution from Sojourner to Perseverance and establishing the rocker-bogie suspension as the dominant flight-proven mobility architecture. The discussion addresses how arm mounting location and chassis geometry influence both workspace and platform stability during manipulation tasks.

Section 2.2 extends the mobility review to wheeled-legged (wheel-on-limb) platforms such as ATHLETE and SherpaTT, which offer actively reconfigurable support polygons and the potential for limbs to serve dual roles as both locomotion and manipulation elements. These platforms are of particular interest for missions requiring traversal of steep or irregular terrain prior to manipulation.

Section 2.3 considers fully legged platforms, reviewing quadruped-arm systems such as Boston Dynamics Spot with integrated manipulators. The discussion highlights how whole-body coordination — exploiting the base's locomotion DOF as additional manipulation DOF — can extend the feasible reachable workspace well beyond the arm's intrinsic kinematic limit.

Section 2.4 reviews the evolution of planetary rover manipulators from the 0.8 m MER Instrument Deployment Device to the 2.1 m Perseverance arm and the 7-DOF Airbus VISPA concept. Key topics include serial kinematic architecture, manipulability metrics, automated base placement algorithms, whole rover–arm coordination, and the emerging requirement for assembly- and construction-class arms at the Lunar South Pole.

Section 2.7 presents the stability evaluation framework adopted in this study. Three

classes of stability criteria are reviewed — geometry-based, moment-based, and contact-force-based — with a comparative synthesis justifying the selection of geometry-based stability margins as the primary metric for the quasi-static reachability analysis developed in subsequent chapters.

2.1 Planetary Mobility Mechanisms - Wheeled Platform

Planetary exploration has been driven by the development of various types of rovers, which vary significantly in complexity, size, and scientific instrumentation. However, despite this diversity of designs, they all share the common characteristic of movement by means of wheels, a system that has consolidated itself as the most efficient for facing the challenges of locomotion in irregular terrains and low gravity [19]. The technical evolution of these vehicles, from the first missions to the most modern concepts, can be observed in Table 2.1.

Table 2.1: Main space exploration rovers from 1997 onwards.

Name	**Institution**	**Size (m^3)**	**Weight (kg)**	**Wheels**	**System**	**Speed (cm/s)**	**Year**
Sojourner	JPL (NASA)	0.65×0.48×0.3	11	6	RB	0.1	1997
Spirit/Opp.	JPL (NASA)	2.3×1.6×1.5	174	6	RB	1	2004
Curiosity	JPL (NASA)	2.9×2.7×2.2	900	6	RB	5	2012
Yutu	CNSA	1.5×1.0×1.1	136	6	RB	5.5	2013
Polaris	Astrobotic/NASA	1.67×2.13×2.43	150	4	Diff.	30	2015
Chandrayaan-2	ISRO/Roscosmos	0.6×0.5×0.4	20	6	RB	10	2017
ExoMars	ESA/Roscosmos	1.2×1.1×2.0	219	6	3B	1	2018
Mobile MAV	NASA	2.7×3.0×2.2	1050	6	RB	-	2020
MELOS	JAXA	1.2×1.0×0.5	150	6	3B	0.75	2020
Perseverance	JPL (NASA)	3.0×2.7×2.2	1025	6	RB	4.2	2021

Sources: [19, 20].

Where: RB is Rocker-Bogie; 3B is Three-Bogie; and Diff means Differential.

The selection of a robotic platform must take into account that the objective is a Sample Return (SR) mission, which requires capabilities far beyond simple in situ analysis. In this context, the rover is responsible for complex operations such as sample extraction, containment, and the final transfer for orbital ascent. While several strategies exist to address these needs, including the use of small rovers for quick collection or larger integrated science platforms, there is a clear requirement for a highly autonomous vehicle capable of precise retrieval and encounter [21].

Table 2.2: Comparative Analysis of Rover Categories: Mass, Mobility, and Robotic Arm Constraints.

Category	**Mass Range**	**Pros**	**Cons**	**Arm & Payload Impact**
Small	0 – 100 kg	1. Minimal launch cost and volume. 2. Low ground pressure (minimal sinkage). 3. High agility in confined terrains.	1. Critical susceptibility to tip-over. 2. Extremely limited power budget. 3. Poor obstacle clearance (H_{obs}).	**Restricted:** Reach is limited by the narrow wheel track. Torque from the arm can easily lift opposing wheels.
Medium	100 – 900 kg	1. Proven reliability for long-term missions. 2. Optimal balance of payload vs. cost. 3. High energy harvest via solar/RTG.	1. Increased mechanical complexity. 2. Higher risk of wheel entrapment. 3. Moderate thermal control demands.	**Versatile:** Chassis mass acts as a stable counterweight. Supports multi-DOF arms with moderate payload (1-5 kg) and 1.5m reach.
Large	900+ kg	1. Superior stability for drilling/sampling. 2. Maximum obstacle/ditch negotiation. 3. All-weather operational capability.	1. Extreme EDL (Entry/Descent/ Landing) risk. 2. High power consumption for actuators. 3. Maximum footprint and logistics cost.	**Robust:** High inertial resistance allows for high-speed arm movements and heavy-duty tools without compromising the Static Stability Margin (SSM).

Based on the categorical trade-offs presented in Table 2.2, the rovers from the historical survey were grouped to establish the boundary conditions for the parametric scaling analysis. For this analysis, the Polaris (Astrobotic) was excluded as it utilizes a four-wheeled differential suspension, which deviates from the six-wheeled trend that defines the majority of successful deep-space missions. To maintain a fidedign scaling process, a consistent 6-wheeled Rocker-Bogie morphology was prioritized, ensuring that the geometric stability polygon remains proportional across all mass classes.

Each category is represented by a benchmark rover that defines the operational expectations for the simulations:

- **Small-Class Representative:** The *Sojourner* (11 kg) is elected to represent the

lower bound. It serves as the baseline for small-class simulations, where the robotic arm's mass and movement have the most significant impact on the vehicle's Static Stability Margin (SSM).

- **Medium-Class Representative:** The *Spirit/Opportunity* (174 kg) rovers represent the medium-class standard. They provide the ideal baseline for balancing payload capacity with landing complexity, serving as the primary reference for the initial CAD model.

- **Large-Class Representative:** The *Perseverance* (1025 kg) is the chosen platform for the heavy-class analysis. As the current state-of-the-art in planetary robotics, it justifies the requirement for a high-mass chassis to provide the necessary inertial anchorage for heavy-duty sampling and high-torque arm operations.

Research indicates that a comparative evaluation of robotic mobility in lunar environments requires a rigorous standardization approach, as the mass disparity between platforms ranging from 10 kg nanorovers to 1000 kg heavy exploration vehicles prevents direct comparisons without proper dimensional and inertial scaling. This standardization is essential to isolate the mechanical performance of different suspension morphologies, allowing for the identification of how each design responds to vertical obstacle negotiation and incline progression under reduced gravity. There is a documented necessity to perform static and quasi-static simulations to determine the geometric and torque limits of each system, evaluating the capability to overcome obstacles such as steps and rocks and the integrity of the stability polygon during the crossing of ditches or cratered terrain. These numerical and laboratory simulations are crucial to define the operational envelope of the robot, ensuring that stability is maintained even when the Center of Mass (CoM) is displaced by severe slopes or the operation of robotic appendages on the lunar surface [9].

STILL NEED TO ADD SOJOUNER AND SPIRIT LITERATURE REVIEW

The Perseverance rover represents an exceptional platform for planetary exploration due to its high operational efficiency and advanced autonomy, which were consolidated during its extended mission in Jezero Crater. The vehicle stands out for its use of the AutoNav system, which enables autonomous navigation through complex terrains with minimal human intervention, breaking distance and speed records compared to previous missions. Additionally, its mechanical robustness and strategic route planning capabilities optimize the time available for scientific activities, allowing for the safe and technically precise exploration of high-interest geological areas, such as an ancient river delta [22].

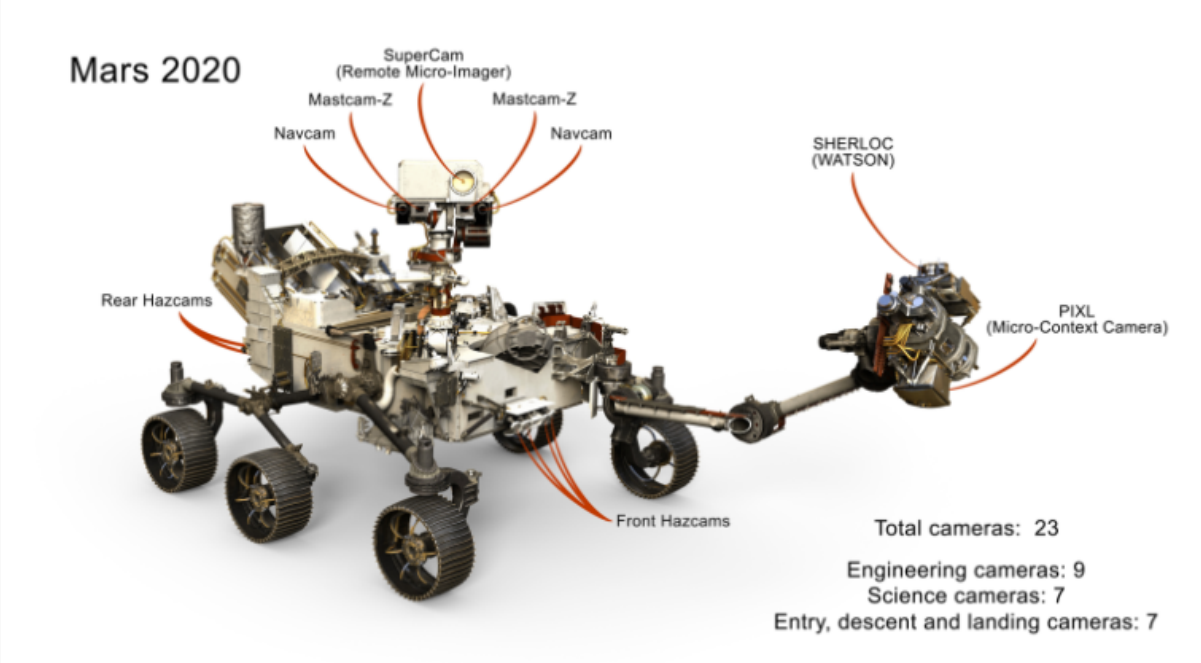

Figure 2.1: Perseverance rover.

Source: [20].

To fulfill its sample collection function, the robot is equipped with a 2.1-meter-long robotic arm that enables the millimeter-level positioning of scientific instruments on irregular rocky surfaces. This system includes a rotary-percussive drill capable of extracting sedimentary and igneous rock cores, which are then processed by the internal Sample Handling Arm (SHA) to be hermetically sealed in titanium tubes. The versatility of this robotic suite was further demonstrated by the creation of sample depots on the surface, ensuring that the collected material is organized and accessible for the future stages of a sample return mission to Earth [22].

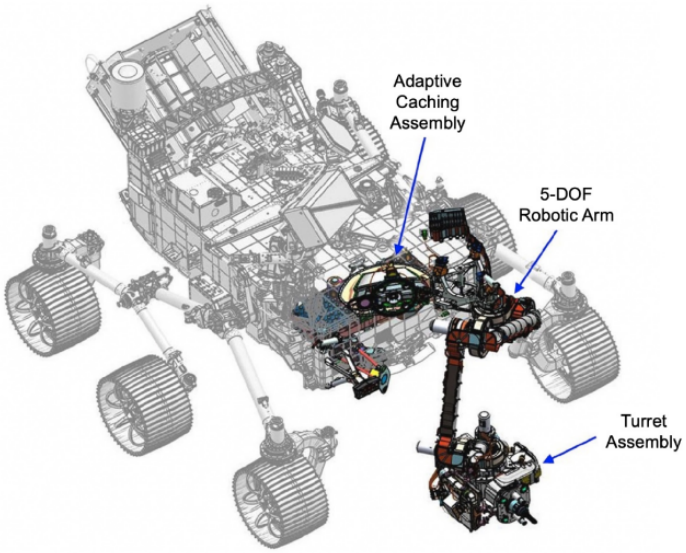

Figure 2.2: Perseverance robotic arm.

Source: [22].

The mechanical architecture of the robotic arm is further characterized by a five-actuator configuration separated by titanium links, utilizing brushless DC motors and friction brakes for precise positioning. At its distal end, a redundant force torque sensor enables closed-loop load applications and monitors for inadvertent contact during operations. The turret assembly serves as the primary interface for surface interaction, housing a rotary percussive coring drill designed for both rock abrasion and the extraction of regolith samples. To ensure accuracy, a facility contact sensor facilitates improved placement while the gas dust removal tool employs compressed nitrogen to clear debris from scientific targets. Beyond sampling, the turret integrates high-resolution instruments such as PIXL, which uses an articulated hexapod to compensate for thermal drift, and SHERLOC, which provides spatially resolved chemical maps. Once a core is acquired, the arm docks the corer against a bit carousel to initiate further processing within the adaptive caching assembly located inside the rover chassis [23].

The stability of a combined mobile platform and robotic arm is a critical factor for planetary exploration because shifts in the Center of Mass (CoM) during manipulation can compromise the entire system. Implementing a six-wheeled configuration with a rocker-bogie suspension system provides a robust foundation to mitigate tip-over risks on irregular terrains and steep slopes. Positioning the robotic arm at the front of the chassis optimizes the Zero Moment Point (ZMP) and maintains a safe stability margin even at maximum reach. This strategic layout ensures the dynamic balance required for high-precision drilling and sampling across diverse environments without the need for heavy or complex passive stabilization devices [24].

The strategic definition of the manipulator mounting point on the Perseverance chassis is fundamental to maximizing mission effectiveness, as reach and dexterity are directly

influenced by the kinematic structure and the location of the arm base [25]. As indicated by capability and reachability map analyses, positioning the arm at the front and bottom of the robot optimizes the useful workspace for ground interaction tasks, allowing the manipulator to access regolith samples with greater orientation freedom and lower risk of kinematic singularities [26]. If the arm were installed on the upper part of the rover, the effective workspace for ground collection would be severely reduced, as a significant portion of the manipulator's reach would be consumed simply to bypass the vehicle's own structure, creating shadow zones caused by collisions with the robot body [27]. Therefore, the low frontal mounting minimizes these geometric constraints, ensuring that the maximum reach volume coincides with the area of greatest scientific interest on the Martian surface.

2.2 Planetary Mobility Mechanisms - Wheeled-legged Platform

Wheeled-legged, or "wheel-on-limb," robots attempt to leverage the benefits of wheeled mobility while also achieving the terrability and posturability of a legged robot, thus making them promising solutions for maximizing the manipulator workspace while adhering to static stability constraints on rough planetary terrain. These robots are differentiated from rocker-bogie or skid-steer architectures in that the legs are positioned between the chassis and each wheel, thus allowing the points of wheel contact to be moved to maintain a large support polygon and a favorable body posture while approaching a scientific target [28], [29], as shown in Figure 2.3. This section briefly discusses some of the key planetary-relevant wheeled-legged robots, including associated design studies, with respect to their structural and/or control aspects that facilitate stable locomotion.

Figure 2.3: SherpaTT in its final integration state.

Early research by Wilcox and co-authors on the ATHLETE (All Terrain Hex Limbed Extra Terrestrial Explorer) rover proposed the concept of a six-limbed wheel-on-leg

design, with the explicit purpose of lunar cargo handling and manipulation [30], [31]. The ATHLETE limb is described as a 6-DoF manipulator with a powered wheel at the end, allowing for efficient wheel-based motion on moderate terrain or for quasi-static walking on extreme slopes and vertical stairs up to 50–70% of the stowed body length, or roughly twice the height of the step for MER-class rovers. Note, as Wilcox et al. discuss, the wheel-on-leg design enables the vehicle to transition from high-speed wheel motion to statically stable walking when wheel thrust is insufficient, directly increasing the number of terrain configurations from which a tool, such as a limb or arm, is able to safely operate (see Figure 2.4).

Figure 2.4: Wheeled-legged ATHLETE rover.

Cordes and co-authors have also generalized this "wheel on limb" concept in the family of hybrid wheeled-legged robots called the Sherpa and SherpaTT robots, developed for lunar logistics and cooperative exploration within the TransTerrA and RIMRES missions [28], [29], [32]. The original Sherpa robot is equipped with four legs with flexible wheels and a multi-purpose manipulator; the suspension system is able to vary the height from fully "belly-down" contact with the terrain to a maximum of 711 mm, and even achieve "negative ground clearance" by lifting the wheels off the ground while the body is in contact with the terrain. Cordes and Babu generalize this design to four identical 5-DoF suspension systems arranged around a central body, forming a toroidal leg workspace from which the preferred pose is chosen to optimize vertical wheel travel, balance vertical and radial reach, or optimize height of the body. Experiments with SherpaTT's Ground Adaption Process (GAP) indicate how force levelling and control of roll and pitch motions may reduce single wheel load deviations from ±300 N to ±50 N and body attitude deviations to about ±0.5° over 0.2 m obstacles, and how such active suspensions may maintain static stability as the pose of the chassis is altered to extend the manipulator's reach (see Figure 2.5).

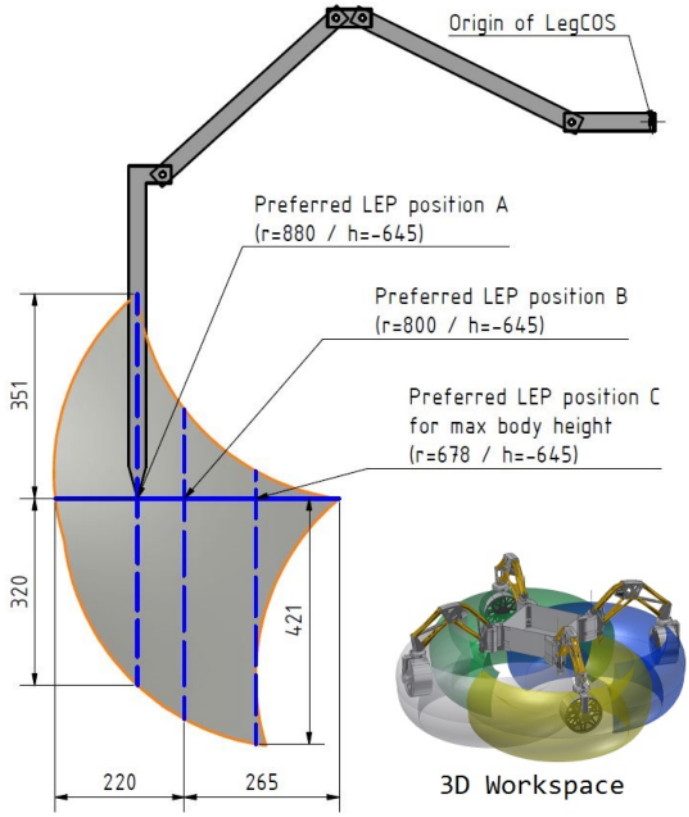

Figure 2.5: Workspace dimensions cross section and preferred poses in cylindrical leg frame.

Source: [29].

These concepts have been taken to the next level for autonomous planetary operation by Reid and co-workers, who investigate actively articulated wheel-on-limb robots over Europa analogue terrain and other rough terrain types [33],. In their experiments over their Europa analogue terrain, Reid et al. employed a wheel-on-limb rover with four limbs, employing multi-objective control to maintain wheel contact, control body attitude, and prevent suspension saturation over steep, blocky terrain, demonstrating that proprioceptive control alone is sufficient to maintain the body nearly level and all wheels in contact, even over very irregular terrain. In a comparative study, Webster and Reid simulate, via a high-fidelity dynamics simulator, simplified versions of RoboSimian, referred to as "WOLVERINE," and ATHLETE, referred to as "MATHLETE," and show that actively articulated wheel-on-limb robots have superior traversability over large step and crater rim terrain types compared to rocker-bogie and wheel-on-leg robots, especially at higher masses, though with higher energy consumption over easier terrain types [9],(see Figure 2.6). The findings indicate that wheeled-legged platforms have their greatest utility for missions where extreme terrain must be crossed to deploy instruments or sampling systems, which is similar to the reach vs. stability trade-off currently considered by this project.

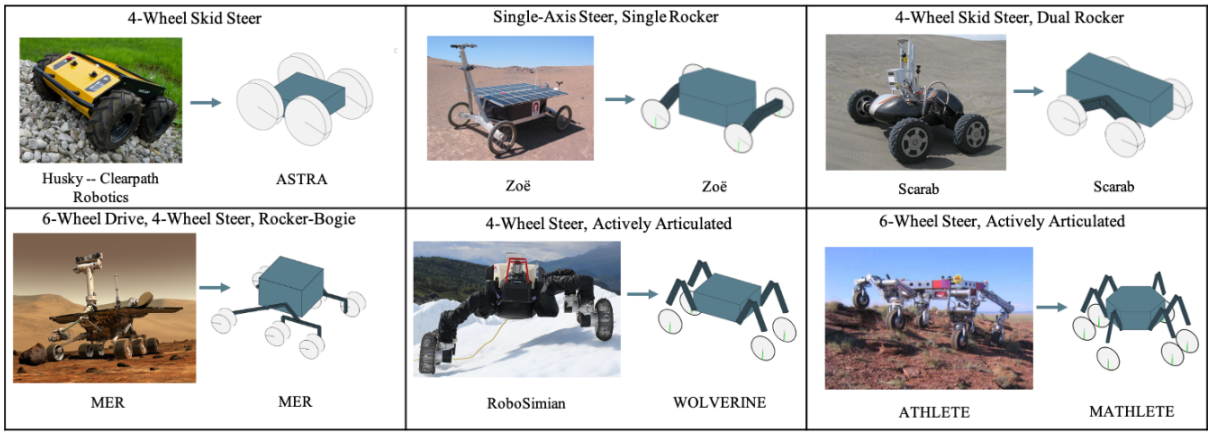

Figure 2.6: Six mobility systems used in this study.

Source: [9].

Aside from particular prototypes, many works deal with the design and optimization of wheeled-legged suspensions. Cordes et al. provide an overview of the original Sherpa suspension and introduce an alternative design with a "knee" joint in each of the legs, removing the rarely utilized wheel tilt/flip DOFs and decoupling the steering of the wheels from their placement during contact to allow for more independent vertical motion [28] (see Figure 2.7). Zhu et al. introduce a stiffness optimization framework for a terrain-adaptive wheeled-legged rover, in which performance indices for deformation, load-carrying capacity, energy efficiency, and dynamic stability are introduced, and performance atlases are utilized to adjust the active and passive compliance of the rover in order to ensure stability during adaptation to rough terrain [34].

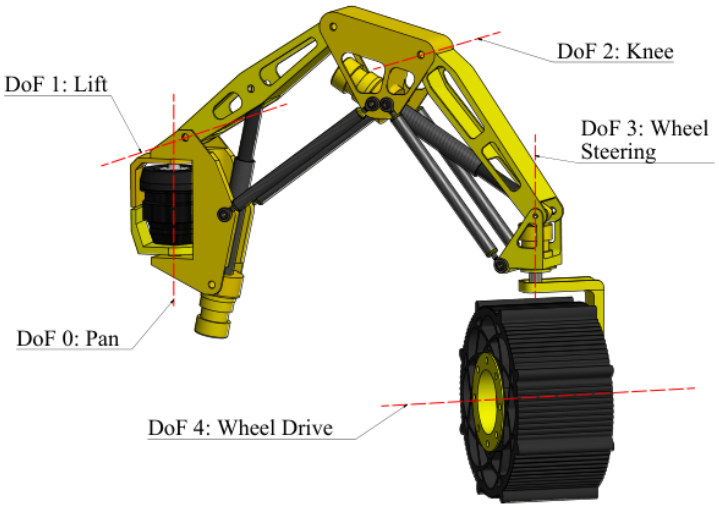

Figure 2.7: New leg design for Sherpa based on two serial-aligned parallel kinematics.

Source: [28].

Wheeled-legged mobility must also be understood in the context of rover-arm co-ordination. Townsend, Biesiadecki, and Collins demonstrate that the versatility of the

ATHLETE robot enables the wheel-on-legs to also function as manipulator arms, for instance, by attaching tools to the wheel hub [35]. SherpaTT also enables the combination of an active suspension system, a manipulator arm, and modular payload interfaces, which enables the adjustment of the posture of the legs, the footprints, and the body position so that the science tools or payloads remain in the arm's reach, yet also have an advantageous support polygon. Together with the placement of the base, as for instance developed by Backes et al. for the Rocky 8 robot, the additional degrees of freedom make the wheeled-legged platforms particularly interesting for the maximization of the reachable workspace under static stability constraints [36].

2.3 Planetary Mobility Mechanisms - Legged platform

Legged robots have emerged as a compelling alternative to conventional wheeled rovers for planetary surface exploration, owing to their superior adaptability to unstructured and steep terrain. Unlike wheeled systems, which are constrained by continuous ground contact and limited obstacle clearance, legged platforms can actively reconfigure their support polygon, step over rocks, traverse granular slopes, and access confined environments such as lava tubes and crater rims that remain inaccessible to traditional rover designs [37, 38]. Field deployments in planetary analogue environments have demonstrated that legged robots can maintain stable locomotion on granular slopes exceeding 25° and loose soil conditions representative of Martian and lunar regolith [37]. Furthermore, the integration of robotic arms onto legged platforms introduces a unified loco-manipulation capability — enabling a single system to both navigate and interact with the environment — which is identified across recent literature as the most promising architecture for next-generation planetary exploration missions [39, 40].

2.3.1 Structural and Geometric Review

The integration of robotic arms onto mobile legged platforms has emerged as a primary strategy for extending manipulation capability in unstructured environments. Across five state-of-the-art studies reviewed in this work, quadruped-arm systems demonstrate that whole-body coordination — exploiting the base's mobility as additional degrees of freedom — consistently outperforms fixed-base arm deployment in terms of reachable workspace, terrain adaptability, and task success rate [39–43]. The reviewed platforms span a spectrum of structural complexity: from the 18-DOF Unitree B1/B2 paired with the Unitree Z1 arm [40, 41], the 19-DOF HyQReal platform with the Kinova Gen3 manipulator [42], and the 18-DOF Boston Dynamics Spot with its integrated Spot Arm [39], to the highly

redundant 37-DOF CENTAURO equipped with bilateral 7-DOF arms [43]. Each platform embodies a distinct structural philosophy — ranging from lightweight minimalism to full kinematic redundancy — and the geometric relationship between the arm mount point, the torso frame, and the leg support polygon is identified across all five works as the primary determinant of operational workspace [39, 43].

2.3.2 Definition of a Representative Model

For the purposes of this review, Boston Dynamics Spot with the Spot Arm — as deployed in the ReLIC framework [39] — is selected as the representative platform. Spot's body is modelled as a rigid rectangular torso with a length of 1,100 mm, width of 500 mm, and a variable height range of 340–620 mm achieved through leg extension [44]. Unlike purely wheeled platforms, Spot's four articulated legs provide a dynamically reconfigurable support polygon, allowing the effective base footprint to be adapted in real time [39]. Each leg comprises three actuated joints — hip abduction-adduction, hip flexion-extension, and knee flexion-extension — contributing 12 leg DOF that provide continuous control over body height, pitch, roll, and lateral displacement [44]. The Spot Arm attaches to the front face of the torso via a fixed rigid mount, contributing 6 additional DOF with a total arm mass of approximately 8 kg [45]. This front-integrated configuration — distinct from the top-back mounts adopted in [40–42] — places the arm's natural workspace directly forward of the robot's primary direction of travel, aligning manipulation capability with the locomotive heading [39].

2.3.3 Selection of a Representative Manipulator

The Spot Arm is a 6-DOF serial manipulator with a maximum reach of 984 mm, the longest of any arm across the five reviewed platforms, and a peak payload capacity of 11 kg, the highest single-arm figure in the group [45]. The end-effector is a parallel jaw gripper with a 175 mm aperture and a 130 N peak tip force, capable of grasping rock core tubes, instrument handles, and geological surface samples [45]. Kinematic analysis identifies the arm as operating in an elbow-up, forward-biased configuration, producing a hemispherical reachable volume predominantly in front of and below the torso mount point [39]. While the 6-DOF design lacks the kinematic redundancy of the 7-DOF Kinova Gen3 used in RAKOMO [42] — meaning singularity avoidance requires base motion rather than internal elbow reconfiguration — this limitation is precisely what ReLIC's leg-reassignment framework resolves through dynamic whole-body coordination [39]. This design choice is further supported by planetary analogue field trials, which similarly identify base mobility as the primary mechanism for extending arm reach on mass-constrained platforms operating in unstructured terrain [37].

Figure 2.8: Boston Dynamics Spot with the integrated 6-DOF Spot Arm performing a contact manipulation task — the hardware platform deployed in the ReLIC loco-manipulation framework. The front-mounted arm configuration provides a 984 mm reach envelope directly aligned with the robot's locomotive heading.

Source: [39].

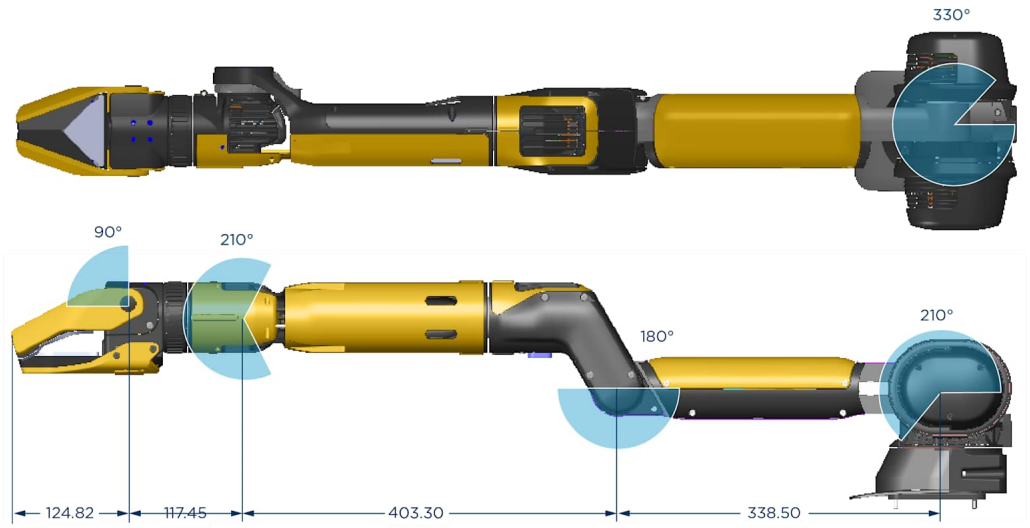

Figure 2.9: Boston Dynamics Spot Arm — a 6-DOF serial manipulator with 984 mm maximum reach, 11 kg payload capacity, and a parallel jaw gripper with 175 mm aperture and 130 N peak tip force.

Source: [45].

2.3.4 Static Stability Modelling

Static stability of the Spot-ReLIC system is maintained through continuous redistribution of ground reaction forces (GRFs) across the active stance legs [39]. The support polygon — defined as the convex hull of active foot contact points — must contain the system's projected Centre of Mass (CoM) for static stability to be guaranteed [43]. When the Spot Arm is fully extended at 984 mm, the CoM shifts approximately 80–120 mm forward of the nominal torso centre, narrowing the anterior stability margin [39, 45]. ReLIC's reinforcement learning-trained locomotion policy compensates by dynamically shifting rear leg stance positions rearward, restoring the CoM projection within the support polygon without operator input [39]. In tripod and biped stances — adopted when a leg is reassigned as a manipulator — the support polygon contracts significantly, and stability is maintained via higher GRF magnitudes on the remaining stance legs, a behaviour validated across surfaces including stairs, slopes, and granular terrain [39]. This approach contrasts with the model-based MPC formulation of [41], where GRF limits are enforced as hard constraints at every solver node, and with the hydraulic joint stiffness strategy of [42], which relies on passive resistance rather than active redistribution. The effectiveness of active stability management during manipulation has also been demonstrated in planetary analogue field trials, where legged robots maintained balance on granular slopes exceeding 25° [37].

2.3.5 Feasible Reachable Workspace

The feasible reachable workspace of the Spot-ReLIC system extends substantially beyond the arm's intrinsic 984 mm kinematic limit through three complementary mechanisms. First, variable body height across a 280 mm range shifts the arm mount point vertically, extending the reachable volume upward and downward without any arm joint motion [41, 44]. Second, torso pitch and roll of up to ±15° project the arm mount point forward or laterally, extending horizontal reach by approximately 90–160 mm depending on body height [41]. This torso-tilt strategy is most explicitly demonstrated in [41], where the MPC solver automatically pitches the torso toward out-of-reach targets as a soft-penalty minimisation behaviour, projecting the arm mount approximately 100–130 mm further forward under a 10–12° pitch. Third, and uniquely among the five reviewed platforms, leg reassignment in ReLIC allows one or more legs to contact, brace against, or manipulate objects in directions entirely outside the Spot Arm's kinematic envelope — including directly behind the robot, laterally at body height, and below the belly plane [39]. Collectively, these mechanisms produce an effective system workspace approaching 360° omnidirectional coverage across a height range of 0–1,800 mm, compared to the arm-only forward hemisphere of approximately 984 mm radius [39]. This omnidirectional, multi-mechanism workspace is the most comprehensive of all five reviewed platforms and represents the most viable

configuration for planetary exploration tasks — including crater rim sampling, boulder face contact, and lava tube entry — where target geometry and base mobility constraints are inherently unpredictable [37, 38].

2.4 Planetary Mobility Mechanisms – Manipulator

Robotic manipulation constitutes a core capability for planetary surface missions, enabling tasks ranging from instrument placement and surface preparation to sample acquisition and transfer. The functional requirements imposed on planetary manipulators differ substantially from those of terrestrial industrial robots: the design must simultaneously minimise mass and volume, tolerate extreme thermal cycling and radiation, operate under significant communication delays, and provide sufficient dexterity and reach to interact with geologically diverse targets on irregular terrain [46]. This section reviews the evolution of rover-mounted manipulator systems, examines their principal kinematic and mechanical characteristics, and discusses the implications of arm configuration for whole-rover coordination and reachability.

2.4.1 Serial Kinematic Architecture and Design Drivers

All planetary manipulators flown to date employ open serial kinematic chains, in which rigid links are connected sequentially through revolute joints from a fixed base to an end effector [47]. This architecture is favoured for planetary applications because it offers a large workspace relative to the stowed volume, permits straightforward forward and inverse kinematic analysis, and allows modular integration of instruments at the distal end. The fundamental kinematic relationship between the joint variable vector $\mathbf{q} \in \mathbb{R}^n$ and the end-effector pose $\mathbf{r} \in \mathbb{R}^m$ is described by

$$\mathbf{r} = f(\mathbf{q})$$

where f denotes the forward kinematic mapping, typically parameterised using the Denavit–Hartenberg convention [47]. The differential relationship $\dot{\mathbf{r}} = \mathbf{J}(\mathbf{q})\,\dot{\mathbf{q}}$, governed by the manipulator Jacobian $\mathbf{J}(\mathbf{q})$, provides the basis for workspace analysis and manipulability evaluation, as discussed in Section 2.5.1.

The principal design drivers for planetary manipulators include reach (the distance from the arm base to the farthest reachable point), payload capacity (the mass of instruments and tools at the end effector), positioning accuracy, stiffness, and stowed volume [46]. These requirements are inherently competing: increasing reach demands longer links, which reduces stiffness and increases mass, while adding degrees of freedom enhances dexterity but introduces additional actuators, cabling, and failure modes. Consequently,

the number of DOF in NASA Mars rover manipulators has consistently been five – from the MER IDD through to the Perseverance arm – representing a practical compromise between dexterity and system complexity [48, 49]. The earlier Sojourner rover (Mars Pathfinder, 1997) did not carry a multi-DOF manipulator arm.

2.4.2 Evolution of Planetary Rover Manipulators

The progression of manipulator systems deployed on planetary surfaces reflects a consistent trend toward greater reach, payload capacity, and task complexity. Table 2.3 summarises the key specifications of the principal rover-mounted arms.

Table 2.3: Comparison of planetary rover manipulator systems.

Mission	**Rover**	**DOF**	**Reach (m)**	**Arm Mass (kg)**	**Payload (kg)**	**Year**
Mars Pathfinder	Sojourner	–	–	–	–	1997
MER	Spirit / Opportunity	5	0.8	4.0	2.0	2004
MSL	Curiosity	5	2.2	67	34	2012
Mars 2020	Perseverance	5	2.1	–	–	2021
ExoMars	Rosalind Franklin	2*	–	–	–	2028†
Concept / non-flown systems						
VISPA	– (Airbus, concept)	7	–	–	–	2022‡

* Drill positioning system with 2 DOF; no general-purpose arm. † Planned launch. ‡ URDF released; not yet flown. Perseverance arm mass and payload mass not reported in publicly available NASA specifications.

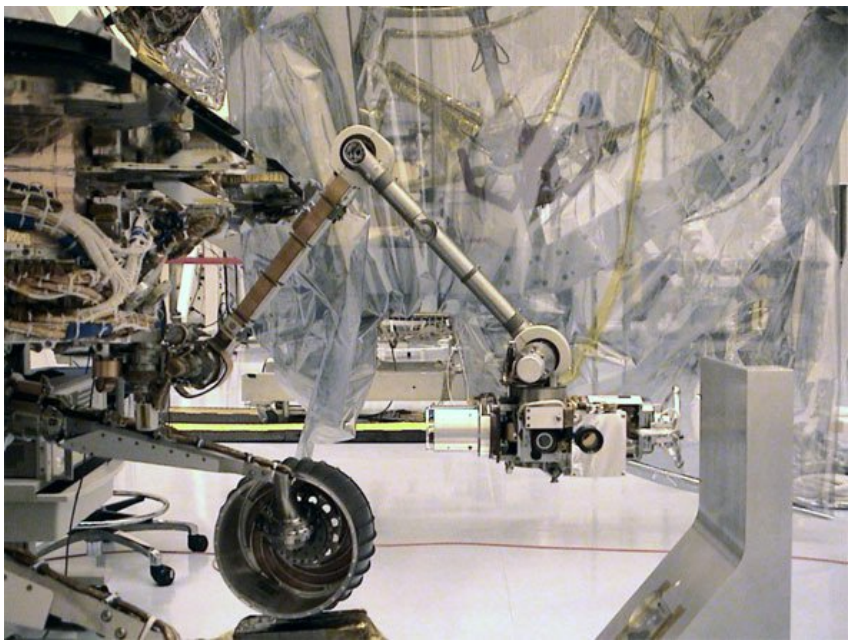

Figure 2.10: The Mars Exploration Rover Instrument Deployment Device (IDD), a 5-DOF serial manipulator carrying four instruments at its turret.

Source: [48].

2.4.2.1 Mars Exploration Rover – Instrument Deployment Device

The Mars Exploration Rovers, Spirit and Opportunity, were equipped with a five-degree-of-freedom Instrument Deployment Device (IDD), representing the first truly dexterous manipulator operated on another planetary surface [48]. With a reach of approximately 0.8 m and a total arm mass of only 4 kg, the IDD was designed to position a 2 kg payload of contact instruments – including the Mössbauer Spectrometer (MB), Alpha Particle X-ray Spectrometer (APXS), Microscopic Imager (MI), and Rock Abrasion Tool (RAT) – against rock and soil targets [50]. The five joints comprised two at the shoulder (azimuth and elevation), one at the elbow, and two at the wrist, providing sufficient workspace for the rover's frontal hemisphere while remaining compact enough to stow within the chassis envelope during traverse [48]. Instrument placement was achieved with a repeatability of approximately 1 mm in position and 1 degree in orientation, a performance level that enabled systematic geochemical characterisation across hundreds of targets throughout the extended mission [50].

2.4.2.2 Mars Science Laboratory – Curiosity Robotic Arm

The Curiosity rover significantly expanded the capability of rover-mounted manipulation through a substantially larger 5-DOF robotic arm with a reach of 2.2 m and a total arm mass of 67 kg, carrying a 34 kg instrument turret [49]. The titanium arm structure incorporates two joints at the shoulder, one at the elbow, and two at the wrist, connected by an upper arm link and a forearm link. A critical innovation was the integration of a percussive drill capable of extracting powdered rock samples from the Martian surface, along with a sample scoop, a brush, the MAHLI camera, and the APXS spectrometer [49]. Unlike the MER IDD, which only placed instruments in contact with the surface, the Curiosity arm actively applies loading during drilling operations. This requirement introduced additional challenges related to structural stiffness, force transmission through the arm, and stability of the rover platform during contact tasks. The arm's electrical cabling system routes over 900 signals from the rover body to the turret instruments through a single-piece flexible printed circuit spanning approximately 10 m in length [49].

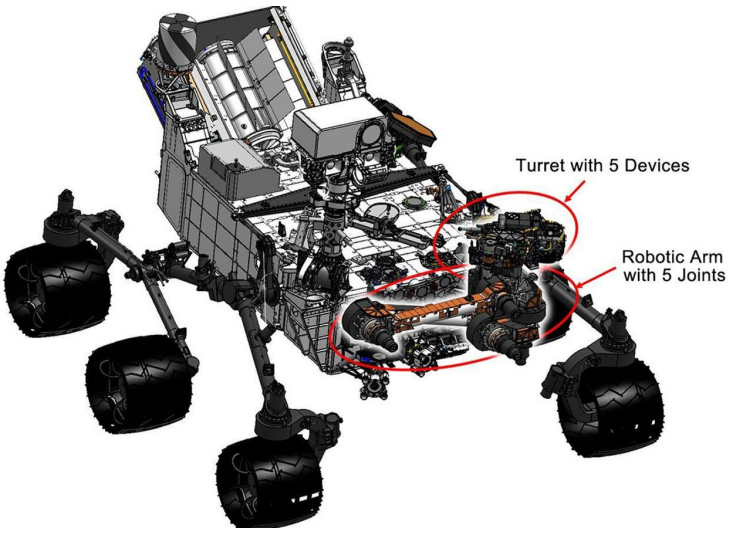

Figure 2.11: Engineering diagram of the Curiosity robotic arm showing the 5-DOF joint configuration and turret-mounted instruments.

Source: [49].

2.4.2.3 Mars 2020 – Perseverance Robotic Arm

As introduced in the discussion of the Perseverance platform (Section 2.1), the rover carries a 2.1 m robotic arm with a five-actuator configuration separated by titanium links [23]. Building on the Curiosity heritage, the arm incorporates a rotary-percussive coring drill designed to extract intact cylindrical rock cores for hermetic sealing in titanium sample tubes. A redundant force-torque sensor at the wrist enables closed-loop load application and monitoring for inadvertent contact, while a facility contact sensor improves placement accuracy on irregular surfaces [23]. The turret assembly further integrates the PIXL and SHERLOC spectrometers, each with their own precision positioning mechanisms. Once a core is acquired, the arm docks the corer against a bit carousel to initiate further processing within the rover's adaptive caching assembly [22]. The combined complexity of drilling, sample handling, and multi-instrument positioning makes the Perseverance arm the most functionally sophisticated manipulator yet deployed on a planetary surface.

2.4.2.4 ExoMars – Rosalind Franklin Drill System

The Rosalind Franklin rover adopts a fundamentally different approach to surface interaction compared to NASA's arm-centric designs. Rather than a general-purpose serial manipulator, the rover employs a dedicated drill system mounted on a two-degree-of-freedom positioning mechanism at the front of the chassis [51]. This system is specifically designed to acquire subsurface core samples from depths of up to 2 m, penetrating beneath the radiation-damaged surface layer where organic molecules and potential biosignatures may be better preserved [51]. The drill uses a rotary-translational action combined with extension rods to reach the required depth, and delivers samples to an internal analytical

laboratory through a dedicated sample handling chain. While the ExoMars approach sacrifices the general-purpose dexterity of a multi-DOF arm, it provides unique access to the deep subsurface environment that no other rover manipulator can achieve.

Figure 2.12: The ExoMars Rosalind Franklin rover with the drill unit visible at the front of the chassis.

Source: [51].

2.4.3 Beyond Exploration: Manipulators for Planetary Assembly and Construction

The preceding subsections have focused on manipulators designed primarily for scientific exploration tasks such as instrument placement and sample acquisition. However, emerging mission architectures for the Lunar South Pole and beyond envision mobile manipulators performing assembly, construction, and in-situ resource utilisation (ISRU) tasks that impose substantially different requirements on arm design [31]. These operations – including habitat module assembly, solar panel deployment, regolith handling, and infrastructure maintenance – demand larger payloads, greater reach, higher DOF for obstacle avoidance, and the ability to apply sustained forces over extended work cycles.

2.4.3.1 The Airbus VISPA Arm

A notable development in this direction is the Versatile In-Space and Planetary Arm (VISPA), developed by Airbus Defence and Space [52]. VISPA is a seven-degree-of-freedom serial manipulator designed to support a broad range of orbital and planetary surface tasks, including in-space manufacturing, satellite assembly, active debris removal, and surface construction operations. The additional seventh DOF, compared to the five-DOF arms on NASA Mars rovers, provides kinematic redundancy that enables the arm to reach targets while simultaneously avoiding obstacles or optimising joint configurations for force

application – a critical capability for construction tasks in cluttered or partially assembled environments.

From a practical standpoint, Airbus has released the VISPA URDF (Unified Robot Description Format) as an open-source package with full mesh geometry and modified Denavit–Hartenberg parameters, compatible with both ROS 1 and ROS 2 [53]. This publicly available model enables direct integration into the ROS 2-based simulation environment being developed in this study, making VISPA a strong candidate arm for the comparative reachability analysis alongside exploration-focused 5-DOF configurations.

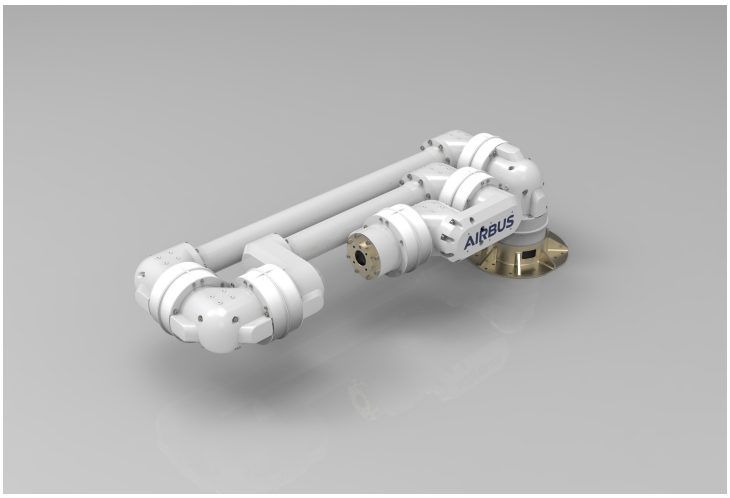

Figure 2.13: The Airbus VISPA (Versatile In-Space and Planetary Arm), a 7-DOF serial manipulator with a publicly available URDF model.

Source: [53].

2.4.3.2 Implications for Reachability Analysis Scope

The inclusion of assembly-class manipulators in the comparative study is motivated by the evolving scope of lunar surface missions. Programmes targeting the Lunar South Pole – such as NASA's Artemis campaign and ESA's European Large Logistics Lander (EL3) – increasingly require robotic systems capable of both scientific exploration and infrastructure support [54]. The ATHLETE platform, for example, was explicitly designed so that its wheel-on-limb configuration could use individual limbs as manipulators for construction and cargo handling tasks [31]. Evaluating manipulator reachability across both exploration and assembly task profiles, rather than exploration alone, therefore provides a more comprehensive assessment of candidate rover-arm configurations for future lunar missions.

The terrain characteristics of the Lunar South Pole region – including steep crater slopes, permanently shadowed regions, and loose regolith with potentially reduced bearing capacity – further constrain the reachable workspace by coupling terrain-induced platform tilt with arm kinematics. These terrain inputs are incorporated into the reachability

analysis framework developed in subsequent chapters.

2.4.4 Summary

Planetary rover manipulators have evolved from the compact 0.8 m, 4 kg IDD on the MER rovers to the 2.2 m and 2.1 m multi-instrument arms on Curiosity and Perseverance respectively, with each generation supporting increasingly complex sampling and analytical tasks. All exploration-class flight systems to date employ five-DOF serial kinematic chains as a compromise between dexterity and system mass. However, the scope of planetary manipulation is expanding beyond exploration to include assembly, construction, and ISRU tasks, motivating the investigation of higher-DOF arms such as the Airbus VISPA. The concept of whole rover–arm coordination offers an additional pathway to augment manipulator capability by leveraging rover mobility as additional task-space DOF, an approach with direct relevance to future low-mass sample return missions. The selection and evaluation of manipulator configurations in this study will therefore consider not only the arm's intrinsic workspace and manipulability, but also the coupled effects of base placement, mounting location, platform stability, terrain slope, and the dual requirements of exploration and assembly operations at the Lunar South Pole.

2.5 Rover–Manipulator System Considerations

2.5.1 Manipulability and Workspace Evaluation

The quality of a manipulator's configuration at a given pose can be assessed through manipulability metrics derived from the Jacobian matrix. Given a manipulator with joint variables $\mathbf{q}$, the set of end-effector velocities achievable for unit-norm joint velocities ($\|\dot{\mathbf{q}}\| \leq 1$) defines an ellipsoid in task space, known as the manipulability ellipsoid [55]. The volume of this ellipsoid,

$$w = \sqrt{\det\left(\mathbf{J}(\mathbf{q})\,\mathbf{J}^T(\mathbf{q})\right)}$$

provides a scalar measure of the arm's ability to arbitrarily change the position and orientation of the end effector at a given configuration. Higher values indicate configurations in which the manipulator can move freely in all directions, while values approaching zero indicate proximity to kinematic singularities where motion capability degenerates along one or more directions [55].

This metric has direct practical relevance for planetary operations. Backes et al. [56] implemented the manipulability ellipsoid volume as the objective function in an automated rover base placement algorithm, in which the rover iteratively repositions itself to maximise the manipulability at a specified science target. The algorithm searches along the approach

vector to find the rover pose that places the target within the arm's reachable workspace while maximising the ability of the manipulator to perform the required task. This whole-rover approach to manipulation planning – in which the three degrees of freedom of rover mobility (position and heading) augment the arm's own DOF – was developed specifically for low-mass rover missions such as Mars Sample Return fetch rovers, where reducing the number of arm joints decreases system mass and complexity [57].

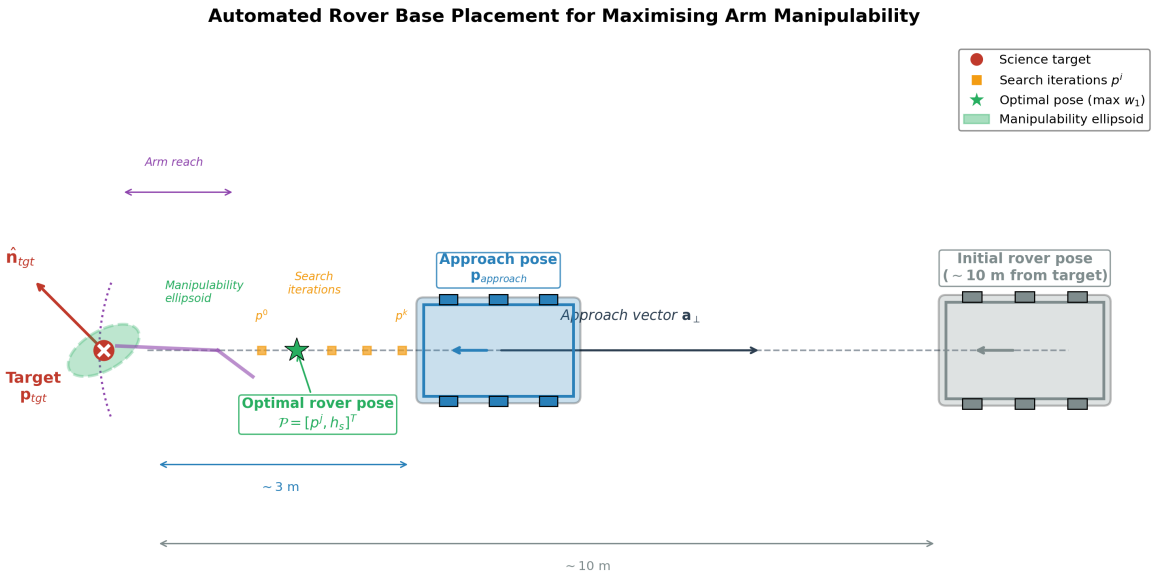

Figure 2.14: Conceptual diagram of automated rover base placement for maximising arm manipulability at a science target.

Adapted from: [56].

2.5.2 Whole Rover–Arm Coordination

The conventional operational paradigm for planetary manipulation treats the rover as a stationary gross-positioning platform: operators command the rover to a suitable pose, and subsequently command the arm to reach the target from this fixed base [56]. This sequential approach requires multiple communication cycles with Earth operators and yields a rover pose that is acceptable rather than optimal. An alternative paradigm, termed whole rover–arm coordination, exploits the rover's three mobility DOF (planar position and heading) as additional degrees of freedom for the manipulation task [57].

This concept is particularly relevant for low-mass rovers intended for Mars Sample Return fetch operations. If the rover's mobility DOF can compensate for a reduced-DOF arm, it becomes possible to design a lighter rover-tool system with fewer arm joints while maintaining sufficient task-space capability for coring and sample retrieval [57]. As illustrated by JPL's research on the Rocky 8 prototype, a two-DOF manipulator utilising the rover base for coarse positioning can accomplish drilling tasks that would otherwise

require a five-DOF arm on a stationary platform [56, 57]. The enabling technologies for this approach include automated base placement, collision-free arm path planning that accounts for both rover and terrain geometry, and vision-guided manipulation using stereo camera feedback to refine end-effector positioning to millimetre-level accuracy [56].

Figure 2.15: Comparison of rover–manipulator coordination strategies: a 2-DOF manipulator utilising base mobility (left) versus a 5-DOF arm operating from a stationary platform (right).

Source: [57].

2.5.3 Arm Mounting Location and Reachability Implications

The mounting location of the manipulator on the rover chassis has a significant influence on both the reachable workspace and the stability of the combined system. As discussed in Section 2.1, the Perseverance arm is mounted at the front and bottom of the rover, a configuration that optimises the useful workspace for ground interaction. Capability and reachability map analyses demonstrate that this frontal mounting maximises the manipulator's orientation freedom for surface tasks while minimising the risk of kinematic singularities [25, 26]. Conversely, mounting the arm on the upper part of the chassis would require a significant portion of the arm's reach to bypass the rover's own structure, creating shadow zones that reduce the effective workspace for ground-level operations [27].

The interaction between arm configuration and rover stability is governed by the shift in the global centre of mass as the manipulator extends. This relationship is quantified through the Zero Moment Point and the geometry-based stability margins presented in Section **??**. For the quasi-static reachability analysis central to this study, the manipulator's reachable workspace must be evaluated jointly with the geometric stability margin to identify the set of arm configurations that are both kinematically feasible and statically stable.

2.6 Lunar Terrain Slope Characteristics

The characterisation of lunar slope distributions is essential for designing representative terrains in rover–manipulator system evaluation. High-resolution orbital measurements from the Lunar Reconnaissance Orbiter (LRO) Laser Altimeter (LOLA) provide comprehensive global topographic data, forming the primary basis for quantitative slope analysis of the lunar surface [58]. These datasets enable the statistical description of terrain morphology across different geological regions and spatial scales.

Analysis of LOLA-derived datasets reveals clear distinctions between lunar maria and highland regions. Highland terrains are generally more rugged, exhibiting median slopes of approximately 9.1°, mean values of 11.0°, and a standard deviation of 7.0° at a 15 m baseline [59]. In contrast, mare regions are significantly smoother, with median slopes around 3.5°, mean values of 4.9°, and a standard deviation of 4.5° under the same baseline conditions [59]. These results highlight the strong dependence of slope characteristics on geological context and confirm that mare regions provide relatively benign mobility conditions compared to highlands.

Global-scale analyses further indicate that the majority of the lunar surface is characterised by relatively low-to-moderate slopes, while steeper terrain is typically confined to localised geological features such as crater walls, rille edges, and mountainous regions [58]. Evidence from Apollo-era mission studies also confirms the presence of operationally challenging terrain, including steep slopes encountered in the Hadley–Apennine region during Apollo 15, where local features such as rille walls can reach slopes on the order of 25° [60]. These observations demonstrate that while extreme slopes are not dominant globally, they remain relevant for assessing rover stability limits.

While these datasets provide a robust statistical foundation, several limitations should be considered when applying them to rover mobility analysis. First, slope values are inherently dependent on the measurement baseline (e.g., 15 m in [59]), whereas rover–terrain interactions occur at smaller spatial scales. As a result, micro-topography and local surface irregularities may not be fully captured by these statistics. Second, global slope distributions aggregate diverse terrain types, meaning that steep slopes ($> 15°$) represent localised rather than typical conditions. Consequently, such slopes should be interpreted as boundary or stress-test scenarios in simulation rather than nominal operating environments.

Based on these considerations, the terrain modelling approach adopted in this study employs discretised slope categories to balance physical realism and computational tractability. Three primary categories are defined: gentle slopes (0–5°), representing mare-like plains; moderate slopes (5–10°), corresponding to mixed or transitional terrain; and steep slopes (10–15°), representing challenging but commonly observed highland conditions. In addition, extended slope ranges up to 20–25° are included selectively to probe stability

limits under extreme conditions.

This discretisation enables systematic comparison across rover configurations while maintaining consistency with observed lunar terrain statistics. Furthermore, the use of co-planar slope approximation provides a computationally efficient representation of terrain inclination in both longitudinal (pitch) and lateral (roll) directions, which is suitable for system-level reachability–stability analysis. It is noted, however, that higher-fidelity terrain models may be required in future work to capture detailed contact interactions and locomotion dynamics [58, 59].

2.7 Stability Metrics for Planetary Mobile Manipulators

2.7.1 Geometry-Based Stability Criteria

Geometry-based stability criteria form the foundational approach for assessing static equilibrium in planetary mobile manipulators. In contrast to fixed-base manipulators, manipulators operating on unanchored platforms exhibit stability characteristics governed by the relationship between the centre of mass and the ground contact configuration [8]. These principles directly apply to planetary rover-manipulator systems [61]. Under quasi-static conditions, static stability is typically defined using the concept of the support polygon.

The support polygon is constructed as the convex hull of all ground contact points between the robot and the terrain. A system is considered statically stable if the vertical projection of its CoM lies within this polygon [13]. Let denote the projected CoM and the support polygon. The static stability condition can be expressed as

$$p_{com} \in \mathcal{P}.$$

This formulation is widely adopted in both wheeled and legged robotics due to its simplicity and physical interpretability [13, 61]. It relies solely on geometric relationships and does not require dynamic modelling, making it suitable for planetary operations that are predominantly slow and quasi-static, such as gradual manipulator extension.

However, the support-polygon condition provides only a binary assessment of stability. For comparative evaluation across different rover configurations, a continuous measure is more informative. To address this limitation, stability margin formulations extend the geometric criterion by quantifying the distance from the CoM projection to the boundary of the support polygon. A common definition is the minimum distance to any polygon

edge:

$$d_{\min} = \min_{e_i \in \partial P} \operatorname{dist}(p_{com}, e_i)$$

This distance-based margin indicates how close the system is to tipping [13]. Larger values correspond to greater resistance to overturning, while represents the tipping boundary. Unlike the binary test, this continuous metric enables quantitative comparison between different base geometries and arm configurations.

For planetary mobile manipulators, geometry-based stability margins are particularly relevant because manipulator motion alters the global CoM location. As the arm extends, the CoM shifts relative to the support polygon, reducing the available stability margin. Consequently, the reachable workspace of the manipulator is implicitly constrained by geometric stability conditions. A target may be kinematically reachable but geometrically infeasible once the associated CoM displacement reduces below an acceptable threshold.

Importantly, geometry-based criteria remain applicable across different mobility mechanisms. For conventional wheeled rovers, the support polygon is determined by wheel–terrain contact geometry. For articulated or wheeled-legged systems, the polygon may become reconfigurable through suspension or limb adjustment [14]. In legged systems, it depends on foothold selection. Despite these structural differences, the underlying geometric stability condition remains consistent.

Although geometry-based approaches provide a unified and computationally efficient baseline for evaluating static stability [61], they inherently neglect the directionality of resultant forces, angular loading effects, and inertial contributions during manipulation. Such limitations become critical for mobile manipulators operating under load transfer or dynamic arm motion. These shortcomings have motivated the development of moment- and wrench-based stability formulations [8].

2.7.2 Moment-Based Stability Criteria

While geometry-based criteria evaluate stability solely through the relative position of the CoM within the support polygon, moment-based approaches consider the distribution of forces and torques acting on the system [62]. These formulations assess stability by analysing the resultant moments about potential tipping edges, thereby incorporating the directionality and magnitude of external forces.

In moment-based stability analysis, tipping is assumed to occur about a specific edge of the support polygon [62]. Let denote a candidate tipping edge. Stability is evaluated by examining the net overturning moment about this edge [15].

$$M_{\text{net}}^{(e_i)} = M_{\text{gravity}}^{(e_i)} + M_{\text{inertia}}^{(e_i)} + M_{\text{external}}^{(e_i)}$$

The system remains stable if the restoring moment generated by gravity exceeds the

destabilising moments induced by inertial forces, manipulator motion, or external loads. This condition can be expressed conceptually as:

$$M_{\text{restoring}} > M_{\text{overturning}}$$

Unlike purely geometric criteria, this formulation explicitly accounts for load transfer and dynamic effects. For mobile manipulators, manipulator acceleration and interaction forces can significantly alter the moment balance, even when the projected CoM remains inside the support polygon [15]. Consequently, moment-based criteria provide a more physically complete representation of stability under manipulation tasks involving external contact or dynamic arm motion [8].

A notable contribution in this domain is the development of tip-over stability margins for mobile manipulators, where the stability measure is defined in terms of the minimum net stabilising moment across all potential tipping edges [15]. Such formulations extend the geometric concept of distance-based margins by incorporating force distribution and system dynamics.

However, moment-based approaches typically require knowledge of ground reaction forces, mass distribution, and dynamic states, increasing computational complexity compared to geometric methods. While they offer improved physical fidelity, their practical implementation in planetary systems must balance modelling accuracy with onboard computational constraints [16].

2.7.3 Contact-Force-Based Stability Criteria

While moment-based approaches evaluate stability through the net torque about potential tipping edges, contact-force-based criteria analyse the full distribution of ground reaction forces and their feasibility under physical constraints. These formulations assess whether a set of contact forces exists that satisfies equilibrium conditions while respecting frictional and unilateral contact constraints.

In contact-force-based stability analysis, the system is considered stable if there exists a set of contact forces at all ground contact points such that:

1. Static or dynamic equilibrium is satisfied,

$$\sum \mathbf{F} = 0, \quad \sum \mathbf{M} = 0$$

2. Each contact force lies within its corresponding friction cone,

$$\sqrt{F_x^2 + F_y^2} \leq \mu F_n$$

3. Normal contact forces remain compressive (i.e., no tensile ground reaction),

$$F_n \geq 0$$

Unlike geometry-based methods, which rely solely on the projected CoM position, and moment-based criteria, which focus on torque balance about a specific edge, contact-force-based formulations consider the entire wrench space generated by contact forces. Stability is therefore interpreted as the feasibility of force equilibrium within admissible contact constraints [17].

This perspective is closely related to concepts such as support wrench cones and force-closure conditions, widely used in legged robotics and multi-contact manipulation. By explicitly incorporating friction limits and load redistribution among contacts, contact-force-based approaches can capture scenarios where geometric stability appears satisfied, yet insufficient friction or uneven force distribution leads to slippage or local loss of support [17, 18].

For planetary mobile manipulators operating on deformable or low-friction terrain, such as regolith surfaces, contact-force feasibility becomes particularly important. Even when the CoM projection lies within the support polygon, reduced friction coefficients or shifting contact conditions may invalidate the existence of a physically admissible force distribution [18]. Consequently, contact-force-based criteria provide a more comprehensive representation of stability under complex terrain interaction.

However, these formulations require estimation or measurement of contact forces and friction parameters, increasing modelling complexity and computational demand [63]. In practice, they are often employed in high-fidelity simulations or advanced control frameworks, while geometry-based methods remain attractive for rapid onboard evaluation.

2.7.4 Comparative Synthesis for Planetary Mobility Evaluation

Table 2.4 summarises the principal characteristics of the three stability assessment paradigms. A hierarchical interpretation emerges: geometry-based methods provide a computationally efficient baseline for quasi-static workspace evaluation, moment-based criteria enhance physical realism under dynamic manipulation, while contact-force-based formulations offer the most comprehensive stability modelling at the expense of computational complexity. In the context of this study, which focuses on quasi-static reachability analysis, geometry-based stability margins are adopted as the primary evaluation metric.

Criterion	**Geometry**	**Moment**	**Contact-Force**
Physical basis	CoM projection relative to support polygon	Net moment about tipping edge	Feasibility of admissible contact wrench
Accounts for external loads	No	Yes	Yes
Accounts for inertia	No	Yes	Yes
Friction modelling	No	Implicit	Explicit (friction cone)
Output type	Binary / distance margin	Continuous moment margin	Feasibility region
Workspace integration	Direct geometric mapping	Coupled with force estimation	Requires full contact model
Computational demand	Very low	Medium	High
Suitable for onboard use	High	Moderate	Limited
Suitable for quasi-static planning	Excellent	Good	Moderate
Suitable for dynamic interaction	Weak	Strong	Very strong
Main limitation	Ignores force directionality	Requires force/mass estimation	High modelling complexity

Table 2.4: Comparison of stability evaluation criteria for planetary mobile manipulators

2.8 Research Gaps and Objectives

2.8.1 Research Gaps

Despite the growing body of research on planetary rover mobility, manipulator design, and stability evaluation, these aspects are often studied separately. Existing studies commonly focus on rover mobility mechanisms and terrain traversal performance [9, 19], or on manipulator kinematics and workspace analysis [25, 27], typically assuming a fixed base. However, rover–manipulator systems operating in planetary environments introduce strong coupling between manipulation and platform stability [15, 62]. When a manipulator extends to reach distant targets, the overall centre of mass of the system shifts relative to the rover's support polygon, potentially reducing stability [15, 62]. While several stability metrics have been proposed for mobile robots, limited research systematically investigates how rover mobility configuration, manipulator placement, and geometric scaling influence

the trade-off between reachable workspace and static stability.

Furthermore, comparative studies across different planetary mobility mechanisms—such as wheeled, wheeled-legged, and legged platforms—remain limited, particularly under representative lunar terrain conditions [9, 64, 65]. Therefore, a systematic framework is needed to evaluate how rover configuration and manipulator integration influence both reachable workspace and static stability. Such an analysis can support the identification of rover–manipulator configurations that achieve an effective balance between manipulation capability and platform stability for planetary exploration tasks.

The central research question addressed in this study is:
Which planetary rover mobility configurations and manipulator placements maximise reachable workspace while maintaining static stability under representative planetary terrain conditions?

2.8.2 Research Objectives

Based on the identified research gap, this study aims to investigate how rover mobility configuration and manipulator placement influence the relationship between reachable workspace and system stability in planetary rover–manipulator systems.

The main objectives of this research are:

1. To analyse planetary rover mobility mechanisms and manipulator configurations, and identify representative rover–manipulator system architectures for further evaluation.

2. To develop a systematic modelling and evaluation framework for analysing manipulator reachability and rover static stability in rover–manipulator systems.

3. To investigate the trade-off between reachable workspace and system stability across different rover configurations through comparative simulation studies in representative planetary terrain conditions.

This study makes three main contributions:

1. A systematic modelling and evaluation framework for analysing reachability–stability trade-offs in rover–manipulator systems.

2. A structured configuration-space generation and analysis approach enabling large-scale comparative evaluation of rover–manipulator systems across different mobility architectures.

3. Comparative insights into how rover mobility architecture influences the reachability–stability balance, demonstrated through simulation-based evaluation in representative planetary terrain conditions.

Chapter 3

Methodology

3.1 Problem Definition

This study investigates the reachability–stability trade-off in rover–manipulator systems through a configuration-based comparative analysis framework. In contrast to conventional studies that analyse either manipulator workspace or rover stability independently, this work formulates the problem as a coupled system-level evaluation across different rover mobility architectures and manipulator configurations.

System Description

The system consists of a rover platform and a serial-link manipulator mounted on the rover body. For analysis, both the rover and the manipulator are represented using simplified geometric models defined by a set of key parameters, enabling a consistent abstraction of the physical system. These parameters govern the reachability and stability characteristics of the system and are categorised into static parameters and active adaptation parameters. Within this framework, the rover mobility architecture is treated as the primary object of investigation, while a set of disturbance conditions is introduced to systematically vary the system configuration. These disturbance conditions include manipulator-related variations and environmental factors, enabling comparative analysis of how different rover architectures respond to changes in system configuration and terrain conditions.

Experimental Design

To enable fair comparison across different rover architectures, a parametric scaling strategy is adopted, where rover platforms are normalised to equivalent mass levels. Based on this, a set of configuration variations—including manipulator mass and size scaling, mounting position, representative postures, and terrain conditions—is systematically generated for analysis. These variations influence system reachability and stability by altering the position of the system centre of mass and its relative location with respect to

the support polygon. This enables comparative analysis of how different rover architectures respond under varying conditions.

Modelling Strategy

From a system perspective, the reachability–stability relationship in rover–manipulator systems is governed by the continuous motion of the manipulator, which causes a continuous shift in the overall system centre of mass (CoM) relative to the support polygon. As the manipulator extends, this coupled variation directly affects both reachable workspace and static stability. When combined with multiple disturbance factors—such as manipulator scaling, mounting position, rover architecture, and terrain conditions—the resulting configuration space becomes high-dimensional. Analysing this relationship under continuous manipulator motion across all disturbance combinations would require exhaustive sampling, leading to prohibitive computational complexity and making the problem intractable.

To address this challenge, a discretised configuration-space strategy is adopted. The continuous motion of the manipulator is approximated using a set of representative deployment postures, reducing the dimensionality of the problem while preserving key behavioural characteristics. In addition, reachability is quantified using a distance-based system reach metric, rather than full workspace reconstruction. Furthermore, the rover's active adaptation is formulated as a reduced-dimensional adjustment problem, enabling efficient evaluation under stability constraints. This approach retains the influence of multiple disturbance factors while ensuring computational tractability for comparative analysis.

Modelling Assumptions

To simplify the analysis while retaining the dominant physical effects, the following assumptions are adopted:

1. The rover chassis is modelled as a rigid body with lumped mass distribution.
2. The manipulator is modelled as a rigid serial-link mechanism with fixed link masses.
3. Manipulator motion is quasi-static; inertial effects are neglected.
4. Terrain is represented by slope components in x and y directions.
5. Wheel–terrain interaction follows a no-slip assumption, and all wheels remain in contact with the ground.
6. Suspension articulation, wheel slip, and dynamic effects are not modelled.
7. External disturbances are neglected; only gravitational effects are considered.

Problem Statement

Under this modelling framework, the objective of this study is to investigate how rover mobility architecture and manipulator placement influence the reachable workspace of rover–manipulator systems while maintaining static stability under representative planetary terrain conditions.

3.2 Research Framework

This study adopts a structured methodological framework to analyse the relationship between manipulator reachability and rover stability across different rover–manipulator configurations. The overall framework is illustrated in Fig. 3.1, which organises the research process into six main stages: system configuration definition, parameter specification, parametric scaling, analytical modelling, simulation validation, and comparative evaluation.

First, the system configuration layer defines the architectural design space of rover–manipulator systems. This includes different rover mobility mechanisms (e.g., wheeled, wheeled–legged, and legged platforms), rover structural configurations such as support points and suspension types, and manipulator configurations including reach capability, degrees of freedom, payload capacity, and installation position on the rover body.

Based on these configurations, a set of system parameters is established to describe the physical properties of the rover–manipulator system. These parameters include rover mass, rover size, base footprint, suspension characteristics, arm mass, arm size, payload capacity, workspace range, and terrain slope conditions.

To enable fair comparison between different system architectures, a parametric scaling layer is introduced. Starting from a reference rover–manipulator model, geometric dimensions and associated physical parameters can be scaled up or down according to predefined scaling rules and physical constraints. In addition, parametric fusion allows rover platforms and manipulators of different sizes to be combined, enabling the exploration of a wider range of rover–manipulator configurations.

The generated configurations are then analysed through analytical modelling, which includes both geometry-based stability analysis and moment-based stability evaluation. Finally, the models are evaluated through a combination of numerical calculations, geometric simulations, and environmental simulations, followed by qualitative and quantitative comparative assessment of reachable workspace and stability performance.

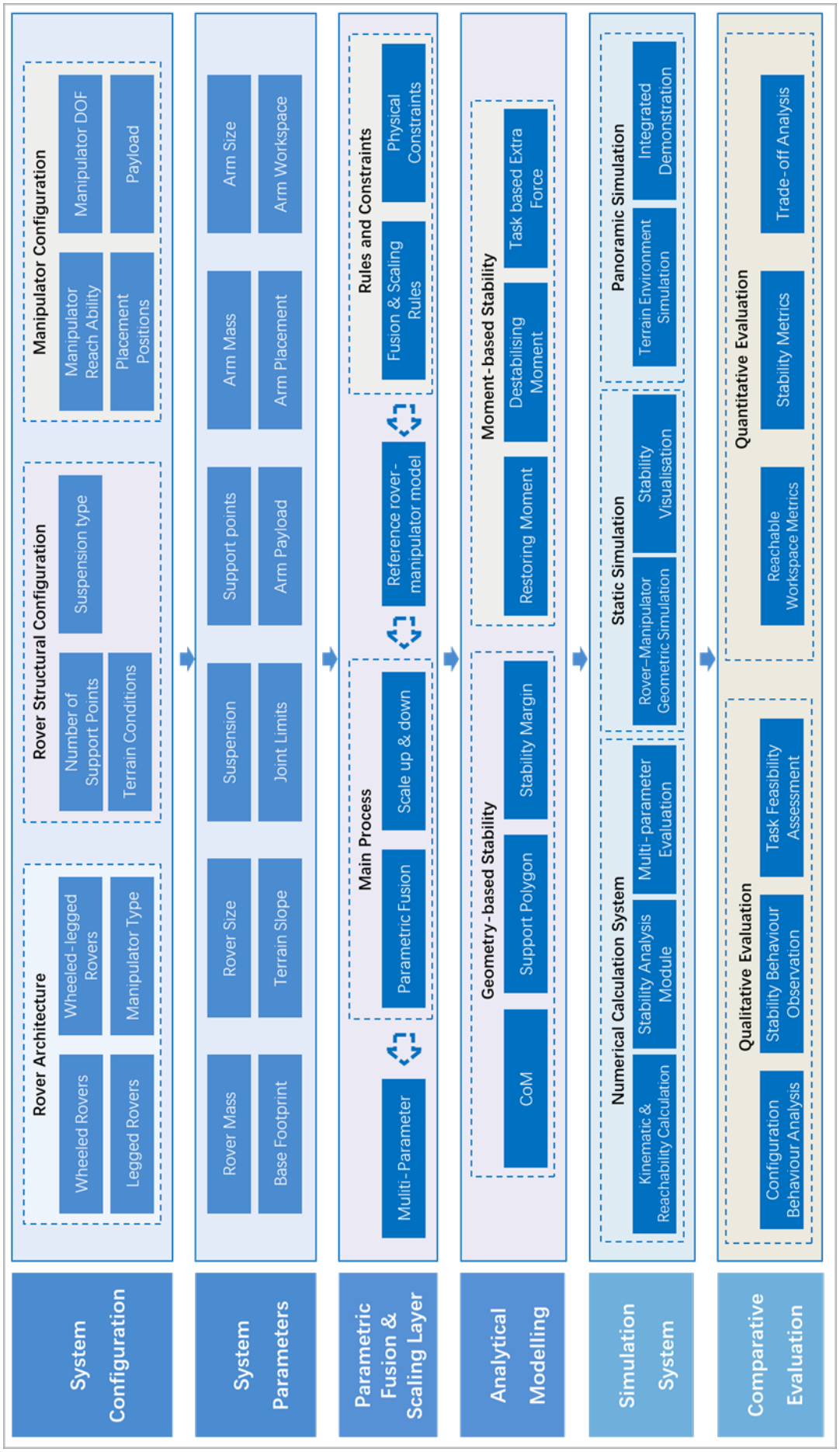

Figure 3.1: Integrated framework for configuration modelling and stability evaluation of rover–manipulator systems

3.3 System Configuration

The system configuration stage defines the design space of rover–manipulator systems considered in this study. The objective of this stage is not to analyse a single robotic platform, but to establish a set of representative rover and manipulator configurations that can be used to generate multiple rover–manipulator system variants for subsequent modelling and evaluation.

In this stage, several categories of rover mobility platforms and robotic manipulators are selected to form a configuration library. The rover platforms represent different mobility mechanisms commonly considered for planetary exploration, including wheeled, wheeled–legged, and legged architectures. For the manipulation subsystem, different robotic arm configurations are considered with variations in reach capability, payload capacity, and installation position on the rover body.

These rover and manipulator configurations serve as the fundamental building blocks of the framework. In the subsequent parametric fusion and scaling layer, rover platforms and manipulator systems can be systematically combined and scaled according to predefined rules and constraints. This process enables the generation of multiple rover–manipulator configurations while maintaining consistent structural relationships, allowing fair comparison of reachability and stability performance across different system designs.

3.3.1 Geometric Parameter Definition and Scaling

The selection of configuration parameters in this study follows three main principles:

1. Parameters must adequately represent the geometric and structural characteristics of the rover–manipulator system.

2. Parameters are selected based on their direct relevance to system reachability and static stability.

3. A limited number of descriptive parameters is included for identification and classification purposes, such as platform name and mobility type.

Based on these principles, the rover configuration is defined using a structured set of parameters, including geometric, mass, support, posture, and mounting interface variables. These parameters collectively describe the physical structure of the rover, its support geometry, and its admissible posture configurations. The complete parameter definition is summarised in Table 3.1.

The classification of parameters as scalable or non-scalable follows a set of modelling principles. Parameters associated with geometric dimensions and mass properties are

treated as scalable, as they define the physical size and proportional characteristics of the rover and can be adjusted using a geometric scale factor. In contrast, parameters that define the structural architecture, configuration topology, or admissible posture ranges are not scaled, as they represent intrinsic characteristics of the platform. Following the same parameter selection principles, the manipulator configuration is defined in a consistent manner. The selected parameters are summarised in Table 3.2 and 3.3.

3.3.2 Reference Frame Definition

To ensure consistency and computational efficiency in the modelling and evaluation process, a unified rover reference frame is adopted for all geometric, kinematic, and stability calculations in this study.

The origin of the rover reference frame is defined at the projection of the rover body reference point onto the ground plane, typically taken as the geometric centre of the chassis. The xand yaxes lie on this reference plane, while the z-axis is defined normal to the plane. All geometric quantities, including support point coordinates, manipulator mounting interfaces, and centre of mass positions, are expressed in this frame.

The manipulator is initially defined in its local base frame using the Modified Denavit–Hartenberg (MDH) convention. Once mounted on the rover, the manipulator base frame is transformed into the rover reference frame through the predefined mounting interface. All subsequent kinematic calculations and mass property representations of the manipulator are therefore expressed in the rover frame, enabling unified evaluation of the combined rover–manipulator system.

Terrain effects are incorporated without introducing additional coordinate systems. Instead of explicitly reconstructing a terrain-aligned frame or rotating the support polygon, terrain inclination is represented through the direction of gravity used in the projection of the system centre of mass. This approach allows the influence of slope to be captured by modifying the projected position of the centre of mass within the rover reference frame, while maintaining a fixed support polygon representation.

This formulation enables all reachability and stability computations to be performed within a single reference frame, avoiding unnecessary coordinate transformations while preserving the key geometric relationships governing system behaviour.

3.3.3 Wheeled Rover Platform Selection

3.3.4 Overview

The methodology follows a multi-stage approach, integrating high-fidelity CAD modeling, terramechanics, and stochastic simulations to determine the optimal configuration for

a robotic arm mounted on a lunar rover. The objective is to maximize the arm's reach while ensuring system stability in a low-gravity environment ($g_{moon} = 1.62\,\mathrm{m/s^2}$).

3.3.5 Phase I: High-Fidelity CAD and Inertial Modeling

To ensure the simulation reflects physical reality, a bottom-up modeling approach is adopted using **SolidWorks**.

- **Mass Distribution:** Internal components (batteries, actuators, and avionics) are modeled as concentrated masses at their estimated 3D coordinates.
- **Inertial Tensors:** The global Center of Mass (CoM) and the inertia tensor matrix $[I]$ are extracted for both stowed and deployed configurations using the parallel axis theorem:

$$[I]_{rover} = \sum_{i=1}^{n} (I_i + m_i[(\mathbf{r}_i \cdot \mathbf{r}_i)\mathbf{E} - \mathbf{r}_i \otimes \mathbf{r}_i]) \tag{3.1}$$

  where $\mathbf{r}_i$ is the displacement vector from the global CoM to the i^{th} component.

3.3.5.1 Parametric Scaling and Comparative Analysis

To evaluate the impact of rover scale on operational efficiency, the methodology incorporates a comparative study of different rover classes. This is achieved through the **SolidWorks Scaling Tool**, allowing for the rapid generation of variants while maintaining geometric proportionality.

- **Dimensional Scaling:** Three distinct rover configurations are generated (Small, Medium, and Large) by applying a linear scale factor S to the original assembly.
- **Mass-Volume Relation:** The mass of each variant is adjusted based on the volumetric scale S^3, ensuring that material density and internal component density remain consistent across the study:

$$m_{new} = m_{base} \cdot S^3 \tag{3.2}$$

- **Comparative Metrics:** The different configurations are compared based on their *Power-to-Weight Ratio* and their *Stability-to-Reach Index*. This approach allows for the identification of a "Sweet Spot" where the rover's mass provides enough anchorage for the arm's torque without compromising mobility in soft regolith.

3.3.6 Phase II: Environmental and Terramechanics Constraints

The lunar regolith interaction is modeled using the **Mohr-Coulomb** failure criterion and the **Bekker-Wong** equations to account for sinkage and motion resistance.

3.3.6.1 Soil Interaction Parameters

The following parameters, derived from Apollo mission data, are utilized for the simulation:

3.3.6.2 Drawbar Pull and Tractive Effort

The net tractive force, or Drawbar Pull (DP), is defined as:

$$DP(\theta, s) = H(s) - R_c - m \cdot g_{moon} \cdot \sin(\theta) \tag{3.3}$$

Where $H(s)$ is the gross thrust based on wheel slip (s), R_c is the motion resistance due to soil compaction, and θ is the terrain slope.

3.3.7 Phase III: Mathematical Framework for Stability

System stability is evaluated using the **Stability Polygon Method**.

1. **Support Polygon:** Defined by the convex hull of the wheel contact points $\{P_1, P_2, P_3, P_4\}$.
2. **Static Stability Margin (SSM):** The minimum distance from the vertical projection of the global CoM to the boundaries of the support polygon.
3. **Tipping Condition:** The system is considered unstable if $SSM \leq 0$ or if the normal force N_i at any wheel contact point reaches zero, indicating wheel lift.
4. **Dynamic CoM Shift:** As the robotic arm extends, the new system CoM (CoM_{sys}) is calculated:
$$\mathbf{R}_{sys} = \frac{m_{rover}\mathbf{r}_{rover} + m_{arm}\mathbf{r}_{arm} + m_{load}\mathbf{r}_{load}}{M_{total}} \tag{3.4}$$

3.3.8 Phase IV: MATLAB/Simulink Co-Simulation

The model is exported via *Simscape Multibody* to simulate the arm's reach.

- **Kinematic Workspace Mapping:** A recursive script iterates through joint angles $\{\alpha, \beta, \gamma\}$ to define the 3D reachable volume.
- **Base Position Optimization:** Mounting coordinates (x_b, y_b) are varied to identify the location that maximizes the *Stable Reachable Workspace* for a 2.0 kg payload.

3.3.9 Phase V: Sensitivity Analysis (Monte Carlo)

To account for lunar uncertainties, a Monte Carlo simulation ($N = 1000$) is executed with stochastic variables:

- **Terrain Slope:** $\theta \sim \mathcal{N}(10°, 5°)$.
- **Regolith Cohesion:** $c \in [0.17, 3.0]$ kPa.
- **Output:** Probability of tip-over vs. arm extension length.

3.3.10 Phase VI: Obstacle and Ditch Transposition

The rover's mobility is evaluated by its ability to negotiate vertical obstacles and cross open ditches common in cratered terrains.

3.3.10.1 Vertical Obstacle Climbing

For a rover to climb a vertical obstacle of height H_{obs}, the wheel radius R_w and the friction coefficient μ must satisfy the geometric constraint:

$$\theta_{climb} = \arccos\left(1 - \frac{H_{obs}}{R_w}\right) \tag{3.5}$$

The static torque required (T_{req}) is calculated as:

$$T_{req} = m g_{moon} R_w \sin(\theta_{climb}) \tag{3.6}$$

A safety factor ($SF = 1.5$) is applied to motor sizing to account for dynamic loads and regolith shear failure.

3.3.10.2 Ditch Crossing Capability

The maximum width of a ditch (W_{ditch}) that the rover can cross depends on the wheelbase (L) and ground clearance (C_g).

- **Geometric Limit:** $W_{ditch} < 2 \cdot R_w$ to avoid wheel entrapment.
- **Clearance Limit:** The crossing is successful only if the chassis does not violate the C_g threshold during the unsupported phase of the CoM trajectory.

3.3.10.3 Simulated Performance Metrics

The "Mobility Map" of the rover is generated by iterating through:

- **Approach/Departure Angles (α_a, α_d):** Maximum slopes before chassis-terrain interference.
- **Break-over Angle (α_b):** Maximum peak angle to avoid "high-centering" based on the rover's longitudinal geometry.

The key parameters need to be defined, refer to Table 3.1.

Table 3.5: Rover platform parameter definition

Category	**Parameter**	**Description**
Geometry	Rover length	Length of the rover chassis
Geometry	Rover width	Width of the rover chassis
Geometry	Rover height	Height of the rover body
Mass	Rover mass	Total mass of the rover platform
Mass	Centre of mass position	Position of the rover centre of mass
Support	Number of support points	Number of ground contact points (wheels or legs)
Support	Support point coordinates	Ground contact positions defining the support polygon, coordinates with respect to centre of mass
Configuration	Mobility type	Wheeled, wheeled–legged, or legged rover architecture
Configuration	Suspension type	Passive or active suspension mechanism, or both
Posture capability	Chassis roll angle	Rotation of the rover body about the longitudinal axis (x-axis), representing the left–right tilting of the chassis relative to the ground
Posture capability	Chassis pitch angle	Rotation of the rover body about the lateral axis (y-axis), representing the forward–backward tilting of the chassis relative to the ground
Posture capability	Chassis height	Vertical position (z direction) of rover chassis
Posture capability	Chassis longitudinal shift	Forward/backward body translation relative to support polygon (x direction)
Posture capability	Chassis lateral shift	Left/right body translation relative to support polygon (y direction)
Manipulator placement	Front-mounted manipulator	Available manipulator mounting interface position (x,y,z) with respect to rover base
Manipulator placement	Centre-mounted manipulator	Available manipulator mounting interface position (x,y,z) with respect to rover base
Manipulator placement	Side-mounted manipulator	Available manipulator mounting interface position (x,y,z) with respect to rover base

3.3.11 Wheeled-legged Rover Platform Selection

The key parameters need to be defined, refer to Table 3.1.

3.3.12 legged Rover Platform Selection

Legged robotic platforms have emerged as the most promising candidates for next-generation planetary surface exploration, owing to their superior traversability over steep, granular, and geometrically irregular terrain that remains inaccessible to conventional wheeled rovers [37]. Among the quadruped-arm systems surveyed, Boston Dynamics Spot — as deployed in the ReLIC framework [39] — represents the most hardware-mature and extensively validated platform, having accumulated over 250,000 km of real-world traversal across environments including nuclear decommissioning sites, underground mine networks, and volcanic planetary analogue terrain [44]. Compared with the Unitree B2 with Z1 arm [41], the HyQReal with Kinova Gen3 [42], and CENTAURO with bilateral 7-DOF arms [43], Spot delivers the longest single-arm reach (984 mm), the highest payload-to-weight ratio (11 kg payload, 32.5 kg total), and the only reinforcement-learning controller that dynamically reassigns legs as auxiliary end-effectors to extend effective workspace beyond the arm kinematic envelope [39]. These characteristics, combined with an autonomous onboard RL policy that eliminates real-time operator input, make Spot-ReLIC the most operationally suitable platform for planetary missions subject to communication latency constraints [38, 39].

3.3.13 Rover Geometric Model and Coordinate Definition

The Spot-ReLIC system is formalised as a rigid multi-body kinematic chain with a floating base, consistent with the whole-body modelling conventions adopted across all five reviewed frameworks [40, 41, 43]. Four right-handed coordinate frames are defined, each derived directly from the official Boston Dynamics SDK geometry documentation and the `spot_ros` URDF [66, 67].

3.3.13.0.1 World Frame $\{\mathcal{W}\}$. The world frame is the inertial reference, with its origin fixed at the robot's boot location and its z-axis aligned with the gravity vector (pointing upward). This corresponds to the `odom` frame in the Spot SDK, estimated via leg-contact kinematics, or the `vision` frame, estimated via visual odometry [66]. Gravity is modelled as $\mathbf{g} = [0,\ 0,\ -9.81]^\top$ ms^{-2} for terrestrial validation, substitutable by $\mathbf{g} = [0,\ 0,\ -3.72]^\top$ ms^{-2} for Martian surface simulation [38].

3.3.13.0.2 Body Frame $\{\mathcal{B}\}$. The body frame origin is placed at the geometric centre of the four hip joints, with the x-axis pointing forward (toward the front hips), the

y-axis pointing laterally left, and the z-axis pointing dorsally upward, as specified by the Spot SDK [66]. This is corroborated in the URDF by the `base_link` joint:

$$\texttt{<origin rpy="0 0 0" xyz="0 0 0"/>} \quad (\texttt{body} \rightarrow \texttt{base\_link}) \tag{3.7}$$

confirming zero offset between the URDF root link and $\{\mathcal{B}\}$ [67]. Each of the four hip abduction joints (`HX`) is offset from $\{\mathcal{B}\}$ by fixed translations extracted from the URDF [67]:

$$\mathbf{p}_{\mathrm{FL}} = [+0.29785,\ +0.05500,\ 0]^{\top}\ \mathrm{m}, \quad \mathbf{p}_{\mathrm{FR}} = [+0.29785,\ -0.05500,\ 0]^{\top}\ \mathrm{m} \tag{3.8}$$

$$\mathbf{p}_{\mathrm{RL}} = [-0.29785,\ +0.05500,\ 0]^{\top}\ \mathrm{m}, \quad \mathbf{p}_{\mathrm{RR}} = [-0.29785,\ -0.05500,\ 0]^{\top}\ \mathrm{m} \tag{3.9}$$

establishing the body half-length of 297.85 mm and the hip lateral outset of 55 mm from the torso centreline [67]. Within each leg chain, the hip-to-thigh (`HY`) joint is offset 110.945 mm laterally (`xyz="0 0.110945 0"`), and the knee (`KN`) joint is positioned 320.5 mm below and 25 mm forward of the thigh pivot (`xyz="0.025 0 -0.3205"`), reflecting the ball-screw push-rod geometry of the knee actuator [67, 68]. Each leg therefore contributes three revolute DOF: hip abduction–adduction (`HX`), hip flexion–extension (`HY`), and knee flexion–extension (`KN`), with joint limits of $[-0.785,\ +0.785]$ rad, $[-0.899,\ +2.295]$ rad, and $[-2.793,\ -0.255]$ rad respectively, as specified in the URDF `<limit>` fields [67].

3.3.13.0.3 Arm Base Frame $\{\mathcal{A}\}$. The arm shoulder mount is rigidly fixed to the anterior-dorsal face of the torso via the front payload rail joint, whose origin is defined in the URDF as [67]:

$$^{\mathcal{B}}T_{\mathcal{A}} = \begin{bmatrix} \mathbf{I}_{3\times 3} & [+0.2075,\ 0,\ +0.0805]^{\top} \\ \mathbf{0}^{\top} & 1 \end{bmatrix} \tag{3.10}$$

placing the first arm joint (`arm0.link_sh0`, shoulder rotation SH0) at +207.5 mm forward and +80.5 mm above the body centre [67]. The six arm joints (SH0, SH1, EL0, EL1, WR0, WR1) are modelled using standard Denavit–Hartenberg parameters extracted from the URDF, with SH1 and EL0 actuated through a mechanically coupled differential transmission governed by [68]:

$$\begin{bmatrix} \dot{q}_{\mathrm{SH1}} \\ \dot{q}_{\mathrm{EL0}} \end{bmatrix} = \frac{1}{101} \begin{bmatrix} 1 & 0 \\ -1 & 1 \end{bmatrix} \begin{bmatrix} \dot{q}_{m_0} \\ \dot{q}_{m_1} \end{bmatrix} \tag{3.11}$$

meaning their individual velocities cannot be set independently; all remaining joints (SH0, EL1, WR0, WR1) operate at a gear ratio of 101:1, and the gripper (`F1X`) at 56.55:1 [68].

3.3.13.0.4 End-Effector Frame $\{\mathcal{E}\}$. The end-effector frame corresponds to the `hand` frame published by Boston Dynamics, placed at the midpoint of the parallel-jaw

gripper with its z-axis aligned with the gripper approach direction [67,69]. The full system therefore comprises 24 actuated DOF: 12 leg joints (3 per leg $\times$ 4 legs) + 6 arm joints + 6 floating-base DOF, and the body-level Jacobian $\mathbf{J} \in \mathbb{R}^{6\times 24}$ maps the full joint velocity vector $\dot{\mathbf{q}} \in \mathbb{R}^{24}$ to the end-effector velocity twist in $\{\mathcal{W}\}$, as employed in the whole-body MPC formulations of [41, 43] and in the ReLIC RL policy of [39].

3.3.14 Manipulator Platform Selection

Three manipulator configurations are selected to span the exploration-to-assembly design space and to pair with the three rover platforms defined in Sections 3.3.1–3.3.3. Selection criteria are: (i) representativeness of the manipulator class, (ii) mass compatibility with the paired rover, and (iii) availability of geometric and kinematic data for modelling.

The **5-DOF Curiosity-heritage arm** (2.2 m reach, 67 kg, 34 kg payload) represents flight-proven exploration-class manipulators and is paired with the wheeled platform [49]. The **6-DOF Spot Arm** (984 mm reach, 8 kg, 11 kg payload) is a compact manipulator designed for legged platforms, where base mobility compensates for reduced reach [39, 45]. The **7-DOF Airbus VISPA** provides kinematic redundancy for assembly and construction tasks and is paired with the wheeled–legged platform; its open-source URDF enables direct ROS 2 integration [53].

All three arms employ open serial kinematic chains with revolute joints. Their parameters are summarised in Table 3.6, and the corresponding modified DH parameters are given in Tables 3.7–3.9. Figure 3.2 illustrates the kinematic topology of each configuration.

Table 3.6: Manipulator platform parameters for the three selected configurations (cf. Table 3.2 template)

Category	**Parameter**	**Curiosity Arm**	**Spot Arm**	**VISPA**
Configuration	Degrees of freedom	5	6	7
Configuration	Joints / Links	5 / 5	6 / 6	7 / 7
Geometry	Joint types	All revolute	All revolute	All revolute
Kinematics	Max. reach (m)	2.2	0.984	TBC*
Mass	Total arm mass (kg)	67	≈ 8	TBC*
Mass	Payload capacity (kg)	34	11	TBC*
Workspace	Dominant volume	Frontal hemisphere	Forward-biased hemisphere	Near-spherical
Pairing	Rover platform	Wheeled (RB)	Legged (Spot)	Wheeled–legged

* To be confirmed from VISPA URDF extraction upon model integration.

Table 3.7: Modified DH parameters — Curiosity-heritage 5-DOF arm

i	a_{i-1} (mm)	α_{i-1} (deg)	d_i (mm)	θ_i
1	0	0	0	θ_1
2	0	−90	0	θ_2
3	1095	0	0	θ_3
4	0	−90	1057	θ_4
5	0	90	0	θ_5

Derived from [49]; links 3 and 4 correspond to upper arm and forearm.

Table 3.8: Modified DH parameters — Spot 6-DOF arm

i	a_{i-1} (mm)	α_{i-1} (deg)	d_i (mm)	θ_i
1 (SH0)	0	0	0	θ_1
2 (SH1)	0	−90	0	θ_2
3 (EL0)	335	0	0	θ_3
4 (EL1)	0	−90	405	θ_4
5 (WR0)	0	90	0	θ_5
6 (WR1)	0	−90	244	θ_6

Extracted from the `spot_ros` URDF [67].

Table 3.9: Modified DH parameters — VISPA 7-DOF arm

i	a_{i-1} (mm)	α_{i-1} (deg)	d_i (mm)	θ_i
1	0	0	0	θ_1
2	0	−90	0	θ_2
3	0	90	d_3^*	θ_3
4	0	−90	0	θ_4
5	0	90	d_5^*	θ_5
6	0	−90	0	θ_6
7	0	90	d_7^*	θ_7

* Link offsets to be extracted from the VISPA URDF [53].

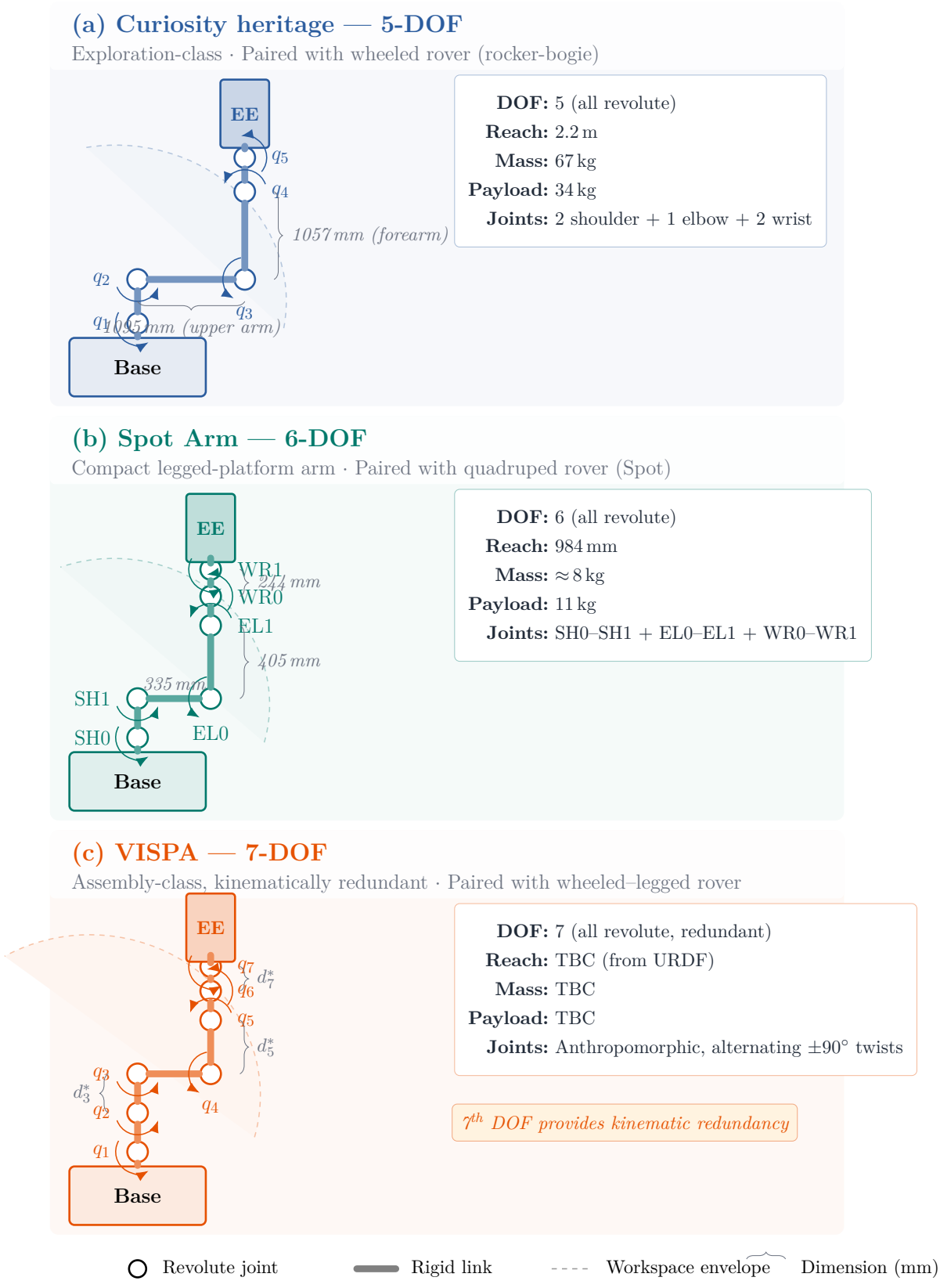

Figure 3.2: Kinematic chain topology of the three selected manipulators. Open circles denote revolute joints; thick lines represent rigid links. Dimension braces indicate principal link lengths in millimetres. Dashed arcs illustrate the approximate workspace envelope. EE = end-effector.

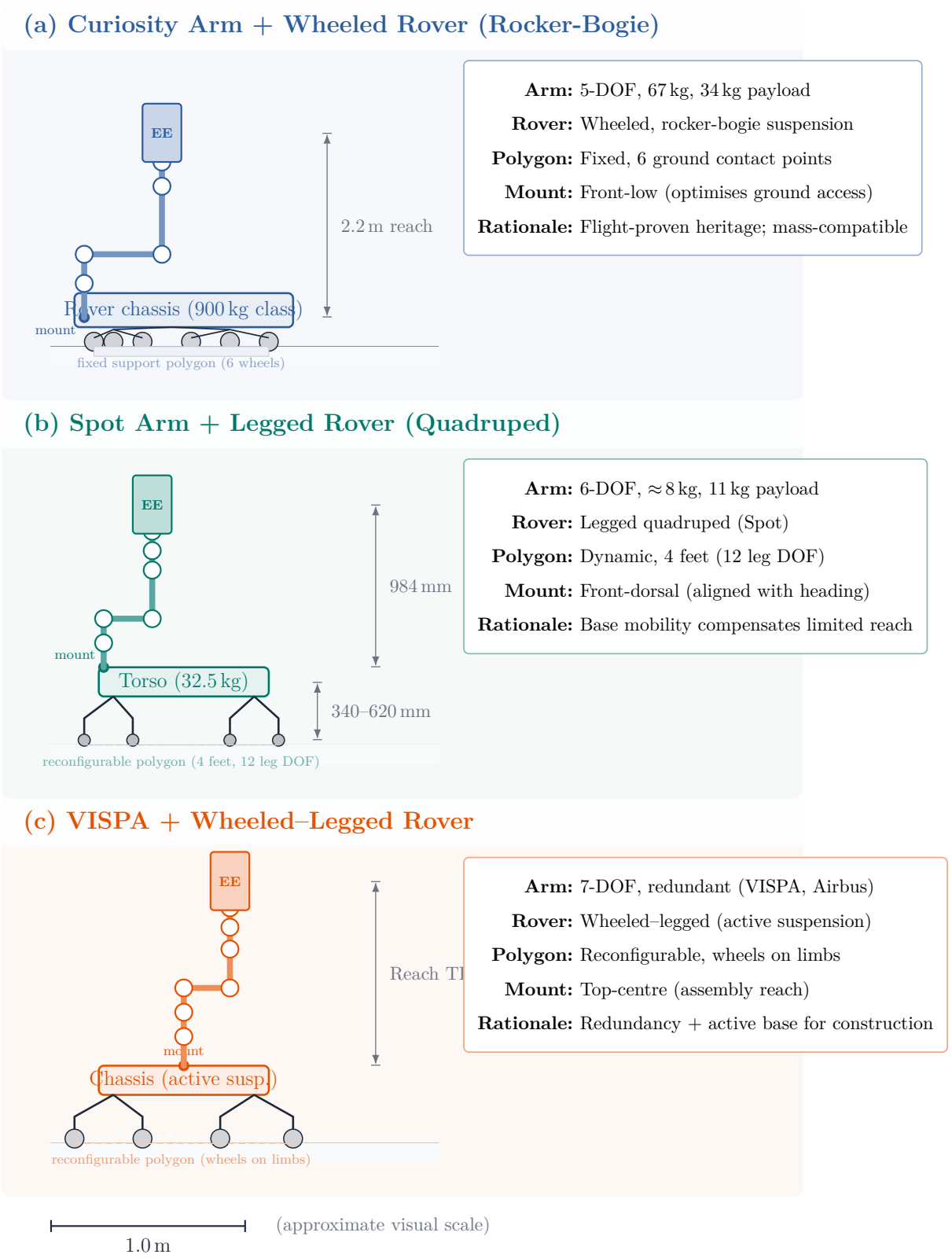

Figure 3.3: Schematic representation of the three rover–manipulator pairings. (a) Curiosity-heritage 5-DOF arm on a wheeled rocker-bogie rover with a fixed support polygon. (b) Spot 6-DOF arm on a legged quadruped with a reconfigurable support polygon. (c) VISPA 7-DOF arm on a wheeled–legged platform with active suspension. Scale bar represents 1.0 m (approximate).

3.3.15 Terrain Design

To investigate the influence of terrain conditions on rover–manipulator configurations, two categories of terrain environments are considered in this study: simplified terrain scenarios and representative lunar terrain environments. The simplified terrains are used to conduct the main numerical analysis under controlled conditions, while the representative lunar terrains are used to simulate rover behaviour in more realistic surface environments.

Simplified Terrain Scenarios

For the numerical analysis, simplified terrain models are adopted in order to isolate the effect of terrain inclination on rover posture and system stability. Instead of modelling detailed lunar surface topography, terrain conditions are represented using geometric slopes defined by the roll and pitch angles of the rover body. Three terrain types are considered: flat terrain, longitudinal slopes, and lateral slopes. Flat terrain represents a horizontal ground surface where both roll and pitch angles of the rover body are zero (roll = 0°, pitch = 0°). This configuration serves as the baseline condition for evaluating rover–manipulator behaviour in the absence of terrain-induced disturbances. For longitudinal slopes, the terrain is inclined in the forward–backward direction relative to the rover heading, producing a pitch angle while the roll angle remains approximately zero. For lateral slopes, the terrain is inclined sideways relative to the rover heading, resulting in a roll angle while the pitch angle remains close to zero. In addition to these single-direction slopes, combined slope conditions are also included to represent terrain surfaces where both roll and pitch inclinations occur simultaneously. To capture different levels of terrain inclination, three slope magnitudes are defined: mild (5°), moderate (10°), and steep (15°). These values are consistent with typical slope ranges considered in planetary rover mobility studies. The complete set of terrain scenarios used in the analysis is summarised in Table 3.10.

Representative Lunar Terrain Environments

To examine rover–manipulator behaviour under more realistic lunar surface conditions, several representative lunar terrain environments are also considered. These terrains are constructed using digital elevation models (DEMs) derived from high-resolution lunar topography datasets. The selected terrains correspond to characteristic geological structures commonly observed on the lunar surface. In particular, terrains associated with crater rims, crater interior slopes, and rough polar topography are included, as these environments represent typical operating conditions for planetary rovers. The representative terrain environments used in this study are summarised in Table 3.11, where the terrain type, geographic location, and corresponding DEM dataset are listed.

3.4 Parametric Fusion and Scale Method

To systematically investigate the influence of rover architecture, manipulator size, and terrain conditions on reachable workspace and system stability, a parametric fusion and scaling framework is introduced. The framework generates a structured configuration space of rover–manipulator systems by combining rover scaling, ratio-based manipulator scaling, and representative arm deployment postures. This approach enables a consistent comparison of different rover–manipulator configurations while controlling the number of evaluated cases. The overall procedure consists of three main steps:

1. Parametric scaling of rover platforms
2. Ratio-based scaling of the manipulator relative to the rover
3. Fusion of rover and manipulator configurations across different terrain conditions

In addition, a set of representative manipulator deployment postures is defined to evaluate the effect of arm extension on system stability.

3.4.1 Rover Parametric Scaling

A reference rover configuration is first defined to represent the geometric and mass properties of the rover platform. To explore different rover sizes while preserving geometric similarity, a parametric scaling approach is applied. The linear scaling factor is defined as:

$$s = \left(\frac{m_{target}}{m_{ref}} \right)^{1/3} \tag{3.12}$$

where:

- m_{ref} is the reference rover mass
- m_{target} is the target rover mass
- s is the linear scaling factor

All major geometric dimensions of the rover (length, width, and height) are scaled proportionally using this factor, ensuring that the overall structural proportions of the rover remain consistent across different mass levels. To represent a wide range of rover sizes used in planetary exploration missions, six rover mass levels are considered in this study, as shown in Table 3.X.

These scaling levels allow the study to cover rover platforms ranging from small reconnaissance robots to large heavy-duty exploration systems.

3.4.2 Manipulator Ration-Based Scaling

Instead of defining independent manipulator mass levels, the manipulator size is scaled relative to the rover platform using the arm-to-rover mass ratio. The ratio is defined as:

$$\lambda = \frac{m_{arm}}{m_{rover}} \tag{3.13}$$

where m_{arm} represents the manipulator mass, m_{rover} represents the rover mass, and λ denotes the arm-to-rover mass ratio.

Using a ratio-based scaling approach allows the manipulator size to adapt automatically to the rover platform and enables the study of how the relative size of the manipulator affects system stability and reachable workspace. To avoid excessive computational redundancy while still covering a wide design space, eight representative ratio levels are selected, as shown in Table 3.X.

The selected ratios cover three conceptual design regions:

- **Low ratio region (0.03–0.08):** manipulators with minimal influence on rover stability.
- **Balanced region (0.12–0.25):** configurations where a trade-off between reachability and stability is expected.
- **Extreme region (0.40–0.70):** configurations used to explore potential stability limits.

For each rover mass level, the manipulator mass is calculated directly from the selected ratio value.

3.4.3 Representative Manipulator Postures

The stability of rover–manipulator systems is strongly affected by manipulator deployment. To capture the influence of arm extension without exploring the entire manipulator configuration space, four representative manipulator postures are defined. These postures are illustrated conceptually in Table 3.X.

3.4.4 Rover-Manipulator Configuration Space

After defining rover scaling levels, arm ratio levels, and representative manipulator postures, rover–manipulator systems are generated through parametric fusion. Let: Let R denote the set of rover configurations, A the set of arm ratio levels, P the set of manipulator postures, M the set of mounting placements, and T the set of terrain conditions.

The total configuration space can therefore be expressed as

$$C = R \times A \times P \times M \times T \tag{3.14}$$

Each configuration represents a unique rover–manipulator system operating under a specific terrain condition and manipulator deployment posture. This structured configuration space enables a systematic exploration of the interaction between rover architecture, manipulator scaling, and terrain conditions, providing a basis for evaluating reachable workspace and static stability across a wide range of planetary robotic system designs. The overall workflow for generating the rover–manipulator configuration space and conducting the subsequent performance evaluation is illustrated in Figure X.

3.5 Analytical Stability Method

To evaluate whether a rover–manipulator system can safely perform manipulation tasks without risking tip-over, an analytical stability modelling framework is developed. In rover-mounted manipulation systems, the feasible workspace of the manipulator is not determined solely by its kinematic structure. As the manipulator extends, the position of the overall system centre of mass (CoM) changes relative to the rover support polygon, potentially reducing platform stability. Therefore, stability constraints must be considered when analysing the reachable workspace of rover–manipulator configurations. In this study, the stability analysis combines a geometry-based stability model with a simplified moment-based capability model. The geometry-based model is used as the primary method for determining whether a configuration is statically feasible, due to its computational efficiency and suitability for large-scale comparative evaluation across different rover architectures and terrain conditions. In addition, a simplified moment-based formulation is introduced to interpret the remaining stability margin in terms of allowable interaction load, providing a task-oriented perspective on the manipulation capability of each configuration, while also allowing the framework to be extended to incorporate additional moment contributions in future analyses.

3.5.1 Geometry-Based Stability Model

For each rover–manipulator configuration, static stability is evaluated by computing the global centre of mass (CoM) of the simplified rover–manipulator system and checking its position relative to the rover support polygon. Following the assumptions defined in Section 3.1, the rover body is simplified as a single rigid body with uniformly distributed mass. The centre of mass of the rover is therefore assumed to coincide with the geometric centre of the rover body, which is defined as the origin of the rover base coordinate frame:

$$\mathbf{r}_{rover} = \mathbf{r}_b \tag{1}$$

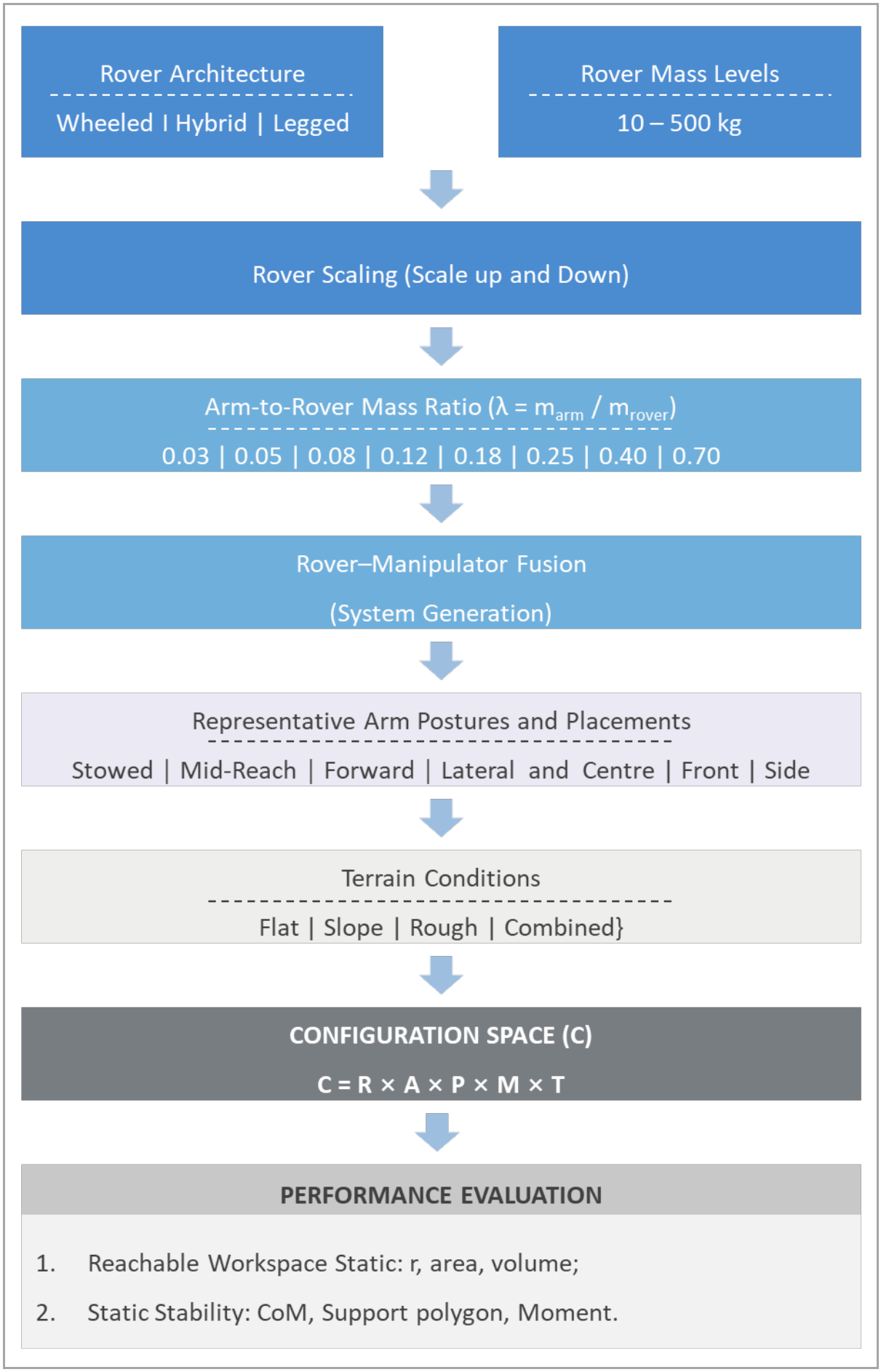

Figure 3.4: Enter Caption

where $\mathbf{r}_b = [0,0,0]^T$ denotes the origin of the rover base frame located at the geometric centre of the rover platform.

$$\mathbf{r}_{rover} = \mathbf{r}_b \tag{1}$$

The manipulator is modelled at link level. Under the uniform mass distribution assumption, each manipulator link is approximated as a rigid segment whose centre of mass lies at the geometric midpoint of the link. For a link of length L_i, the local centre-of-mass position defined in the link coordinate frame is therefore given by

$$\mathbf{r}_{c,i} = \begin{bmatrix} L_i/2 \\ 0 \\ 0 \end{bmatrix} \tag{2}$$

where the direction of the midpoint vector follows the principal axis of the link frame.

The position of the link centre of mass expressed in the rover base frame is obtained through forward kinematics using the homogeneous transformation matrix

$$^0\mathbf{r}_{c,i} = {}^0\mathbf{T}_i(\mathbf{q})\,\mathbf{r}_{c,i} \tag{3}$$

where ${}^0\mathbf{T}_i(\mathbf{q})$ represents the transformation from the rover base frame to the i-th link frame under the joint configuration $\mathbf{q}$.

Using the positions of all link centres of mass, the equivalent centre of mass of the manipulator is computed as

$$\mathbf{r}_{arm} = \frac{\sum_{i=1}^{n} m_i \, {}^0\mathbf{r}_{c,i}}{\sum_{i=1}^{n} m_i} \tag{4}$$

where m_i denotes the mass of link i and n is the total number of manipulator links.

Finally, the global centre of mass of the rover–manipulator system is obtained by combining the rover body and manipulator masses

$$\mathbf{r}_{CoM} = \frac{m_{rover}\mathbf{r}_{rover} + m_{arm}\mathbf{r}_{arm}}{m_{rover} + m_{arm}} \tag{5}$$

where

$$m_{arm} = \sum_{i=1}^{n} m_i$$

For a rover, the support polygon is defined by the convex hull formed by all wheel–ground contact points. Let the contact points be

$$\mathbf{p}_i = [x_i, y_i]^T, \quad i = 1, \ldots, k$$

where k denotes the number of wheel contacts with the terrain.

The projection of the global centre of mass onto the ground plane is given by

$$\mathbf{r}_{CoM}^{proj} = \begin{bmatrix} x_{CoM} \\ y_{CoM} \end{bmatrix} \tag{6}$$

Static stability is satisfied when the projected centre of mass lies inside the support polygon.

To quantify the degree of stability, the Static Stability Margin (SSM) is defined as the minimum distance between the projected centre of mass and the edges of the support polygon

$$SSM = \min_{j} d(\mathbf{r}_{CoM}^{proj}, e_j) \tag{7}$$

where e_j denotes the j-th edge of the support polygon and $d(\cdot)$ represents the perpendicular distance from the projected centre of mass to that edge.

Each edge e_j is defined by two adjacent vertices of the support polygon, denoted as

$$\mathbf{v}_j = [x_j, y_j]^T, \quad \mathbf{v}_{j+1} = [x_{j+1}, y_{j+1}]^T$$

The perpendicular distance from the projected centre of mass $\mathbf{r}_{CoM}^{proj}$ to the edge e_j is computed as

$$d(\mathbf{r}_{CoM}^{proj}, e_j) = \frac{\left|(\mathbf{v}_{j+1} - \mathbf{v}_j) \times (\mathbf{r}_{CoM}^{proj} - \mathbf{v}_j)\right|}{\|\mathbf{v}_{j+1} - \mathbf{v}_j\|} \tag{8}$$

where the numerator represents the magnitude of the two-dimensional cross product and the denominator corresponds to the length of the edge.

A positive value of SSM indicates that the configuration is statically stable, while $SSM = 0$ corresponds to the tipping boundary where the projected centre of mass lies exactly on one edge of the support polygon.

The above stability evaluation procedure is repeated for each sampled rover–manipulator configuration generated by the parametric scaling framework, enabling a systematic comparison of reachable workspace and stability characteristics across different rover architectures and manipulator configurations.

3.5.2 Moment-Based Load Capability Estimation

While the geometry-based stability model determines whether a configuration is statically feasible, it does not directly indicate the level of external interaction force that the rover–manipulator system can sustain. To provide a more intuitive interpretation of the remaining stability reserve and enable further extension of the stability analysis, a simplified moment-based formulation is introduced.

When an external force is applied at the manipulator end-effector, the rover–manipulator system may experience a tipping tendency around the boundary of the support polygon. The stability of the system can therefore be interpreted in terms of the restoring moment generated by gravity about the potential tipping axis.

The total weight of the rover–manipulator system is expressed as

$$W = Mg \tag{9}$$

where M denotes the total mass of the rover–manipulator system and g represents the gravitational acceleration. In this study, lunar gravity is adopted with

$$g = 1.62\,\mathrm{m/s^2}.$$

From the geometry-based stability analysis, the Static Stability Margin (SSM) represents the minimum distance between the projected centre of mass and the boundary of the support polygon. This margin corresponds to the effective lever arm between the system weight and the potential tipping axis. Therefore,

$$d = SSM \tag{10}$$

The restoring moment generated by gravity about the tipping axis can then be expressed as

$$M_g = Wd \tag{11}$$

where d corresponds directly to the stability margin obtained from the geometry-based analysis.

This formulation provides a physical interpretation of the geometric stability margin: the larger the value of d, the greater the gravitational restoring moment that resists tipping. The remaining stability reserve can therefore be interpreted as the maximum moment that can be counteracted before the system reaches the tipping boundary.

In practical manipulation tasks, external interaction forces applied at the manipulator end-effector may generate an overturning moment about the same tipping axis. Let h denote the perpendicular distance between the line of action of the external force and the tipping axis. The maximum allowable external force that can be sustained without causing tip-over can therefore be approximated by balancing the external moment with the gravitational restoring moment:

$$F_{max} = \frac{Wd}{h} \tag{12}$$

where F_{max} represents the maximum allowable end-effector interaction force. This relationship provides a direct interpretation of how the geometric stability margin translates

into manipulation capability: configurations with larger stability margins or greater system weight can tolerate larger interaction forces, while configurations with smaller margins become more susceptible to tipping during manipulation.

3.6 Active Posture Adjustment Modelling

Active posture adjustment is introduced to regulate the configuration of the rover–manipulator system under different control priorities, with the aim of probing the achievable boundary between reachability and static stability. Rather than being treated as a single optimisation policy, the adjustment framework is organised into two objective-biased modes: a stability-first mode, which prioritises stability recovery and preservation, and a reach-biased boundary mode, which prioritises reach extension while enforcing the same stability constraint. These two modes are used as boundary-probing strategies for comparative evaluation, rather than as a pair of mathematically symmetric optimisation algorithms.

In both modes, the active suspension adjustment variables are defined as

$$q = [\phi, \theta, \Delta x, \Delta y, \Delta z]^T$$

where ϕ and θ denote rover roll and pitch compensation, and $\Delta x, \Delta y, \Delta z$ denote equivalent translational suspension adjustments. In the present framework, the translational variables are introduced as abstract equivalent degrees of freedom to represent the potential effect of active structural reconfiguration or centre-of-mass repositioning. They do not necessarily correspond to a common mechanism in existing rover platforms, but are used here to capture the geometric effect of active mass-centre relocation on reachability and stability.

The reachable distance of the system is defined as the Euclidean distance between the manipulator flange position and the rover reference centre of mass:

$$R^{sys} = \| \, p_{flange} - p_{rover,ref} \, \|$$

For both adjustment modes, feasibility is evaluated using the same static stability condition:

$$SSM_{2D} \geq 0$$

where SSM_{2D} is the signed minimum distance between the projected system centre of mass and the support polygon boundary. A positive value indicates that the projected centre of mass lies within the support region, while a negative value indicates static instability.

The two strategies share the same variable set, feasibility criterion, and boundary-refinement principle, but differ in their initial prioritisation logic. The stability-first

strategy follows a hierarchical adjustment sequence that first improves stability and then expands reach only if feasible. In contrast, the reach-biased boundary strategy first selects a suspension boundary direction that is favourable to reach extension and then searches along that direction for the furthest feasible stable point. Since both strategies are heuristic and direction-constrained, the resulting solutions should be interpreted as practical feasible boundary configurations rather than globally optimal solutions.

To improve comparability between the two objective-biased modes, a unified tolerance framework is introduced. A mount-aware reference length L_{ref} is first defined according to the dominant working direction associated with the current mount configuration. Along this direction, the corresponding relevant support boundary is identified, and the shortest Euclidean distance from the reference point to that boundary is computed. This reference length has the same point-to-boundary distance interpretation as SSM_{2D}, but serves as a geometric scaling quantity rather than an instantaneous stability measure. Based on this reference scale, a dimensionless tolerance ratio λ_{tol} is introduced and the tolerance band is defined as

$$\delta = \lambda_{tol} L_{ref}$$

This formulation avoids the use of fixed absolute thresholds and allows the stopping conditions of both strategies to be interpreted relative to the same mount-dependent support scale.

3.6.1 Stability-First Adjustment Strategy

The stability-first strategy is designed to prioritise stability improvement before any attempt is made to expand system reach. The process begins from the nominal rover–manipulator configuration, for which the original static stability and original system reach are first evaluated.

Attitude Compensation by Pitch and Roll

In the first stage, only the rover attitude variables ϕ and θ are adjusted. A terrain-compensation initial estimate is first constructed by counteracting the terrain slopes within the allowable roll and pitch limits. Starting from this initial estimate, a lightweight local search is then performed to identify a better pitch–roll combination.

The pitch–roll search does not directly maximise the stability margin. Instead, it primarily minimises the offset of the projected system centre of mass in the rover plane, such that the projected centre of mass is driven as close as possible to the rover reference centre. Among candidates with similar projection offset, the one with the larger SSM_{2D} is preferred. Therefore, the pitch–roll stage can be interpreted as a geometric stability compensation process based on projected centre-of-mass centralisation, with stability

margin used as a secondary tie-breaking indicator.

It should be noted that the stability-oriented bias of this strategy is not solely a consequence of the search sequence itself, but also of the modelling assumption adopted in this study. In the present framework, pitch and roll are treated as the most physically plausible primary posture-regulation variables for stability improvement, while translational adjustment is treated as a secondary mechanism for reach extension or additional centre-of-mass repositioning. Accordingly, the resulting stability bias is framework-dependent rather than universally intrinsic to all rover architectures.

Translational Adjustment Along the End-Flange Direction

After pitch–roll optimisation, the flange position and the updated system reach are recomputed. A translational adjustment direction is then constructed from the current rover centre of mass to the manipulator flange:

$$u = \frac{p_{flange} - p_{rover\_com}}{\| p_{flange} - p_{rover\_com} \|}$$

-

Based on the sign of each component of u, a directional translational boundary vector is selected within the allowable translational limits. The translational adjustment is then parameterised as

$$d(\lambda) = \lambda d_{dir}, \lambda \in [0, 1]$$

where d_{dir} is the predefined translation direction.

At this stage, the optimisation does not rely solely on the binary condition $SSM_{2D} \geq 0$, but also uses a stability-oriented tolerance condition. The projected centre of mass is considered to have entered a sufficiently stabilised central region when

$$\| p_{\mathrm{CoM}}^{proj} - p_{target} \| \leq \delta_{stab}$$

where p_{target} is the target point in the rover ground plane. In the present implementation, this target is taken as the rover planar reference origin, giving

$$\| p_{\mathrm{CoM}}^{proj} \| \leq \delta_{stab}$$

with $\delta_{stab} = \lambda_{tol} L_{ref}$ when a shared tolerance ratio is adopted.

Two cases are then considered.

If the system is sufficiently stabilised after pitch–roll compensation, translational adjustment is used in reach extension mode. In this case, the system is translated along the end-flange direction to increase reach while remaining stable. The objective is to

identify the maximum feasible translation:

$$\lambda^* = \max \lambda \in [0,1]\{\lambda \mid SSM2D(\lambda) \geq 0\}$$

If the full boundary displacement remains stable, $\lambda = 1$ is directly accepted. Otherwise, binary search is used to locate the maximum stable boundary point.

If the system is still unstable, or remains outside the required stability tolerance region after pitch–roll compensation, translational adjustment is used in stability recovery or reinforcement mode. In this case, translation is applied in the opposite direction:

$$d(\lambda) = -\lambda d_{dir}, \lambda \in [0,1]$$

The objective is then to identify the minimum translation required either to restore feasibility or to move the projected centre of mass into the prescribed central tolerance region. In the feasibility-restoration case, this can be written as

$$\lambda^* = \min \lambda \in [0,1]\{\lambda \mid SSM2D(\lambda) \geq 0\}$$

and, more generally, the translation may continue until the stability-oriented tolerance condition is satisfied. If no acceptable solution exists within the maximum allowable reverse translation, the configuration is considered unrecoverable within the active suspension limits.

Boundary Refinement

For both extension and recovery cases, the scalar parameter λ is determined through one-dimensional boundary search. A fixed binary refinement with $N = 7$ iterations is used, yielding a resolution of approximately

$$\frac{1}{2^7} \approx 0.78\%$$

which is sufficient for approximating the feasible stability boundary with negligible influence on the comparative reachability analysis.

The final compensated configuration is then obtained by applying the selected pitch, roll, and translational adjustment, after which the compensated mount position, system centre of mass, system reach, and final SSM_{2D} are recomputed in a closed loop.

Overall, the stability-first strategy can be interpreted as a hierarchical feasibility-oriented procedure: it first improves stability through pitch–roll adjustment, then either expands reach up to the stability boundary or, if necessary, applies reverse translation to recover or reinforce stability with minimum reach loss.

3.6.2 Reach-Biased Boundary Adjustment Strategy

The reach-biased boundary strategy is designed to favour reach extension more directly. Instead of first performing explicit stability-centred pitch–roll optimisation, this strategy first constructs a suspension boundary direction that is heuristically favourable to extending the manipulator reach, and then searches along that direction for the furthest stable configuration.

Reach-Biased Boundary Direction Construction

As in the stability-first strategy, the original stability and original system reach are first evaluated for the nominal configuration. A direction vector is then defined from the rover centre of mass to the manipulator flange:

$$\mathbf{v} = p_{flange} - p_{rover\_com}$$

This vector represents the current end-flange extension direction relative to the rover body. Based on the sign of each component of $\mathbf{v}$, an extreme-direction boundary is selected for all active suspension variables, including roll, pitch, and translational shifts. For each degree of freedom, the upper or lower allowable bound is selected according to the sign of the corresponding direction component. This produces a predefined reach-biased boundary vector

$$q_{dir} = [\phi_{dir}, \theta_{dir}, \Delta x_{dir}, \Delta y_{dir}, \Delta z_{dir}]^T$$

which heuristically represents a suspension posture favourable to further reach extension.

This construction is not derived from gradient information or global optimisation. Instead, it is a sign-based heuristic that converts the current flange extension direction into a feasible suspension boundary direction.

One-Dimensional Feasible Boundary Search

Once the reach-biased direction has been defined, the candidate adjustment is parameterised as

$$q(\lambda) = \lambda q_{dir}, \lambda \in [0, 1]$$

where $\lambda = 0$ corresponds to no compensation and $\lambda = 1$ corresponds to the full reach-biased suspension boundary configuration.

The strategy then searches for the largest feasible stable point along this predefined direction:

$$\lambda^* = \max_{\lambda \in [0,1]} \{\lambda \mid SSM_{2D}(q(\lambda)) \geq 0\}$$

In addition to feasibility, a reach-oriented tolerance condition is introduced. The

candidate is considered sufficiently close to the admissible stability boundary when

$$0 \leq SSM_{2D}(q(\lambda)) \leq \delta_{reach}$$

where $\delta_{reach} = \lambda_{tol} L_{ref}$ when the same tolerance ratio is used for both biased modes. Once the solution enters this boundary-adjacent tolerance band, the search may be terminated without requiring convergence to the exact limiting boundary.

The search is therefore performed in two stages. First, a coarse scan is conducted over a small set of uniformly distributed λ samples in $[0, 1]$. Then, if a transition from stable to unstable is detected, binary refinement is applied between the last stable point and the first unstable point to approximate the maximum feasible stable boundary or an acceptable near-boundary solution.

The objective here is not to optimise a continuous weighted score, but to locate the furthest admissible point on the reach-biased direction while satisfying the same feasibility constraint and entering the prescribed boundary tolerance band.

Fallback Mechanism and Interpretation

If a stable candidate is found along the reach-biased direction, the corresponding configuration is adopted as the compensated posture. If no feasible stable solution exists along that direction, the strategy falls back to the stability-first procedure. This fallback mechanism ensures that the adjustment process does not terminate at an infeasible state when the heuristically selected reach-biased path fails to contain a stable solution.

Therefore, the reach-biased boundary strategy should be interpreted as a practical reach-oriented boundary-probing method rather than a globally optimal reachability solver. Its main role in this study is to expose the reach-favourable side of the system capability envelope under the same feasibility criterion.

3.6.3 Remarks on Method Characteristics and Limitations

Several characteristics of the active posture adjustment framework should be noted.

First, neither strategy performs global optimisation in the full five-dimensional adjustment space. Both strategies reduce the problem to direction-constrained one-dimensional searches after defining a preferred compensation direction or sequence. This choice improves interpretability and computational efficiency, but also means that the obtained solutions are locally or directionally feasible rather than globally optimal.

Second, in the stability-first strategy, pitch–roll compensation is driven primarily by projected centre-of-mass centralisation rather than direct maximisation of SSM_{2D}. This provides a clear geometric interpretation, but it also means that the strategy uses a stability-related proxy objective in the attitude stage.

Third, in the reach-biased boundary strategy, the compensation direction is generated heuristically from the sign of the current end-flange direction. As a result, the selected path is reach-favourable in an engineering sense, but is not guaranteed to be the best possible reach-improving direction in the full adjustment space.

Fourth, the translational variables in x, y, z are introduced as equivalent configuration-adjustment degrees of freedom. They represent the geometric effect of active reconfiguration or centre-of-mass relocation, but should not be interpreted as a claim that all rover platforms possess such mechanisms in practice.

Finally, the two strategies are not intended to form a perfectly symmetric optimisation pair. They are instead used as two objective-biased probing modes for identifying the practical capability boundaries of rover–manipulator systems. Their comparability arises from the use of the same variable set, the same feasibility condition, and the same tolerance band defined relative to a common reference scale, rather than from identical objective functions or mathematically equivalent optimisation structure.

3.7 System Framework

To support the large-scale generation and evaluation of rover–manipulator configurations and the validation of the analytical modelling results, the proposed methodology is implemented through a modular system framework. The overall architecture of the framework is illustrated in Figure 3.5.

The framework is organised into three implementation layers: a Python-based service layer, a MATLAB-based analytical engine and static simulation layer, and a MATLAB–ROS2–Gazebo integrated simulation layer. The MATLAB-based analytical and static simulation layer forms the core of the framework, where configuration generation, analytical evaluation, and geometric validation are performed. The Python layer provides basic workflow support for the framework, while the integrated simulation layer offers additional environment-level validation. A lightweight Python layer is used to organise configuration inputs and coordinate the execution of the analytical calculations. Through this layer, rover scaling rules, manipulator parameters, terrain conditions, and representative arm postures are defined and passed to the analytical engine for large-scale configuration generation and evaluation. The generated results can also be organised and presented in a structured form to support configuration comparison and subsequent analysis. The core analytical computations are performed within a MATLAB-based analytical engine, which generates and evaluates large numbers of rover–manipulator configurations using the parametric scaling and stability models introduced in the previous sections. Within the same environment, a single-scenario static simulation module is used to verify the geometric behaviour of representative configurations. Under stationary rover conditions, the simulation visualises the rover–manipulator geometry, centre-of-mass movement, and

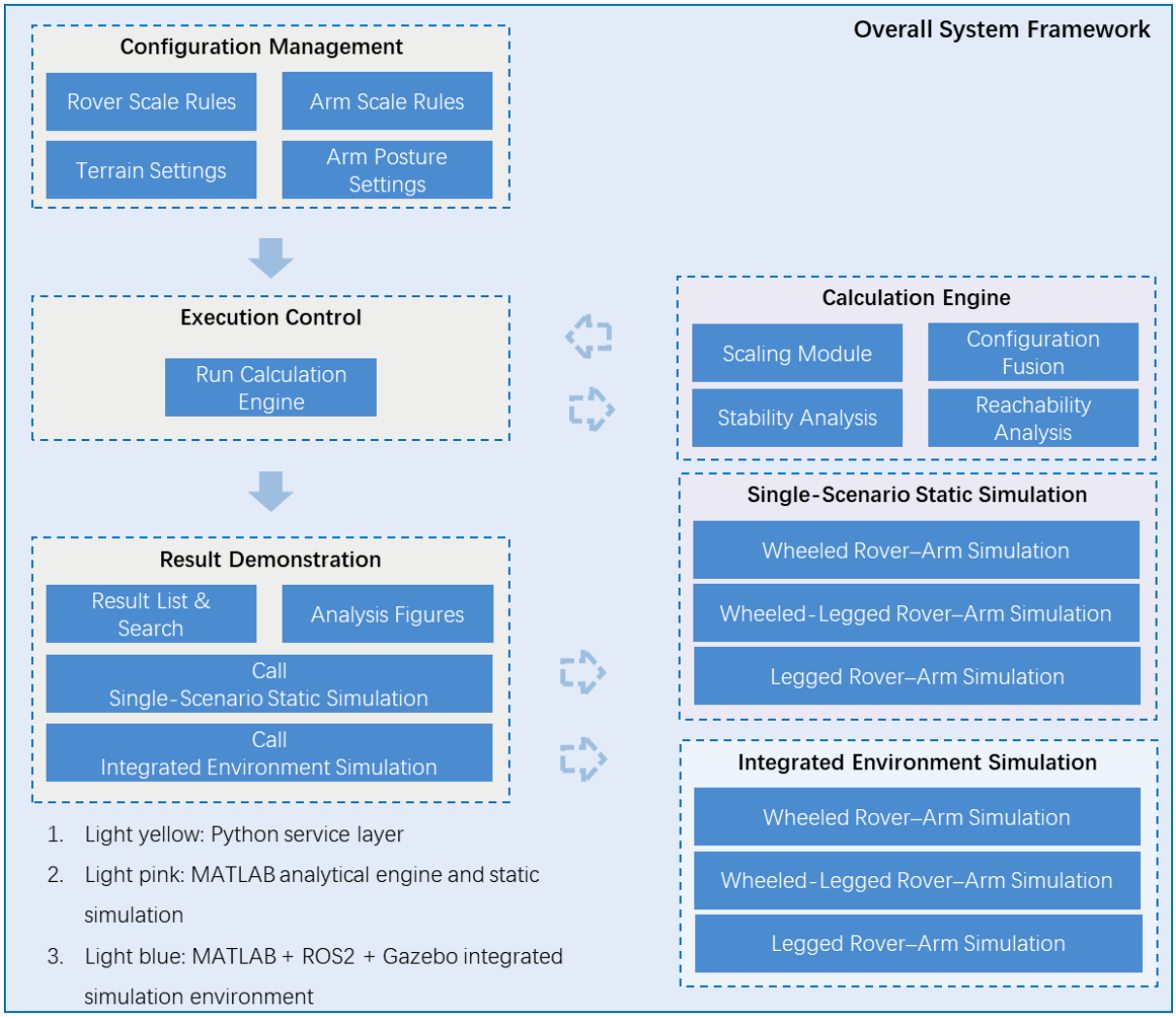

Figure 3.5: Overall System Framework

support polygon relationships as the manipulator deploys, providing geometric verification of the analytical stability modelling. To further validate the analytical results in a more complete robotic environment, selected configurations can be examined within a MATLAB–ROS2–Gazebo integrated simulation environment. In this stage, rover–manipulator systems are placed within terrain scenes and simulated using ROS2 and Gazebo, allowing the analytical predictions to be observed within a more realistic robotic simulation context. By separating the framework into these three layers, the system supports efficient large-scale configuration evaluation while enabling simulation-based validation of representative system behaviours.

3.7.1 Python-based service layer

The configuration management and execution control layer forms the interface between the user-defined system settings and the analytical calculation engine. This layer is implemented using Python and functions as a lightweight service platform responsible for organising configuration inputs, triggering calculation processes, and presenting analysis results. In this layer, several key configuration settings are defined to construct the design space explored in the study. These settings include rover scaling rules, manipulator scaling rules, terrain conditions, and representative manipulator posture configurations. Together, these parameters define the input space from which rover–manipulator system configurations are generated by the calculation engine. Once the configuration settings are defined, the Python layer initiates the execution of the analytical calculation engine. The engine then performs large-scale configuration generation and stability evaluation according to the rules defined in the previous methodological sections. After the calculation process is completed, the same layer is used for result management and visualisation. Generated configuration results can be organised into searchable result lists and analysed through a series of statistical and comparative figures. This functionality allows different rover–manipulator configurations to be explored interactively, supporting the comparative evaluation of reachable workspace and system stability. In addition, the configuration management layer provides interfaces for invoking scenario simulations. Selected configurations identified through the analytical evaluation can be forwarded to either the single-scenario static simulation module or the integrated environment simulation module for further demonstration.

3.7.2 MATLAB-based analytical engine

The calculation engine forms the core computational component of the proposed system framework. It is responsible for generating rover–manipulator configurations and evaluating their stability and reachability characteristics using the analytical models introduced in the previous sections. The internal workflow of the calculation engine

is illustrated in Figure 3.6, which presents the complete configuration generation and evaluation pipeline. The engine is organised into three functional layers: the model generation layer, the system configuration layer, and the performance evaluation layer. These layers progressively transform the initial rover reference models into fully evaluated rover–manipulator system configurations.

1. Model Generation Layer

The model generation layer produces scalable rover platform models based on predefined parametric scaling rules. Three representative rover architectures are considered: wheeled rovers, wheeled–legged rovers, and legged rovers. For each architecture, a reference rover geometry is first defined. The parametric scaling module then generates scaled rover variants by applying the rover scaling rules introduced in the parametric modelling stage. During this process, constraint validation is performed to ensure that the generated rover configurations remain physically feasible. In addition, geometric visualisation functions are used to verify the generated rover structures. Once a rover geometry passes the constraint validation stage, the rover stability parameters are initialised. These parameters include centre of mass location, and the corresponding support polygon determined by the contact points with the flat terrain. The output of this layer is a set of rover platform configurations for each mobility architecture. These sets are then merged into a unified rover configuration set, which forms the basis for the subsequent rover–manipulator system generation process.

2. System Configuration Layer

The system configuration layer constructs complete rover–manipulator system configurations by progressively combining rover platforms, manipulators, mounting positions, arm postures, and terrain conditions. First, the manipulator scaling module generates manipulator models based on a predefined reference arm geometry together with the rover configuration parameters. Since the manipulator design is coupled with the rover platform size, the scaling process considers rover parameters when generating the manipulator variants. Parameter validation is then performed to ensure that the generated manipulator configurations remain consistent with the rover platform constraints. Next, the manipulator mount fusion module combines the generated manipulators with the rover platforms. Different mounting locations on the rover body are considered, producing rover–arm pre-mount configurations. For each configuration, system-level stability parameters are recalculated to reflect the updated mass distribution after the manipulator is attached. Following this step, the manipulator posture fusion module introduces representative arm deployment postures. These postures correspond to typical manipulator operating states such as stowed, partially deployed, and fully extended configurations. The system stability is recalculated for each posture to capture the influence of manipulator deployment on the rover centre of mass. Finally, the terrain fusion module integrates terrain conditions into the system configurations. Representative terrain conditions, including slopes and uneven ground surfaces, are applied to the rover–manipulator posture configurations. This

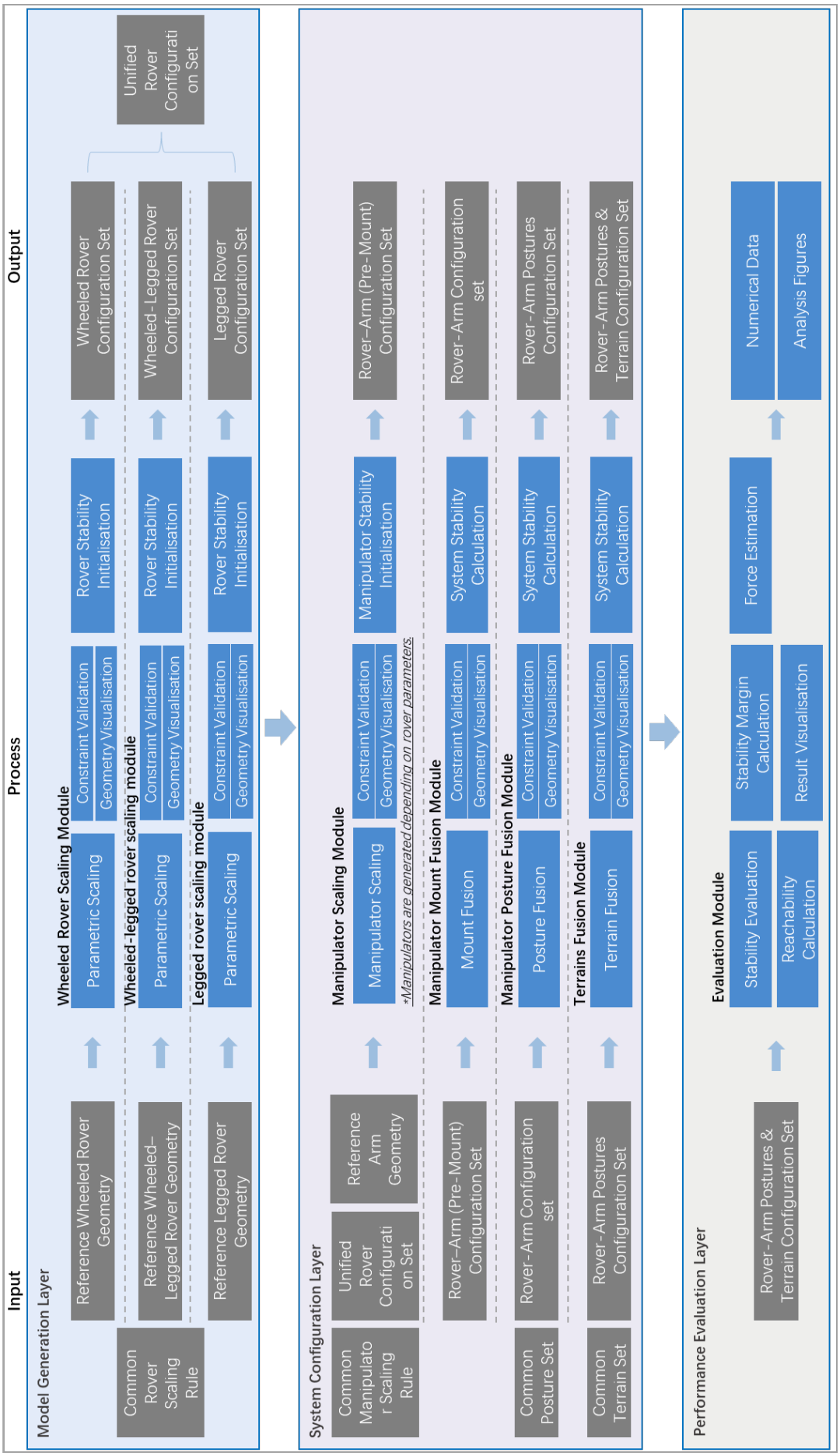

Figure 3.6: Matlab Analytical Engine and Simulation Framework

process produces a comprehensive set of rover–arm–terrain configurations that represent different environmental interaction scenarios.

3. Performance Evaluation Layer

The final stage of the calculation engine performs quantitative evaluation of the generated rover–manipulator configurations. In this layer, an evaluation module analyses each rover–arm–terrain configuration using the analytical stability models developed earlier in the methodology. The stability evaluation determines whether the system remains statically stable under the given configuration by examining the relationship between the projected centre of mass and the rover support polygon. In addition to the binary stability assessment, the static stability margin is calculated to quantify the remaining stability reserve of the system. A simplified force estimation module is also introduced to estimate the external interaction forces that can be sustained before the rover approaches the tipping boundary. Parallel to the stability analysis, the reachability of the manipulator flange is evaluated for each configuration. The flange position is expressed in the rover base frame and the corresponding reach distances are calculated. These reachability metrics are then combined with the stability indicators to produce a dataset describing the trade-off between manipulator reach capability and rover platform stability. The final outputs of the calculation engine include numerical datasets and visual analysis figures, which are subsequently used for comparative evaluation and result interpretation in the following sections.

3.7.3 MATLAB-based static simulation layer

While the calculation engine performs large-scale discrete evaluation across many rover–manipulator configurations, a complementary simulation module is introduced to validate the geometric consistency of the analytical modelling results. This module is referred to as the single-scenario static simulation. In this simulation mode, the rover base is assumed to remain stationary, and the focus is placed on the continuous deployment of the manipulator within a selected configuration. This allows the geometric evolution of the rover–manipulator system to be observed as the manipulator moves from a stowed posture to extended working postures. During the simulation process, the positions of the rover body, manipulator links, and system centre of mass are visualised together with the rover support polygon. This enables the geometric relationship between manipulator motion and rover stability to be examined, providing an intuitive verification of the analytical stability calculations. Unlike the configuration evaluation performed by the calculation engine, which analyses many discrete configurations independently, the single-scenario simulation emphasises continuous system behaviour within a single configuration. The purpose of this module is therefore not to replace the analytical evaluation but to provide geometric validation of the modelling assumptions and to confirm the physical feasibility

of the calculated stability results.

3.7.4 MATLAB–ROS2–Gazebo integrated simulation layer

In addition to the simplified static scenario simulation, the framework also includes an integrated environment simulation module that provides an extended validation environment for the analytical modelling results. This module combines MATLAB-generated configuration information with external robotics simulation tools, including ROS2 and Gazebo. In this environment, selected rover–manipulator configurations are placed within terrain scenes, allowing the system behaviour predicted by the analytical models to be examined under more realistic environmental conditions. Compared with the simplified analytical representation used in the calculation engine and the geometric verification provided by the single-scenario static simulation, the integrated environment simulation represents the rover, manipulator, and terrain within a more engineering-realistic and environment-complete context. In this environment, the ROS2-based simulation can call the MATLAB analytical engine to compute key stability metrics, such as the system centre of mass and the support polygon, allowing the analytical modelling assumptions and predicted behaviours to be examined within a more realistic robotic simulation setting. The integrated environment simulation serves to examine whether the conclusions derived from the simplified analytical models remain consistent when represented within a more realistic system context.

3.8 Comparative Evaluation

The analytical modelling framework developed in the previous sections generates a comprehensive configuration dataset describing the reachability and stability characteristics of rover–manipulator systems under varying design parameters and terrain conditions. While the analytical model evaluates the feasibility and performance of individual configurations, the objective of this study is to understand how different rover mobility architectures influence system-level manipulation capability when integrated with robotic manipulators. To address this objective, a structured comparative evaluation framework is introduced to analyse the generated dataset from multiple statistical perspectives. The comparative evaluation is organised into three complementary stages. First, an architecture-level analysis is conducted to establish the baseline capability of each rover mobility architecture in terms of stability feasibility, maximum reachable distance, and stability reserve. Second, the adaptability of rover architectures to configuration disturbances is examined by analysing system behaviour under variations in terrain inclination, manipulator scaling, mounting position, and representative manipulator postures. Finally, the reachability–stability trade-off inherent in rover–manipulator systems is investigated by examining how system

stability evolves as the operational reach of the manipulator increases. Through this three-layer evaluation framework, the analysis aims to reveal how rover platform geometry and mobility architecture influence the balance between manipulation capability and system stability.

3.8.1 Performance Metrics Definition

To enable consistent comparison across rover–manipulator configurations, several performance metrics are used throughout the comparative evaluation. These metrics are derived from the configuration dataset generated by the analytical stability model and describe the feasibility, reach capability, and stability reserve of rover–manipulator systems.

Let C denote the full configuration dataset and i represent an individual rover–manipulator configuration. The stability state of each configuration is represented by a binary variable $Stable_i$, where a value of 1 indicates that the system centre of mass remains within the support polygon and the configuration satisfies the static stability constraint, while a value of 0 indicates an unstable configuration.

The stable configuration ratio represents the proportion of configurations that remain statically feasible within a given configuration set:

$$SR = \frac{\sum_i Stable_i}{|C|} \tag{3.15}$$

This metric reflects the probability that a rover–manipulator configuration maintains static stability under the evaluated operating conditions.

The maximum stable reach represents the furthest operational distance that can be achieved while maintaining static stability. Let R_i^{sys} denote the system reach of configuration i, defined as the Euclidean distance between the rover base frame and the manipulator flange position. The maximum stable reach can therefore be expressed as

$$R_{\max} = \max_{Stable_i=1} R_i^{sys} \tag{3.16}$$

which represents the furthest reachable distance supported by the rover–manipulator system without violating the stability constraint.

To characterise the stability reserve of a configuration set, the average static stability margin is also evaluated. Let SSM_i denote the static stability margin of configuration i, defined as the minimum distance between the projected system centre of mass and the boundary of the support polygon. The average stability margin is therefore expressed as

$$AvgSSM = \frac{1}{|C|} \sum_i SSM_i \tag{3.17}$$

In addition to the geometric stability margin, the gravitational restoring moment about the potential tipping edge is also used to provide a physical interpretation of the system's resistance to tip-over. When the projected centre of mass is located at a distance d_i from the tipping boundary, the restoring moment generated by gravity can be approximated as

$$M_i = W \cdot d_i \tag{3.18}$$

where $W = Mg$ represents the total system weight and d_i corresponds to the geometric stability margin associated with configuration i. This relationship establishes a direct connection between the geometry-based stability model and the moment-based stability interpretation.

To characterise the overall moment-based stability reserve of a configuration set, the average restoring moment can be defined as

$$AvgM = \frac{1}{|C|} \sum_i M_i \tag{3.19}$$

Since the restoring moment is directly proportional to the geometric stability margin under constant system weight, the two metrics provide equivalent stability information. However, the moment-based representation offers a more intuitive physical interpretation of the rover's resistance to tipping.

These metrics are used consistently in the following analyses to evaluate rover architecture capability, disturbance adaptability, and the reachability–stability trade-off.

3.8.2 Architecture-Level Performance Overview

At the first level of analysis, the configuration dataset is grouped according to rover mobility architecture in order to establish the baseline capability of different rover platforms.

The performance of each rover architecture is evaluated using three metrics introduced in Section 3.8.1

First, the Stable Configuration Ratio (SR) measures the proportion of configurations that satisfy the static stability constraint. This indicator reflects the overall stability feasibility of a rover architecture across the explored configuration space and represents the probability that the rover–manipulator system remains stable under varying manipulator configurations and terrain conditions.

Second, the Maximum Stable Reach ($R_{\max}$) represents the furthest operational reach that can be achieved while maintaining static stability. This metric characterises the maximum manipulation capability supported by a given rover architecture without violating the tipping constraint.

Third, the Average Static Stability Margin ($AvgSSM$), together with its moment-

based interpretation through the Average Restoring Moment ($AvgM$), describes the overall stability reserve of the rover–manipulator system. While the geometric stability margin quantifies the distance between the projected centre of mass and the tipping boundary, the restoring moment provides a physical interpretation of the system's resistance to tip-over. Larger values therefore indicate stronger stability capacity during manipulation tasks.

By analysing these indicators together, the architecture-level evaluation provides an integrated performance profile of different rover mobility architectures. Specifically, the analysis reveals how different rover platforms balance stability feasibility, manipulation reach capability, and stability reserve when integrated with robotic manipulators. These baseline observations establish a reference for the subsequent analyses, where the influence of configuration disturbances and the reachability–stability trade-off are further investigated.

3.8.3 Disturbance adaptability analysis

In the second stage of the evaluation, the configuration dataset is analysed from the perspective of disturbance conditions introduced by manipulator integration and terrain variation. In practical rover–manipulator operations, system performance is influenced by variations in environmental conditions and manipulator configurations. In this study, these variations are treated as disturbance categories within the configuration space, including terrain inclination, manipulator scaling, mounting position, and representative manipulator postures.

Rather than isolating variables through strict control experiments, the disturbance analysis evaluates rover performance statistically by grouping configurations according to specific disturbance conditions. For each disturbance category, configuration subsets corresponding to different disturbance states are extracted from the dataset and evaluated using the same performance metrics defined in Section 3.8.1.

First, the Stable Configuration Ratio (SR) is used to examine how frequently rover–manipulator configurations remain statically stable under different disturbance conditions. Changes in SR across disturbance states indicate the sensitivity of rover architectures to environmental or configuration variations.

Second, the Maximum Stable Reach ($R_{\max}$) is analysed to determine how disturbance conditions influence the achievable operational reach while maintaining stability. This metric reflects how different rover platforms preserve manipulation capability when manipulator configuration or terrain conditions change.

Third, the Average Static Stability Margin ($AvgSSM$), together with the Average Restoring Moment ($AvgM$), is used to characterise the stability reserve of the system under different disturbance conditions. While the geometric stability margin measures the distance between the projected centre of mass and the tipping boundary, the restoring

moment provides a physical interpretation of the rover's resistance to tip-over.

By analysing these metrics across disturbance categories, the adaptability of rover architectures to configuration and environmental variations can be characterised. This stage therefore reveals how the geometric and structural properties of different rover platforms influence their ability to maintain stability and manipulation capability under varying operational conditions.

3.8.4 Reachability–stability trade-off analysis

Beyond disturbance adaptability, the final stage of the evaluation focuses on the fundamental reachability–stability trade-off inherent in rover–manipulator systems. When the manipulator extends to increase the operational reach of the system, the overall centre of mass of the rover–manipulator system shifts relative to the support polygon, increasing the tipping moment acting on the rover platform. Consequently, reachability and stability represent competing performance objectives that must be balanced when designing mobile manipulation systems.

To investigate this relationship, the analysis examines how system stability evolves as the reachable distance of the manipulator increases. The system reach R^{sys} is used to represent the operational distance between the rover base frame and the manipulator flange, while the corresponding static stability margin (SSM) and restoring moment (M) describe the remaining stability reserve of the system.

First, the distribution of the Stable Configuration Ratio (SR) is examined across different reach ranges in order to determine how frequently configurations remain feasible as the manipulator extension increases. This analysis reveals the reach limits within which rover–manipulator systems can maintain stable operation.

Second, the variation of SSM and its moment-based interpretation through M is analysed as a function of system reach. These indicators describe how the stability reserve of the rover platform decreases as the manipulator extends further away from the rover body.

By analysing the relationship between reachable distance and stability reserve, the reachability–stability trade-off behaviour of different rover architectures can be characterised. Architectures that maintain larger stability margins and restoring moments at greater reachable distances exhibit a more favourable balance between manipulation capability and platform stability. Through this analysis, the influence of rover platform geometry and mobility architecture on the reachability–stability trade-off can therefore be systematically revealed.

Table 3.1: Rover configuration parameter definition

Parameter	**Scale**	**Description**
Rover ID	No	Unique identifier of the rover platform
Rover Name	No	Descriptive name of the rover platform
Mobility Type	No	Mobility architecture of the rover (e.g., wheeled, wheeled–legged, or legged)
Rover Mass	Yes	Total mass of the rover platform
Centre of Mass Position	Yes	Position of the rover centre of mass expressed as a 3D coordinate (x, y, z) in the rover base reference frame
Rover Length	Yes	Length of the rover chassis
Rover Width	Yes	Width of the rover chassis
Rover Height	Yes	Height of the rover body
Rover Clearance	Yes	Ground clearance of the rover body
Support Point Count	No	Number of ground contact points (wheels or legs)
Support Points	Yes	Coordinates of ground contact points defining the support polygon (relative to the rover base frame)
Active Suspension Enabled	No	Indicates whether active suspension is enabled
Chassis Active Roll Limit	No	Maximum allowable rotation about the longitudinal axis (x-axis), representing lateral tilt
Chassis Active Pitch Limit	No	Maximum allowable rotation about the lateral axis (y-axis), representing forward/backward tilt
Chassis Active Longitudinal Shift	Yes	Maximum forward/backward translation of the chassis relative to the support polygon (x direction)
Chassis Active Lateral Shift	Yes	Maximum left/right translation of the chassis relative to the support polygon (y direction)
Chassis Active Height Adjust	Yes	Adjustable vertical position of the rover chassis (z direction)
Mount Front	Yes	Manipulator mounting interface at the front of the rover (x, y, z) in the rover base frame
Mount Centre	Yes	Manipulator mounting interface at the centre of the rover (x, y, z) in the rover base frame
Mount Side	Yes	Manipulator mounting interface at the side of the rover (x, y, z) in the rover base frame

Table 3.2: Manipulator configuration parameter definition

Parameter	**Scale**	**Description**
Manipulator ID	No	Unique identifier of the manipulator model
Manipulator Name	No	Descriptive name of the manipulator model
Degrees of Freedom	No	Number of independent joints in the manipulator
Joint Count	No	Total number of manipulator joints
Link Count	No	Total number of manipulator links
Maximum Reach	Yes	Maximum distance from manipulator base to flange in the reference configuration
Total Manipulator Mass	Yes	Total mass of the manipulator structure excluding end-effector
Payload	Yes	Maximum payload capacity of the manipulator

Table 3.3: Manipulator kinematic and mass parameter definition (MDH-based)

Category	**Parameter**	**Scale**	**Description**
Configuration	Manipulator ID	No	Unique identifier of the manipulator model
Configuration	Joint Index (i)	No	Joint number in the serial kinematic chain
Geometry	a_{i-1} (mm)	Yes	Link length between joint $(i-1)$ and (i) (MDH parameter)
Geometry	α_{i-1} (deg)	No	Link twist angle between joint axes (MDH parameter)
Geometry	d_i (mm)	Yes	Offset along the joint axis (MDH parameter)
Kinematics	θ_i (deg)	No	Joint variable defining manipulator posture
Mass	Link Mass (kg)	Yes	Mass of each link including joint contribution
Mass	Link CoM Local (mm)	Yes	Local centre of mass of each link expressed in the link frame

Table 3.4: Lunar Regolith Physical Properties (Source: Apollo Mission Data)

Parameter	Symbol	Typical Value
Cohesion	c	$0.17 - 3.0$ kPa
Internal Friction Angle	ϕ	$30° - 45°$
Bulk Density	ρ	$1500 - 1800$ kg/m^3
Sinkage Exponent	n	1.1

Table 3.10: Terrain inclination scenarios used in the analysis

Terrain Type	**Roll (°)**	**Pitch (°)**
Flat	0	0
Longitudinal mild	0	5
Longitudinal moderate	0	10
Longitudinal steep	0	15
Lateral mild	5	0
Lateral moderate	10	0
Lateral steep	15	0
Combined mild	5	5
Combined moderate	10	10
Combined steep	15	15

Table 3.11: Representative lunar terrain environments used for simulation

Terrain	**Location**	**Lat**	**Lon**
Crater rim slope	Shackleton crater rim	XX	XX
Crater interior slope	Cabeus crater	XX	XX
Polar rough terrain	Malapert massif	XX	XX

Table 3.12: Rover scale configurations used in the study

Rover Scale ID	Rover Mass (kg)	Description
R1	10	Small robotic scout
R2	25	Lightweight exploration rover
R3	50	Medium robotic platform
R4	100	Standard planetary rover scale
R5	250	Heavy exploration rover
R6	500	Large robotic platform

Table 3.13: Manipulator-to-rover mass ratio configurations

Ratio ID	Mass Ratio (λ)	Design Region
A1	0.03	Very light manipulator
A2	0.05	Light manipulator
A3	0.08	Moderate-light configuration
A4	0.12	Balanced configuration
A5	0.18	Medium manipulator
A6	0.25	Heavy manipulator
A7	0.40	Extreme configuration
A8	0.70	Upper design boundary

Table 3.14: Representative manipulator deployment postures used for evaluation

Posture ID	Description	Purpose
P1	Stowed	Baseline configuration with minimal CoM shift
P2	Mid-reach	Nominal working configuration
P3	Full forward extension	Maximum forward reach and potential forward tip-over
P4	Lateral extension	Side extension for evaluating roll stability

Chapter 4

Framework Validation

4.1 Methodology

The primary objective of the validation process is to assess the fidelity of the developed mathematical model by comparing its simulated behavior against established operational performance characteristics of the real-world Mars Science Laboratory (MSL) rover, Curiosity. To achieve this, the simulation's results are benchmarked against the maximum static inclination angles without overturning reported in official technical literature.

The validation is structured into three distinct procedural steps, executed sequentially:

4.1.1 Step 1: Literature Research and Requirements Definition

Initially, extensive research was conducted in public NASA repositories and relevant academic publications to acquire two key categories of data:

1. **Reference Performance Metric:** Identification of the documented operational limits for the MSL rover regarding static stability. According to the report *"Mars Curiosity Rover Mobility Trends During the First Seven Years"* [70], the real-world Curiosity rover maintains stability and does not overturn at static inclination angles up to 45° in any direction relative to the gravity vector. This value serves as the quantitative benchmark for validating the simulation.

2. **3D Geometry and Physical Parameters:** Acquisition of a representative 3D CAD model [71] of the rover to determine the initial relative positions of components, which are prerequisites for calculating the system's center of mass (CM).

4.1.2 Step 2: Simplified Model Parameter Acquisition via SolidWorks

Due to the substantial complexity in determining the precise center of mass (CM) location for the complete MSL rover, which includes numerous high-density internal instruments and flexible harnesses, a simplified mechanical model was utilized for this study. The development of this simplified model relies on accurate dimensional data extracted from the high-fidelity CAD model using SolidWorks software.

The following geometric features were systematically measured (Figure 4.1):

- Coordinates of ground contact points for the six wheels;
- Precise relative positioning and extension reach of the robotic arm;
- Overall dimensions of the chassis and suspension links.

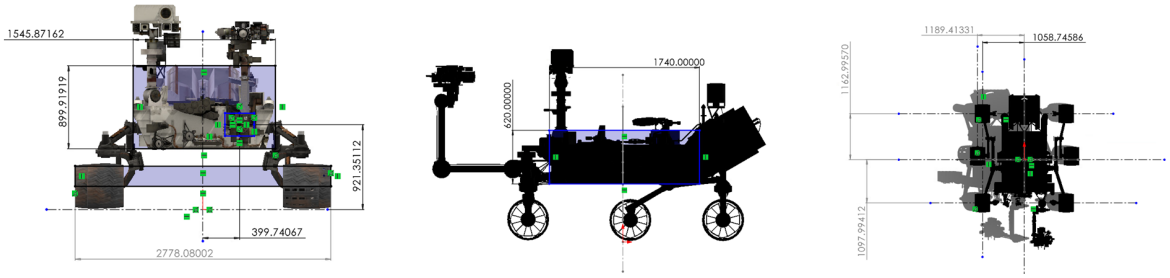

(a) Front profile measurements. (b) Side profile measurements. (c) Top view for contact points.

Figure 4.1: Data acquisition from the MSL CAD model using SolidWorks to parameterize the simplified mechanical model.

4.1.3 Step 3: Simulation and Comparison with Reference Data

The simplified mathematical model was implemented in MATLAB to simulate the rover's static response across a critical range of inclination angles ($40°, 45°$, and $50°$) for both X and Y axes.

Given the uncertainty regarding the exact internal mass distribution of the physical rover, an iterative estimation approach was adopted to define the CM of the simplified model. The CM coordinates were refined through successive simulation runs until the model's tipping point aligned precisely with the nominal $45°$ threshold established in the literature. This ensures that the simplified geometry effectively represents the global stability envelope of the actual vehicle.

4.1.3.1 X-Axis Stability Analysis

For the X-axis (longitudinal) tilt, the model demonstrated stability across all tested angles (Figure 4.2). Even at 50°, the rover remained stable. This higher stability margin in the X-axis is physically consistent with the rover's design, as the longitudinal wheel base is significantly larger than its lateral track width, resulting in a more elongated stability polygon.

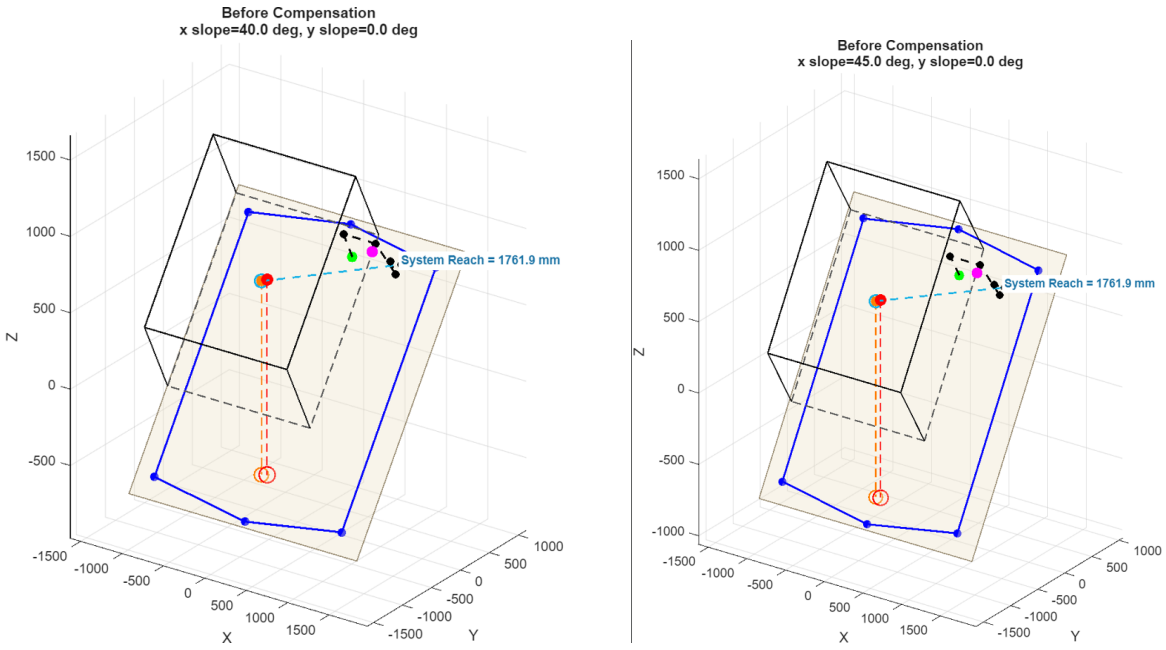

(a) X-axis tilt at 40°.

(b) X-axis tilt at 45°.

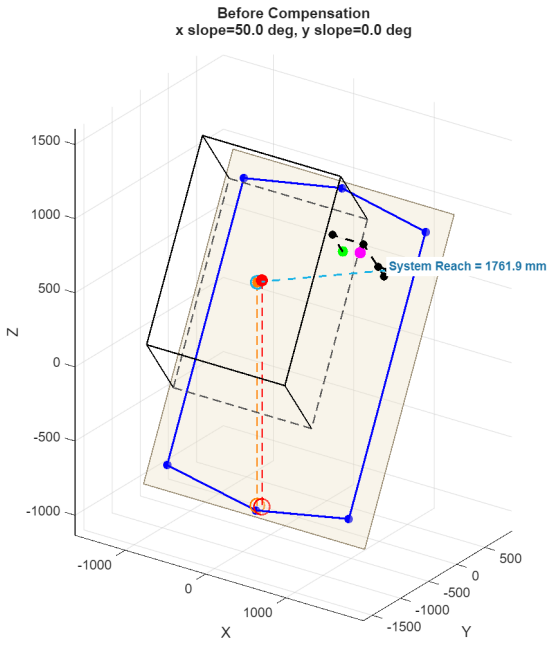

(c) X-axis tilt at 50°.

Figure 4.2: Static stability results for X-axis inclination.

4.1.3.2 Y-Axis Stability Analysis and Model Validation

The lateral stability analysis (Y-axis) provided the definitive validation of the model. As shown in Figure 4.3, the model is stable at 40° and reaches its limit at 45°, matching NASA's reported threshold. Crucially, at 50°, the system overturns as predicted, confirming the accuracy of the mathematical implementation. It is important to note that these results assume a rigid ground interface; in real Martian conditions, soil uncertainty and low-friction coefficients might lead to sliding before the geometric overturning limit is reached.

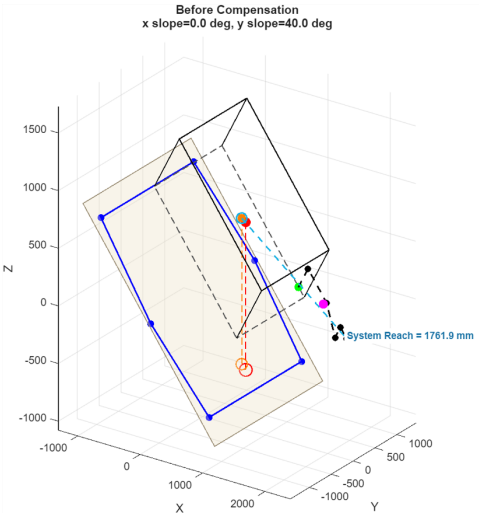

(a) Y-axis tilt at 40° (Stable).

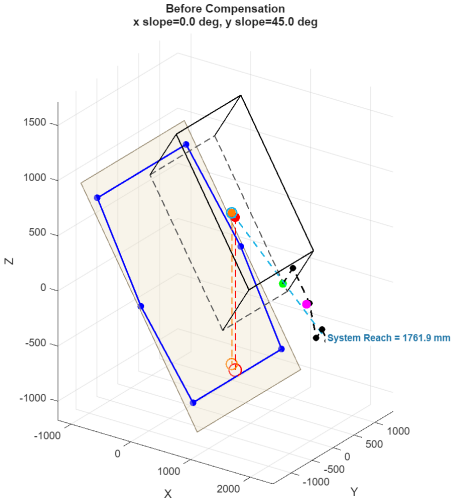

(b) Y-axis tilt at 45° (Threshold).

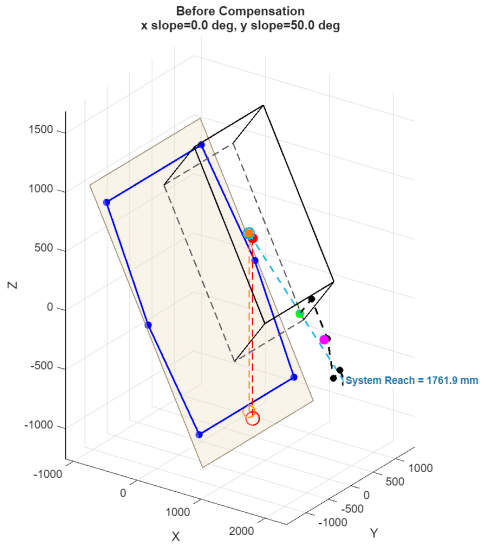

(c) Y-axis tilt at 50° (Overturning).

Figure 4.3: Static stability results for Y-axis inclination, validating the model against the 45° literature limit.

4.1.4 Assumptions and Simplifications

To maintain computational efficiency while ensuring physical relevance, the following assumptions were made:

- **Rigid Body Dynamics:** The rover components are treated as perfectly rigid, neglecting structural deformation or suspension compliance.
- **Ground Interaction:** The simulation assumes a non-deformable, high-friction surface to isolate the geometric stability limits from terramechanical variables.
- **Independence of Gravity Magnitude:** While Mars has a lower gravitational acceleration than Earth, the magnitude of g does not influence the *angle* of static overturning. This occurs because the tipping condition is determined strictly by the torque balance relative to the pivot point (the lowest wheel). Since both the restoring torque and the overturning torque are directly proportional to g ($\tau = \mathbf{r} \times m\mathbf{g}$), the gravity term cancels out when solving for the critical angle (θ), making the stability threshold purely a function of system geometry and mass distribution.
- **Independence of Environmental Factors:** The model assumes an isolated static environment, neglecting external aerodynamic forces such as wind or air friction. This simplification is justified by the low density of the Martian atmosphere (approximately 1% of Earth's) and the static nature of the simulation, where the magnitude of aerodynamic drag or lift is negligible compared to the gravitational forces acting on the 900 kg mass of the rover. Consequently, the stability limit is treated as a purely optomechanical and geometric problem.

Chapter 5

System Implementation and Technical Outputs

5.1 System Overview

The proposed framework is realised as an integrated evaluation system that enables large-scale analysis of rover–manipulator configurations under varying operating conditions. Rather than remaining at a conceptual level, the framework is implemented as a working system capable of generating, evaluating, and organising a large number of configuration instances in a consistent and reproducible manner.

The system combines configuration management, analytical computation, and data aggregation into a unified workflow. Structured parameter sets are used to define rover platforms, manipulator properties, and environmental conditions, which are systematically combined to construct the full configuration space. Each configuration is then evaluated using the analytical models defined in the methodology, producing quantitative measures of reachability and static stability.

To support efficient processing of the configuration space, the implementation separates configuration generation from analytical evaluation. A lightweight orchestration layer manages parameter combinations and dataset construction, while the analytical engine performs computation of system centre of mass, stability margin, and related metrics. The resulting outputs are stored in a structured dataset, enabling direct comparison and further analysis.

In addition to numerical evaluation, the system incorporates a simulation layer for visual inspection of representative configurations. This allows the behaviour of the rover–manipulator system to be observed in terms of centre-of-mass projection and support polygon interaction, providing an intuitive validation of the analytical results.

Overall, the implemented system transforms the proposed framework into a practical evaluation platform, capable of producing consistent, scalable, and interpretable outputs

Figure 5.1: Modular Parameter Database Structure for Configuration Management

for subsequent analysis.

5.2 Configuration and Dataset

The configuration space defined in the methodology is instantiated into a structured and scalable dataset through a modular parameter management approach. Instead of representing configurations implicitly, all system parameters are explicitly organised into dedicated data repositories, enabling systematic construction of configuration instances.

As shown in Figure 5.1, the implementation adopts a modular database structure in which different parameter domains are stored separately, including rover platforms, manipulator configurations, scaling parameters, posture definitions, and terrain conditions. This separation allows each parameter group to be defined, updated, and extended independently, while still supporting flexible combination across domains.

Each rover–manipulator system is encoded as a structured configuration entity, where geometric properties, mass distribution, support polygon definition, and mounting parameters are explicitly defined. An example of this structured representation is illustrated in Figure 5.2. This unified schema ensures that all configurations are described in a consistent format, forming a reliable basis for automated evaluation.

Based on these parameter definitions, the full configuration space is generated through systematic combination across all parameter domains. The resulting configurations are stored as a structured dataset, where each entry corresponds to a unique combination of rover, manipulator, posture, and terrain conditions. A representative subset of this dataset is shown in Figure 5.3, where each configuration is uniquely identified and associated with its corresponding parameter attributes.

arms × surf_path × rovers ×

1×1 struct with 20 fields

Field	Value	Size	Class
Rover_ID	"RV01"	1×1	string
Rover_Name	"Perseverance-inspired Six-Wheel Rover"	1×1	string
Mobility_Type	"Wheeled"	1×1	string
Rover_Mass	900	1×1	double
Rover_Length	1720	1×1	double
Rover_Width	1545	1×1	double
Rover_Height	620	1×1	double
Rover_Clearance	660	1×1	double
Centre_of_Mass_Position	[0,0,970]	1×3	double
Support_Point_Count	6	1×1	double
Support_Points	6×3 double	6×3	double
Active_Suspension_Enabled	0	1×1	logical
Chassis_active_Roll_Limit	[0,0]	1×2	double
Chassis_active_Pitch_Limit	[0,0]	1×2	double
Chassis_active_Longitudinal_Shift	[0,0]	1×2	double
Chassis_active_Lateral_Shift	[0,0]	1×2	double
Chassis_active_Height_Adjust	[0,0]	1×2	double
Mount_Front	[860,400,921]	1×3	double
Mount_Centre	[0,0,1280]	1×3	double
Mount_Side	[0,280,1280]	1×3	double

Figure 5.2: Structured Representation of a Rover Configuration Entity

Config_ID	Rover_ID	Arm_ID	Ratio_ID	Rover	Arm	Ratio	Mount_ID	Mount_Na	Mount_Po	Arm_Base	Posture_IC	Posture_N	Joint_Angl	Posture	Arm_Tota	Rover_Tot	Arm_CoM	Arm_CoM	System_Ci	Link_CoM	Link_CoM	Terrain_ID	Terrain_Ty	Terrain_X	Terrain_Y	Terrain	Origi
2	RV01_RS0	RV01_RS0	AM02_MS	MS01	{"Rover_IC":{"Arm_ID":	{"Ratio_ID":MF	Front	[191 90 85	[191 90 85	MP20	Home	[0.00 -90.(	{"Manipul	0.3	10	[-0.00 -	13	[191.90 7	[5.59 2.19	[0.00 0.00	[191.90 85	TR01	Flat	0	0	{"Terrain_I	[191
3	RV01_RS0	RV01_RS0	AM02_MS	MS01	{"Rover_IC":{"Arm_ID":	{"Ratio_ID":MF	Front	[191 90 85	[191 90 85	MP20	Home	[0.00 -90.(	{"Manipul	0.3	10	[-0.00 -	13	[191.90 7	[5.59 2.19	[0.00 0.00	[191.90 85	TR02	Longitudir	0	5	{"Terrain_I	[191
4	RV01_RS0	RV01_RS0	AM02_MS	MS01	{"Rover_IC":{"Arm_ID":	{"Ratio_ID":MF	Front	[191 90 85	[191 90 85	MP20	Home	[0.00 -90.(	{"Manipul	0.3	10	[-0.00 -	13	[191.90 7	[5.59 2.19	[0.00 0.00	[191.90 85	TR03	Longitudir	0	10	{"Terrain_I	[191
5	RV01_RS0	RV01_RS0	AM02_MS	MS01	{"Rover_IC":{"Arm_ID":	{"Ratio_ID":MF	Front	[191 90 85	[191 90 85	MP20	Home	[0.00 -90.(	{"Manipul	0.3	10	[-0.00 -	13	[191.90 7	[5.59 2.19	[0.00 0.00	[191.90 85	TR04	Longitudir	0	15	{"Terrain_I	[191
6	RV01_RS0	RV01_RS0	AM02_MS	MS01	{"Rover_IC":{"Arm_ID":	{"Ratio_ID":MF	Front	[191 90 85	[191 90 85	MP20	Home	[0.00 -90.(	{"Manipul	0.3	10	[-0.00 -	13	[191.90 7	[5.59 2.19	[0.00 0.00	[191.90 85	TR05	Lateral_Mi	5	0	{"Terrain_I	[191
7	RV01_RS0	RV01_RS0	AM02_MS	MS01	{"Rover_IC":{"Arm_ID":	{"Ratio_ID":MF	Front	[191 90 85	[191 90 85	MP20	Home	[0.00 -90.(	{"Manipul	0.3	10	[-0.00 -	13	[191.90 7	[5.59 2.19	[0.00 0.00	[191.90 85	TR06	Lateral_Mi	10	0	{"Terrain_I	[191
8	RV01_RS0	RV01_RS0	AM02_MS	MS01	{"Rover_IC":{"Arm_ID":	{"Ratio_ID":MF	Front	[191 90 85	[191 90 85	MP20	Home	[0.00 -90.(	{"Manipul	0.3	10	[-0.00 -	13	[191.90 7	[5.59 2.19	[0.00 0.00	[191.90 85	TR07	Lateral_Sh	15	0	{"Terrain_I	[191
9	RV01_RS0	RV01_RS0	AM02_MS	MS01	{"Rover_IC":{"Arm_ID":	{"Ratio_ID":MF	Front	[191 90 85	[191 90 85	MP20	Home	[0.00 -90.(	{"Manipul	0.3	10	[-0.00 -	13	[191.90 7	[5.59 2.19	[0.00 0.00	[191.90 85	TR08	Combinec	5	5	{"Terrain_I	[191
10	RV01_RS0	RV01_RS0	AM02_MS	MS01	{"Rover_IC":{"Arm_ID":	{"Ratio_ID":MF	Front	[191 90 85	[191 90 85	MP20	Home	[0.00 -90.(	{"Manipul	0.3	10	[-0.00 -	13	[191.90 7	[5.59 2.19	[0.00 0.00	[191.90 85	TR09	Combinec	10	10	{"Terrain_I	[191
11	RV01_RS0	RV01_RS0	AM02_MS	MS01	{"Rover_IC":{"Arm_ID":	{"Ratio_ID":MF	Front	[191 90 85	[191 90 85	MP20	Home	[0.00 -90.(	{"Manipul	0.3	10	[-0.00 -	13	[191.90 7	[5.59 2.19	[0.00 0.00	[191.90 85	TR10	Combinec	15	15	{"Terrain_I	[191
12	RV01_RS0	RV01_RS0	AM02_MS	MS01	{"Rover_IC":{"Arm_ID":	{"Ratio_ID":MF	Front	[191 90 85	[191 90 85	MP20	Home	[0.00 -90.(	{"Manipul	0.3	10	[-0.00 -	13	[191.90 7	[5.59 2.19	[0.00 0.00	[191.90 85	TR11	Diag_Long	6	12	{"Terrain_I	[191
13	RV01_RS0	RV01_RS0	AM02_MS	MS01	{"Rover_IC":{"Arm_ID":	{"Ratio_ID":MF	Front	[191 90 85	[191 90 85	MP20	Home	[0.00 -90.(	{"Manipul	0.3	10	[-0.00 -	13	[191.90 7	[5.59 2.19	[0.00 0.00	[191.90 85	TR12	Diag_Lat_I	12	6	{"Terrain_I	[191
14	RV01_RS0	RV01_RS0	AM02_MS	MS01	{"Rover_IC":{"Arm_ID":	{"Ratio_ID":MF	Front	[191 90 85	[191 90 85	MP20	Home	[0.00 -90.(	{"Manipul	0.3	10	[-0.00 -	13	[191.90 7	[5.59 2.19	[0.00 0.00	[191.90 85	TR13	Longitudir	0	25	{"Terrain_I	[191
15	RV01_RS0	RV01_RS0	AM02_MS	MS01	{"Rover_IC":{"Arm_ID":	{"Ratio_ID":MF	Front	[191 90 85	[191 90 85	MP20	Home	[0.00 -90.(	{"Manipul	0.3	10	[-0.00 -	13	[191.90 7	[5.59 2.19	[0.00 0.00	[191.90 85	TR14	Combinec	25	25	{"Terrain_I	[191
16	RV01_RS0	RV01_RS0	AM02_MS	MS01	{"Rover_IC":{"Arm_ID":	{"Ratio_ID":MF	Front	[191 90 85	[191 90 85	MP20	Home	[0.00 -90.(	{"Manipul	0.3	10	[-0.00 -	13	[191.90 7	[5.59 2.19	[0.00 0.00	[191.90 85	TR15	Diag_Long	15	25	{"Terrain_I	[191
17	RV01_RS0	RV01_RS0	AM02_MS	MS01	{"Rover_IC":{"Arm_ID":	{"Ratio_ID":MF	Front	[191 90 85	[191 90 85	MP21	Stowed	[0.00 -90.(	{"Manipul	0.3	10	[25.29 -	12	[217.19 7	[6.33 2.24	[0.00 0.00	[191.90 85	TR01	Flat	0	0	{"Terrain_I	[191
18	RV01_RS0	RV01_RS0	AM02_MS	MS01	{"Rover_IC":{"Arm_ID":	{"Ratio_ID":MF	Front	[191 90 85	[191 90 85	MP21	Stowed	[0.00 -90.(	{"Manipul	0.3	10	[25.29 -	12	[217.19 7	[6.33 2.24	[0.00 0.00	[191.90 85	TR02	Longitudir	0	5	{"Terrain_I	[191
19	RV01_RS0	RV01_RS0	AM02_MS	MS01	{"Rover_IC":{"Arm_ID":	{"Ratio_ID":MF	Front	[191 90 85	[191 90 85	MP21	Stowed	[0.00 -90.(	{"Manipul	0.3	10	[25.29 -	12	[217.19 7	[6.33 2.24	[0.00 0.00	[191.90 85	TR03	Longitudir	0	10	{"Terrain_I	[191
20	RV01_RS0	RV01_RS0	AM02_MS	MS01	{"Rover_IC":{"Arm_ID":	{"Ratio_ID":MF	Front	[191 90 85	[191 90 85	MP21	Stowed	[0.00 -90.(	{"Manipul	0.3	10	[25.29 -	12	[217.19 7	[6.33 2.24	[0.00 0.00	[191.90 85	TR04	Longitudir	0	15	{"Terrain_I	[191
21	RV01_RS0	RV01_RS0	AM02_MS	MS01	{"Rover_IC":{"Arm_ID":	{"Ratio_ID":MF	Front	[191 90 85	[191 90 85	MP21	Stowed	[0.00 -90.(	{"Manipul	0.3	10	[25.29 -	12	[217.19 7	[6.33 2.24	[0.00 0.00	[191.90 85	TR05	Lateral_Mi	5	0	{"Terrain_I	[191
22	RV01_RS0	RV01_RS0	AM02_MS	MS01	{"Rover_IC":{"Arm_ID":	{"Ratio_ID":MF	Front	[191 90 85	[191 90 85	MP21	Stowed	[0.00 -90.(	{"Manipul	0.3	10	[25.29 -	12	[217.19 7	[6.33 2.24	[0.00 0.00	[191.90 85	TR06	Lateral_Mi	10	0	{"Terrain_I	[191
23	RV01_RS0	RV01_RS0	AM02_MS	MS01	{"Rover_IC":{"Arm_ID":	{"Ratio_ID":MF	Front	[191 90 85	[191 90 85	MP21	Stowed	[0.00 -90.(	{"Manipul	0.3	10	[25.29 -	12	[217.19 7	[6.33 2.24	[0.00 0.00	[191.90 85	TR07	Lateral_Sh	15	0	{"Terrain_I	[191
24	RV01_RS0	RV01_RS0	AM02_MS	MS01	{"Rover_IC":{"Arm_ID":	{"Ratio_ID":MF	Front	[191 90 85	[191 90 85	MP21	Stowed	[0.00 -90.(	{"Manipul	0.3	10	[25.29 -	12	[217.19 7	[6.33 2.24	[0.00 0.00	[191.90 85	TR08	Combinec	5	5	{"Terrain_I	[191
25	RV01_RS0	RV01_RS0	AM02_MS	MS01	{"Rover_IC":{"Arm_ID":	{"Ratio_ID":MF	Front	[191 90 85	[191 90 85	MP21	Stowed	[0.00 -90.(	{"Manipul	0.3	10	[25.29 -	12	[217.19 7	[6.33 2.24	[0.00 0.00	[191.90 85	TR09	Combinec	10	10	{"Terrain_I	[191
26	RV01_RS0	RV01_RS0	AM02_MS	MS01	{"Rover_IC":{"Arm_ID":	{"Ratio_ID":MF	Front	[191 90 85	[191 90 85	MP21	Stowed	[0.00 -90.(	{"Manipul	0.3	10	[25.29 -	12	[217.19 7	[6.33 2.24	[0.00 0.00	[191.90 85	TR10	Combinec	15	15	{"Terrain_I	[191
27	RV01_RS0	RV01_RS0	AM02_MS	MS01	{"Rover_IC":{"Arm_ID":	{"Ratio_ID":MF	Front	[191 90 85	[191 90 85	MP21	Stowed	[0.00 -90.(	{"Manipul	0.3	10	[25.29 -	12	[217.19 7	[6.33 2.24	[0.00 0.00	[191.90 85	TR11	Diag_Long	6	12	{"Terrain_I	[191
28	RV01_RS0	RV01_RS0	AM02_MS	MS01	{"Rover_IC":{"Arm_ID":	{"Ratio_ID":MF	Front	[191 90 85	[191 90 85	MP21	Stowed	[0.00 -90.(	{"Manipul	0.3	10	[25.29 -	12	[217.19 7	[6.33 2.24	[0.00 0.00	[191.90 85	TR12	Diag_Lat_I	12	6	{"Terrain_I	[191
29	RV01_RS0	RV01_RS0	AM02_MS	MS01	{"Rover_IC":{"Arm_ID":	{"Ratio_ID":MF	Front	[191 90 85	[191 90 85	MP21	Stowed	[0.00 -90.(	{"Manipul	0.3	10	[25.29 -	12	[217.19 7	[6.33 2.24	[0.00 0.00	[191.90 85	TR13	Longitudir	0	25	{"Terrain_I	[191
30	RV01_RS0	RV01_RS0	AM02_MS	MS01	{"Rover_IC":{"Arm_ID":	{"Ratio_ID":MF	Front	[191 90 85	[191 90 85	MP21	Stowed	[0.00 -90.(	{"Manipul	0.3	10	[25.29 -	12	[217.19 7	[6.33 2.24	[0.00 0.00	[191.90 85	TR14	Combinec	25	25	{"Terrain_I	[191
31	RV01_RS0	RV01_RS0	AM02_MS	MS01	{"Rover_IC":{"Arm_ID":	{"Ratio_ID":MF	Front	[191 90 85	[191 90 85	MP21	Stowed	[0.00 -90.(	{"Manipul	0.3	10	[25.29 -	12	[217.19 7	[6.33 2.24	[0.00 0.00	[191.90 85	TR15	Diag_Long	15	25	{"Terrain_I	[191
32	RV01_RS0	RV01_RS0	AM02_MS	MS01	{"Rover_IC":{"Arm_ID":	{"Ratio_ID":MF	Front	[191 90 85	[191 90 85	MP22	Mid-reac	[0.00 - 12(	{"Manipul	0.3	10	[47.53 -	12	[239.43 7	[6.98 2.24	[0.00 0.00	[191.90 85	TR01	Flat	0	0	{"Terrain_I	[191
33	RV01_RS0	RV01_RS0	AM02_MS	MS01	{"Rover_IC":{"Arm_ID":	{"Ratio_ID":MF	Front	[191 90 85	[191 90 85	MP22	Mid-reac	[0.00 - 12(	{"Manipul	0.3	10	[47.53 -	12	[239.43 7	[6.98 2.24	[0.00 0.00	[191.90 85	TR02	Longitudir	0	5	{"Terrain_I	[191
34	RV01_RS0	RV01_RS0	AM02_MS	MS01	{"Rover_IC":{"Arm_ID":	{"Ratio_ID":MF	Front	[191 90 85	[191 90 85	MP22	Mid-reac	[0.00 - 12(	{"Manipul	0.3	10	[47.53 -	12	[239.43 7	[6.98 2.24	[0.00 0.00	[191.90 85	TR03	Longitudir	0	10	{"Terrain_I	[191
35	RV01_RS0	RV01_RS0	AM02_MS	MS01	{"Rover_IC":{"Arm_ID":	{"Ratio_ID":MF	Front	[191 90 85	[191 90 85	MP22	Mid-reac	[0.00 - 12(	{"Manipul	0.3	10	[47.53 -	12	[239.43 7	[6.98 2.24	[0.00 0.00	[191.90 85	TR04	Longitudir	0	15	{"Terrain_I	[191
36	RV01_RS0	RV01_RS0	AM02_MS	MS01	{"Rover_IC":{"Arm_ID":	{"Ratio_ID":MF	Front	[191 90 85	[191 90 85	MP22	Mid-reac	[0.00 - 12(	{"Manipul	0.3	10	[47.53 -	12	[239.43 7	[6.98 2.24	[0.00 0.00	[191.90 85	TR05	Lateral_Mi	5	0	{"Terrain_I	[191
37	RV01_RS0	RV01_RS0	AM02_MS	MS01	{"Rover_IC":{"Arm_ID":	{"Ratio_ID":MF	Front	[191 90 85	[191 90 85	MP22	Mid-reac	[0.00 - 12(	{"Manipul	0.3	10	[47.53 -	12	[239.43 7	[6.98 2.24	[0.00 0.00	[191.90 85	TR06	Lateral_Mi	10	0	{"Terrain_I	[191
38	RV01_RS0	RV01_RS0	AM02_MS	MS01	{"Rover_IC":{"Arm_ID":	{"Ratio_ID":MF	Front	[191 90 85	[191 90 85	MP22	Mid-reac	[0.00 - 12(	{"Manipul	0.3	10	[47.53 -	12	[239.43 7	[6.98 2.24	[0.00 0.00	[191.90 85	TR07	Lateral_Sh	15	0	{"Terrain_I	[191

rover_arm_posture_terrain_confi

Figure 5.3: Generated Configuration Dataset with Combined Parameter Instances

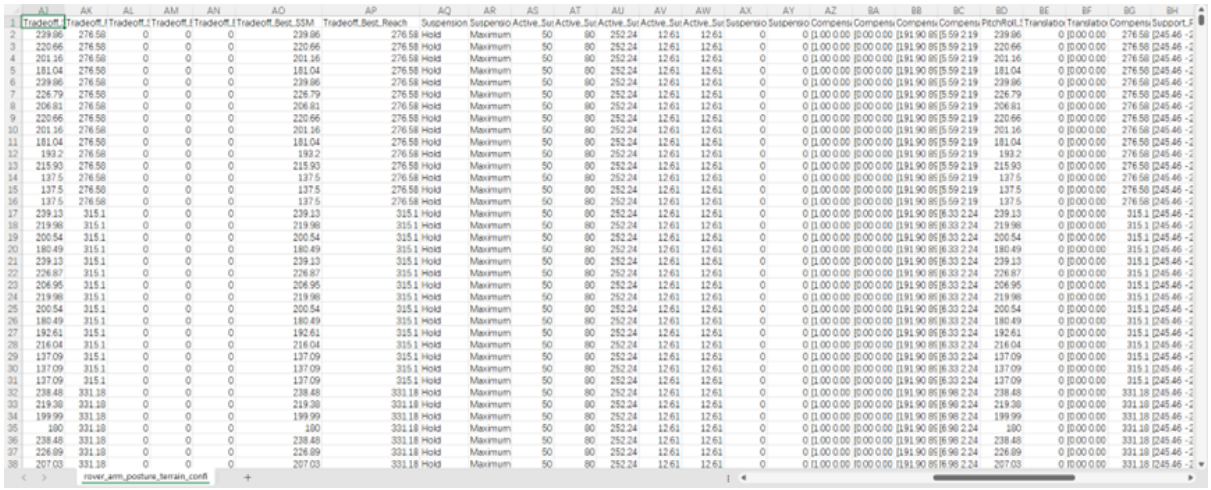

Figure 5.4: Structured Evaluation Dataset Integrating Configuration Parameters and Performance Metrics

5.3 Analytical Outputs

The constructed configuration dataset is processed to generate quantitative evaluation outputs describing system reachability and static stability. For each configuration instance, the analytical model produces a set of metrics that characterise the system performance under the corresponding parameter combination. The primary evaluation results are organised into a unified dataset, where each entry integrates both configuration parameters and computed outputs. As illustrated in Figure 5.4, each configuration is uniquely identified and associated with its corresponding rover, manipulator, posture, and terrain attributes, together with the evaluated performance metrics. This unified representation enables direct comparison across configurations within a consistent data structure.

Due to the large scale of the configuration space, the complete dataset contains a substantial number of entries. Therefore, representative subsets are used for visual inspection, while the full dataset is retained for systematic analysis. This approach ensures both scalability of computation and clarity of presentation.

In addition to the primary outputs, further aggregation is performed to support higher-level comparison across different system architectures. An example of such aggregated results is shown in Figure 5.5, where key indicators are summarised to provide an overview of system performance under different configurations.

5.4 Simulation Demonstration

To support practical usage and inspection of the evaluation results, a lightweight interface is developed for configuration management and data access. As shown in Figure 5.6, the system provides a structured view of configuration parameters and evaluation

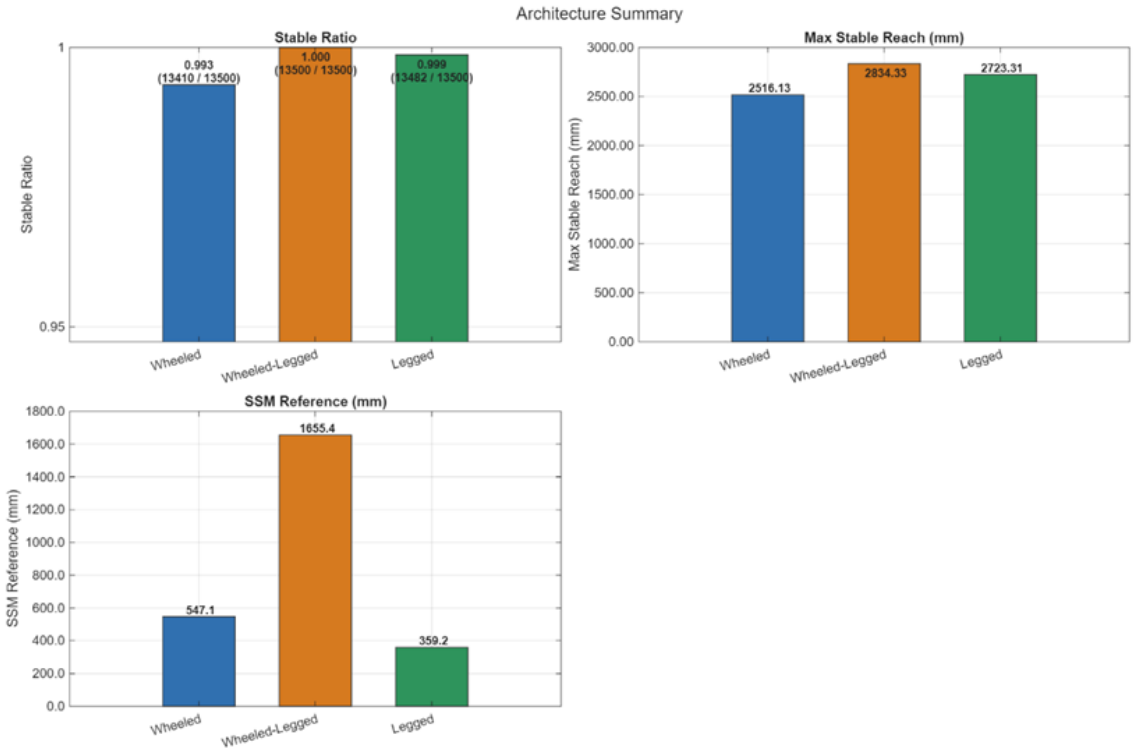

Figure 5.5: Aggregated Performance Comparison Across Rover Architectures

outputs, allowing efficient exploration of the generated dataset.

This interface enables users to inspect configuration definitions, access evaluation results, and navigate across different parameter combinations. It serves as a practical layer connecting the analytical computation with user-level interaction, facilitating interpretation of the generated data. In addition to the interface-based inspection, a simulation environment is used to provide visual representation of representative configurations. As illustrated in Figure 5.7, the rover–manipulator system is visualised in a three-dimensional space, where the centre of mass and support polygon are explicitly represented.

Through this visualisation, the stability condition of the system can be directly observed. The relative position of the projected centre of mass with respect to the support polygon provides an intuitive interpretation of the analytical stability metrics. This complements the numerical evaluation and enhances understanding of the reachability–stability relationship. While the interface enables structured access to the dataset, and the simulation provides visual validation, the primary evaluation results remain based on the analytical model described in the methodology. Additional simulation results under a wider range of configurations and terrain conditions are provided in Appendix A for completeness.

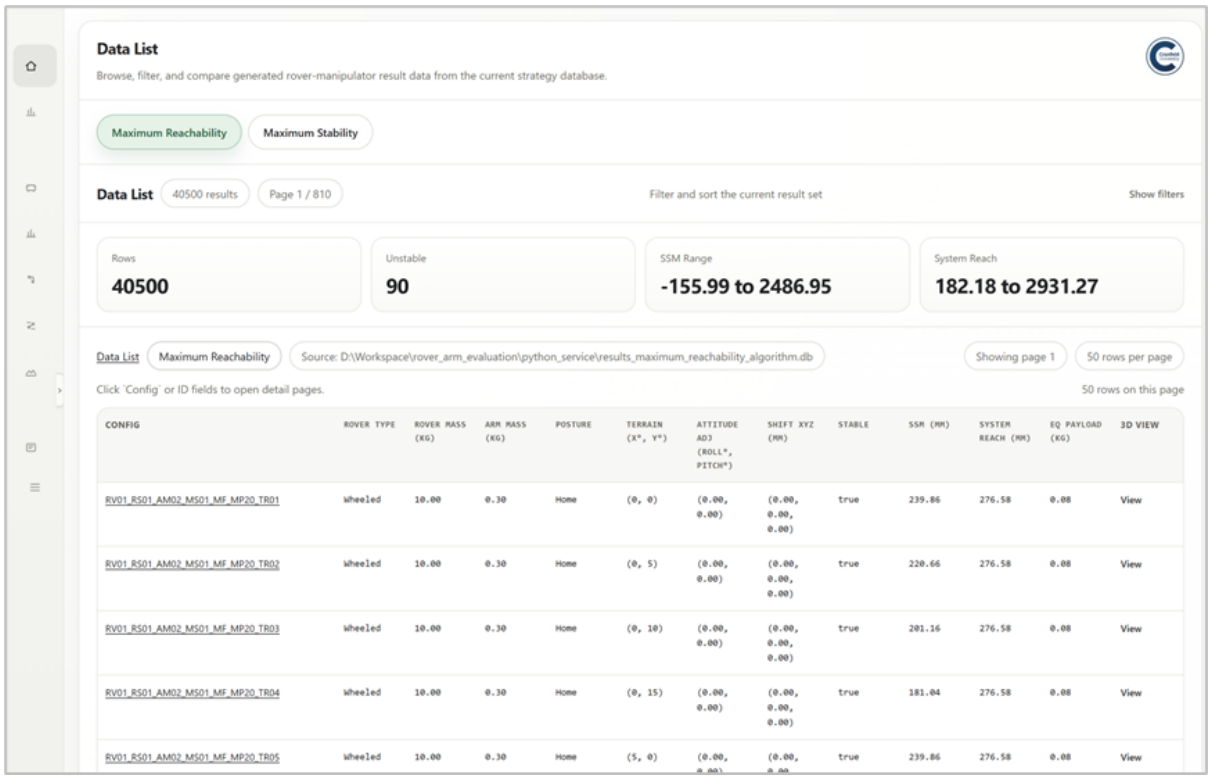

Figure 5.6: User Interface for Configuration Exploration and Evaluation Result Inspection

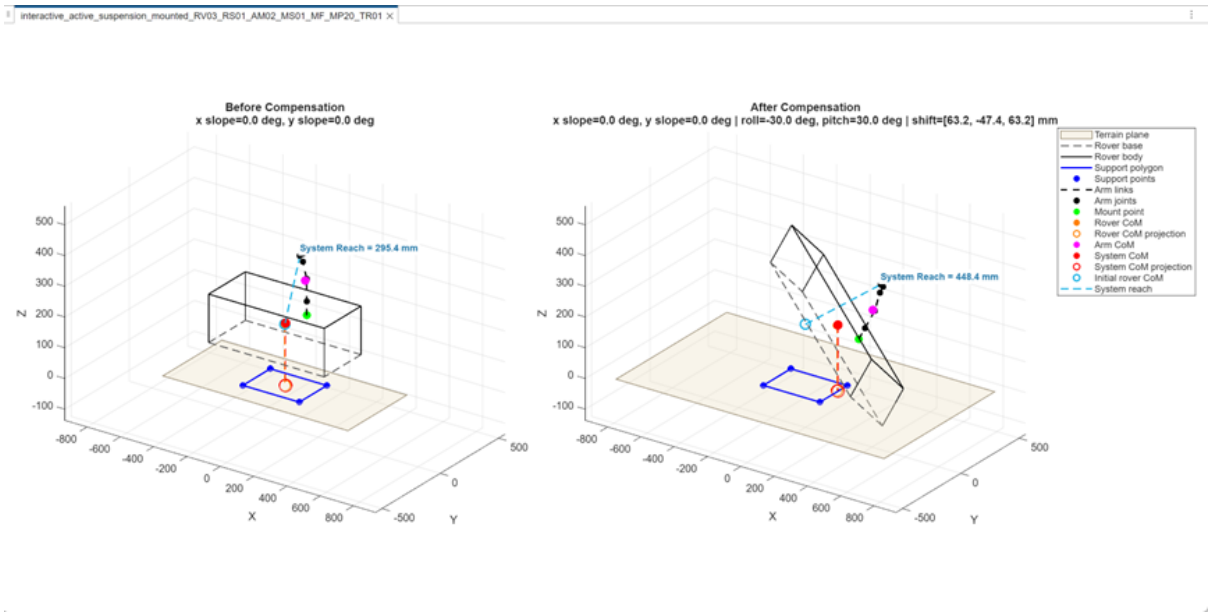

Figure 5.7: Visualisation of Rover–Manipulator System Showing Centre of Mass and Support Polygon

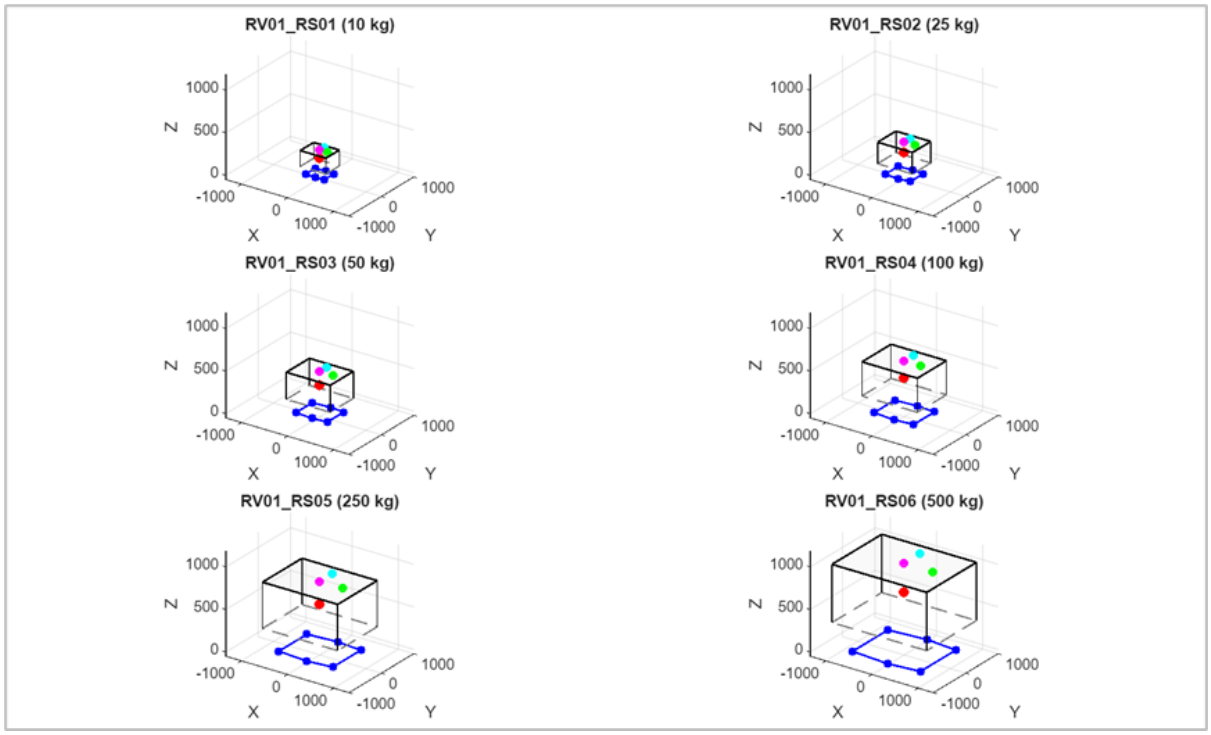

Figure 5.8: Rover geometric scaling across different mass levels

5.5 Verification and Validation

5.5.1 Configuration and Scaling Consistency Verification

The configuration generation process was verified to ensure that the applied scaling rules and parameter fusion mechanisms produce physically consistent and structurally valid system configurations. This verification is essential, as the reliability of subsequent analytical evaluation depends directly on the correctness of the generated configuration dataset.

The rover geometric scaling was first examined against the predefined mass–geometry relationship. In the proposed framework, rover dimensions are scaled proportionally according to a cubic-root formulation, ensuring consistency with volumetric scaling assumptions. The resulting configurations exhibit a monotonic increase in rover length and width with increasing rover mass, confirming that the geometric scaling behaviour follows the intended physical model.

As illustrated in Figure 5.8, representative rover configurations across different mass levels demonstrate consistent geometric expansion while preserving structural proportions, supporting that the implemented scaling mechanism adheres to the intended volumetric scaling relationship.

In parallel, the scaling of manipulator properties was validated with respect to the rover mass. The arm mass is defined as a ratio of rover mass, and corresponding geometric

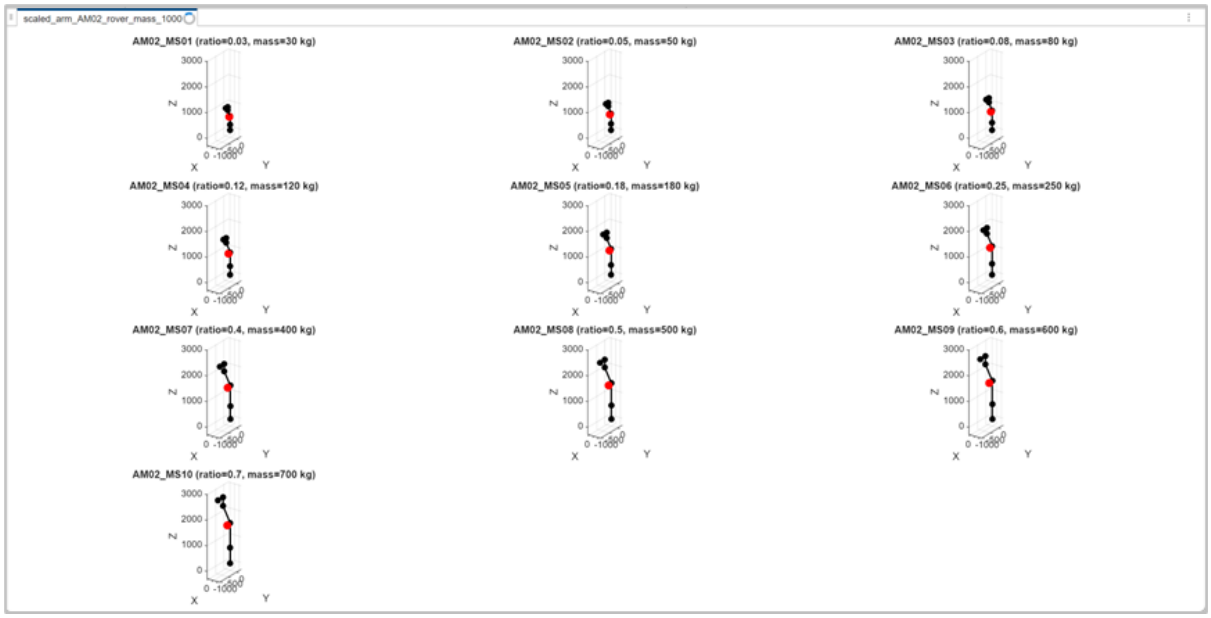

Figure 5.9: Manipulator scaling validation across mass ratios (referenced to 1000 kg rover), showing proportional geometry scaling and coherent CoM evolution

parameters are scaled consistently. The generated configurations demonstrate coherent relationships between rover mass, arm mass, and maximum reach, indicating that the scaling rules are applied uniformly across system components.

As illustrated in Figure 5.9, each configuration reflects the defined mass ratio and corresponding absolute arm mass, confirming the correctness of the ratio-to-mass mapping. The manipulator geometry scales proportionally across all cases, with no structural distortion, while the centre-of-mass (CoM) position evolves consistently with increasing arm size, preserving its relative location.

The parameter fusion process, which integrates rover configurations, manipulator properties, mounting positions, postures, and terrain conditions into a unified configuration space, was also examined. All generated configurations preserve valid geometric relationships and consistent mappings between system components. No conflicting parameter combinations or structurally invalid configurations were observed, indicating that the fusion process produces coherent system definitions. To further assess consistency at the dataset level, statistical validation was performed on the derived parameters.

As illustrated in Figure 5.10, clear monotonic relationships are observed between rover mass and key derived quantities, including rover dimensions, arm mass, and arm reach. These trends confirm that the configuration generation process produces physically meaningful and internally consistent data distributions, rather than arbitrary parameter combinations.

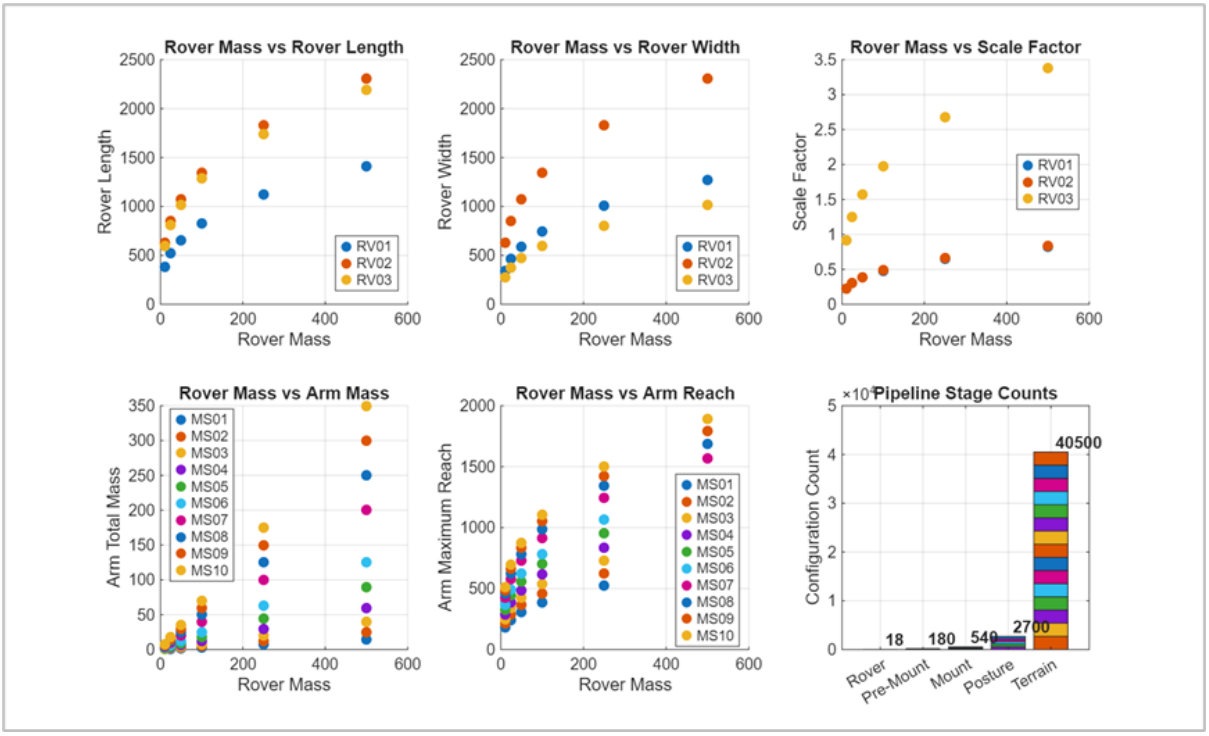

Figure 5.10: Consistency of scaling relationships across rover and manipulator configurations. The figure illustrates monotonic trends between rover mass and derived parameters, including rover dimensions, arm mass, and maximum reach, confirming the physical coherence of the scaling and parameter fusion process

5.5.2 Analytical Model Verification

To verify the correctness of the analytical computation framework, a representative configuration case was selected, and its full calculation chain was manually validated using the exported intermediate data. The verification aims to ensure that all key outputs—particularly centre-of-mass propagation, terrain projection, stability margin, and reachability—are numerically consistent with the underlying analytical formulations.

The input parameters for the selected configuration are summarised in Table X. These parameters define the system mass distribution, geometric configuration, terrain condition, and reference quantities required for subsequent calculations.

Based on these inputs, the key computational steps were independently evaluated and compared against the exported results, as summarised in Table Y.

article amsmath amssymb

The verification confirms that each stage of the analytical model produces results consistent with the corresponding theoretical formulations. In particular, the system centre-of-mass is correctly propagated from component-level properties, and its projection onto the inclined terrain is consistent with the gravity-direction transformation under combined slope conditions. The resulting projected CoM location leads to a stability margin that matches the geometric definition based on the support polygon.

Table 5.1: Input Parameters for Verification Case

Category	Parameter	Value
Rover	Mass	10.00 kg
	CoM (Rover Frame)	(0.00, 0.00, 216.45) mm
Arm	Total Mass	0.30 kg
	Arm CoM (Rover Frame)	(191.90, 75.27, 321.91) mm
Terrain	X slope	15°
	Y slope	15°
Geometry	Support Polygon (2D)	[(245.46, -236.53), ..., (0, -265.54)]
Flange	Position (Arm Frame)	(0.00, -58.05, 207.65) mm
	Position (Rover Frame)	(191.90, 31.21, 413.16) mm
Constants	Gravity	1.62 m/s^2
	Equivalent Height	0.41 m

Table 5.2: Calculation Verification Results

Step	Calculation Item	Formula	Result	Match
1	System Mass	$M_{sys} = M_r + M_a$	10.30 kg	✓
2	System CoM	mass-weighted average	(5.59, 2.19, 219.52)	✓
3	Terrain Projection	gravity-direction projection	(64.42, -58.70)	✓
4	Stability Margin (SSM)	min distance to polygon edge	181.04 mm	✓
5	Arm Reach	Euclidean norm	215.61 mm	✓
6	System Reach	Euclidean norm	276.58 mm	✓
7	Restoring Moment	$M = Mgd$	3.02 Nm	✓
8	Equivalent Payload	derived from moment	4.51 kg → 0.08 kg	✓

Furthermore, the reachability metrics derived from flange positions are consistent with Euclidean distance formulations, and the restoring moment calculation aligns with the quasi-static stability model. The equivalent payload estimation is also consistent with the derived force and the manipulator payload constraint.

Minor numerical differences (within rounding precision) may arise due to floating-point operations in intermediate steps; however, all results remain consistent within acceptable tolerance.

This verification focuses on a representative configuration, while the same computational procedure is consistently applied across the full dataset. Therefore, the agreement between independently evaluated results and exported data demonstrates that the analytical model is correctly implemented and numerically consistent across the complete computation chain.

5.5.3 System-Level Behaviour Validation

System-level validation was conducted to assess whether the proposed framework produces physically consistent and meaningful behaviour across the entire configuration space. Unlike the previous section, which focuses on numerical correctness of individual computations, this stage evaluates whether the aggregated results reflect expected physical relationships between reachability, stability, and system parameters.

Global Trend Consistency

The overall trends of the generated dataset were first examined. A clear and consistent trade-off between reachability and static stability is observed, where increased system reach is generally associated with a reduction in stability margin (SSM).

In addition, systematic degradation of stability is observed with increasing manipulator mass ratio and terrain inclination. These trends are consistent with physical intuition: a heavier manipulator shifts the system centre of mass away from the support region, while steeper terrain increases the likelihood of tipping by effectively reducing the stability margin.

Importantly, these relationships are not isolated observations but are consistently reproduced across different rover architectures, mounting configurations, and posture conditions, indicating that the framework captures the underlying physical dependencies rather than dataset-specific artefacts.

Active Suspension Strategy Validation

The behaviour of the active suspension strategies was evaluated by comparing their responses under identical initial configurations and posture conditions. Representative examples are shown in Figure 5.12.

For the same initial state, the two strategies produce noticeably different adjusted configurations. The stability-first strategy results in a more conservative posture, with

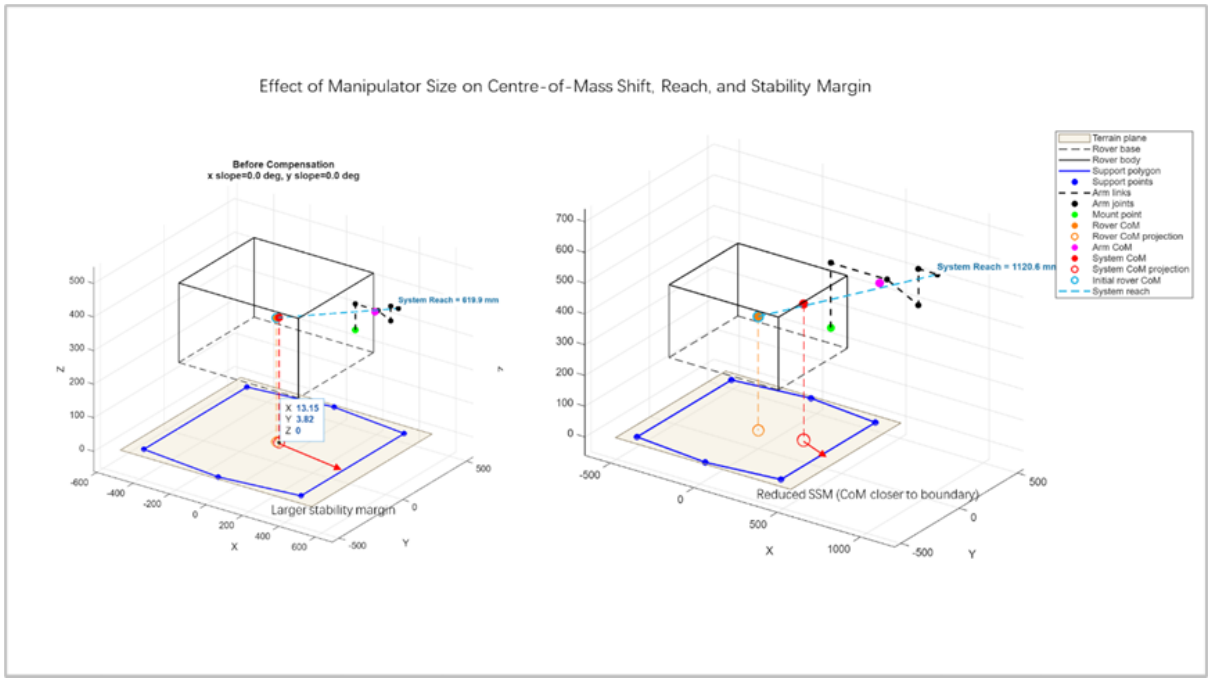

Figure 5.11: Effect of manipulator size on system behaviour. Increasing manipulator size shifts the system centre of mass (CoM) forward, resulting in increased reach and reduced stability margin (SSM). The CoM projection moves closer to the support polygon boundary, indicating a higher risk of tipping

the system centre of mass remaining well within the support region. In contrast, the reach-biased strategy leads to a more extended configuration, where the end-effector reach is increased and the centre of mass shifts closer to the support boundary.

These differences are directly reflected in the resulting system reach and stability margin. The reach-biased strategy achieves a larger reach at the cost of reduced stability margin, while the stability-first strategy maintains a larger stability buffer with limited reach extension.

The consistent divergence in resulting configurations confirms that the two strategies operate according to their intended objectives. This provides evidence that the active suspension adjustment mechanism produces distinct and interpretable behaviours suitable for comparative evaluation.

Cross-Configuration Consistency

Cross-configuration consistency was assessed by examining whether the same underlying geometric mechanism is preserved across heterogeneous configurations. Figure X presents representative cases under increasing terrain disturbance as an intuitive illustration. Although the figure focuses on terrain variation, the key observation is that stability changes are governed consistently by the relative position between the projected centre of mass (CoM) and the support polygon. As disturbance increases, the projected CoM moves towards the support boundary in a physically interpretable manner, without anomalous jumps or contradictory behaviour. Since other configuration variables, including

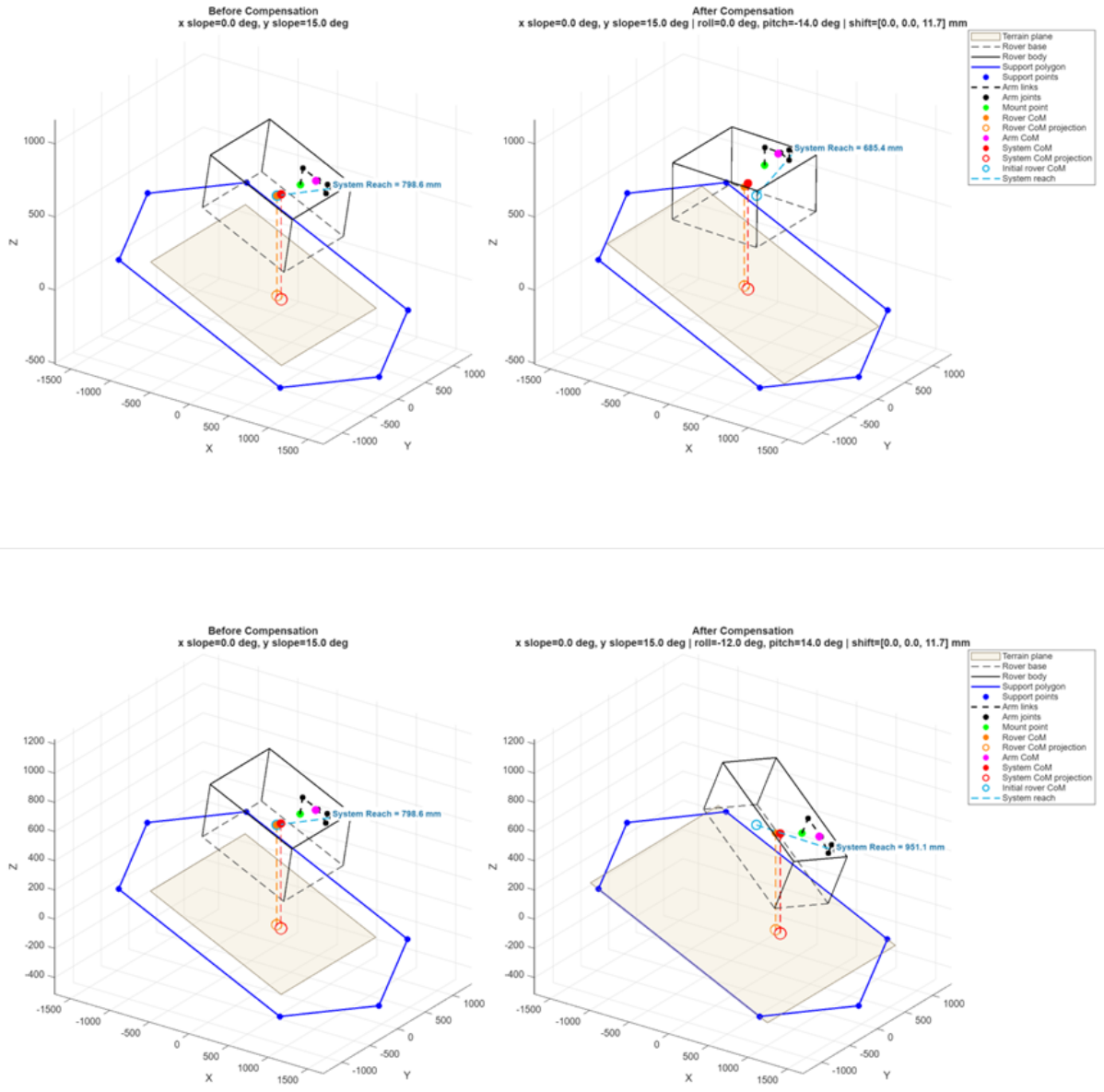

Figure 5.12: Comparison of two active suspension strategies under identical initial configuration. The stability-first strategy results in a conservative posture with higher stability margin, while the reach-biased strategy produces an extended configuration with increased reach and reduced stability margin

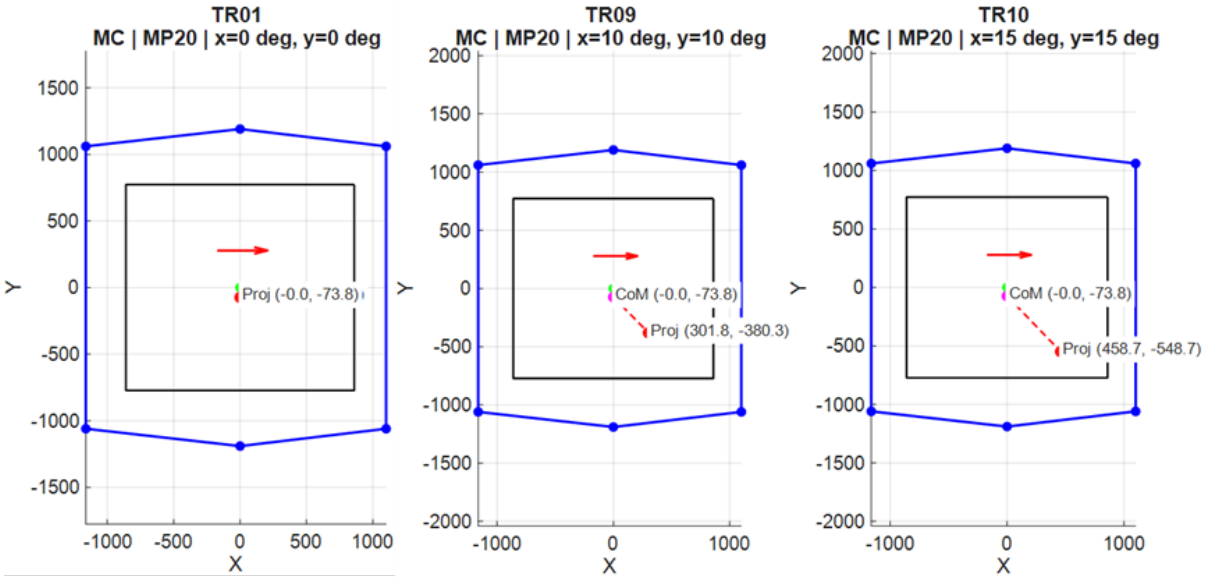

Figure 5.13: Illustration of cross-configuration consistency under progressively increasing terrain inclination. The projected centre of mass (CoM) shifts smoothly towards the downhill direction while the support polygon remains unchanged, demonstrating geometrically consistent and physically interpretable stability behaviour without anomalous patterns

manipulator posture, mounting position, and rover architecture, affect stability through the same CoM–support polygon relationship, this representative behaviour provides evidence that the framework maintains internal consistency across the wider configuration space rather than only for a single terrain sequence.

Summary of System-Level Validation

Overall, the observed global trends, boundary behaviours, and cross-configuration consistency confirm that the proposed framework produces realistic and physically interpretable system-level responses.

This provides additional confidence that the evaluation results are not only numerically correct (as verified in Section 5.5.2), but also physically meaningful when interpreted at the system level.

5.5.4 Platform Functional Validation

A staged functional validation was conducted to assess the reliability and usability of the developed evaluation platform. The validation scope covered core interaction mechanisms, including configuration editing, query execution, system response behaviour, and data consistency across key modules.

Representative user interaction workflows were tested across multiple modules. Typical operations, such as parameter editing, form submission, and multi-mode querying, were examined to verify the correctness of system responses and data handling.

The results indicate that the platform exhibits stable and consistent behaviour, with

correct data persistence, predictable query responses, and a unified interaction pattern across different functional pages. No critical inconsistencies or functional failures were identified during the testing process.

Detailed testing procedures and results are provided in Appendix B.

5.5.5 Scenario-Based Validation

Chapter 6

Results and Discussion

6.1 Architecture-Level Performance Comparison

6.2 Disturbance Sensitivity Analysis

6.3 Reachability–Stability Trade-off Analysis

Chapter 7

Conclusion

7.1 xxxxx

References

[1] National Aeronautics and Space Administration (NASA). Artemis; 2026. Accessed: 9 March 2026. https://www.nasa.gov/humans-in-space/artemis/.

[2] Squyres SW, Arvidson RE, Bell JF, Brückner J, Cabrol NA, Calvin W, et al. The Opportunity Rover's Athena Science Investigation at Meridiani Planum, Mars. Science. 2004;306(5702):1698-703.

[3] Grotzinger JP, Crisp J, Vasavada AR, Anderson RC, Baker CJ, Barry R, et al. Mars Science Laboratory Mission and Science Investigation. Space Science Reviews. 2012;170(1):5-56.

[4] Storiale F, Ferrentino E, Salvioli F, Kapellos K, Chiacchio P. Optimal Whole Body Trajectory Planning for Mobile Manipulators in Planetary Exploration and Construction. IEEE Open Journal of the Industrial Electronics Society. 2025;6:1285-97.

[5] NASA. Mars; 2023. Accessed: 9 March 2026. Available from: https://science.nasa.gov/mars/.

[6] Dzedzickis A, Subačiūtė-Žemaitienė J, Šutinys E, Samukaitė-Bubnienė U, Bučinskas V. Advanced Applications of Industrial Robotics: New Trends and Possibilities. Applied Sciences. 2022;12(1):135.

[7] Almurib HAF, Al-Qrimli HF, Kumar N. A Review of Application Industrial Robotic Design. In: 2011 Ninth International Conference on ICT and Knowledge Engineering; 2012. p. 105-12.

[8] Papadopoulos EG, Rey DA. A new measure of tipover stability margin for mobile manipulators. In: Proceedings of IEEE International Conference on Robotics and Automation. vol. 4; 1996. p. 3111-6 vol.4. ISSN: 1050-4729. Available from: https://ieeexplore.ieee.org/document/509185/.

[9] Webster C, Reid W. A Comparative Rover Mobility Evaluation for Traversing Permanently Shadowed Regions on the Moon. In: 2022 IEEE Aerospace

Conference (AERO); 2022. p. 1-15. ISSN: 1095-323X. Available from: https://ieeexplore.ieee.org/document/9843748/.

[10] Wilcox BH, Litwin T, Biesiadecki J, Matthews J, Heverly M, Morrison J, et al. Athlete: A cargo handling and manipulation robot for the moon. Journal of Field Robotics. 2007;24(5):421-34. _eprint: https://onlinelibrary.wiley.com/doi/pdf/10.1002/rob.20193. Available from: https://onlinelibrary.wiley.com/doi/abs/10.1002/rob.20193.

[11] Quan Y, Zhao C, Lv C, Wang K, Zhou Y. The Dexterity Capability Map for a Seven-Degree-of-Freedom Manipulator. Machines. 2022;10(11):1038.

[12] Medvid AY, Yakovyna VS. Estimation of Task-Specific Manipulability Scores for a Robotic Manipulator in Vacuuming Scenarios. Herald of Advanced Information Technology. 2025;8(4):434-46.

[13] McGhee RB, Frank AA. On the stability properties of quadruped creeping gaits. Mathematical Biosciences. 1968 Aug;3:331-51. Available from: https://www.sciencedirect.com/science/article/pii/0025556468900904.

[14] Yoshida E, Kanoun O, Esteves C, Laumond Jp. Task-driven Support Polygon Reshaping for Humanoids. In: 2006 6th IEEE-RAS International Conference on Humanoid Robots; 2006. p. 208-13. ISSN: 2164-0580. Available from: https://ieeexplore.ieee.org/abstract/document/4115603.

[15] Moosavian SAA, Alipour K. On the dynamic tip-over stability of wheeled mobile manipulators. International Journal of Robotics and Automation. 2007 Jan;22:322-8.

[16] Ding X, Liu Y, Hou J, Ma Q. Online Dynamic Tip-Over Avoidance for a Wheeled Mobile Manipulator With an Improved Tip-Over Moment Stability Criterion. IEEE Access. 2019;7:67632-45. Available from: https://ieeexplore.ieee.org/document/8709686/.

[17] Bretl T, Lall S. Testing Static Equilibrium for Legged Robots. IEEE Transactions on Robotics. 2008 Aug;24(4):794-807. Available from: https://ieeexplore.ieee.org/document/4598894/.

[18] Or Y, Rimon E. Geometric Characterization and Experimental Validation of Frictional 3-Contact Equilibrium Stances in Three-Dimensions. In: Proceedings 2007 IEEE International Conference on Robotics and Automation; 2007. p. 193-8. ISSN: 1050-4729. Available from: https://ieeexplore.ieee.org/document/4209091/.

[19] Mateo Sanguino TdJ. 50 years of rovers for planetary exploration: A retrospective review for future directions. Robotics and Autonomous Systems. 2017;94:172-85.

[20] NASA. Rover Components - Mars 2020 Perseverance Rover; 2020. Accessed: 2026-03-04. https://science.nasa.gov/mission/mars-2020-perseverance/rover-components/.

[21] Schenker PS, Huntsberger TL, Pirjanian P, Baumgartner ET, Tunstel E. Planetary rover developments supporting Mars exploration, sample return and future human-robotic colonization. Autonomous Robots. 2003;14(2):103-26.

[22] Verma V, Thiel E, Rankin A, Balabanska N, Maimone M, Rothenberger N, et al. Robotic Operations During Perseverance's First Extended Mission. In: 2025 IEEE Aerospace Conference. IEEE; 2025. .

[23] Verma V, Hartman F, Rankin A, Maimone M, Del Sesto T, Toupet O, et al. First 210 solar days of Mars 2020 Perseverance Robotic Operations – Mobility, Robotic Arm, Sampling, and Helicopter. In: 2022 IEEE Aerospace Conference (AERO). IEEE; 2022. .

[24] Toledo Fuentes A, Kipfmüller M, Burghart C, José Prieto MA, Bertram T, Bryga M, et al. Stable operation of arm type robots on mobile platforms. Procedia CIRP. 2021;99:104-9.

[25] Porges O, Lampariello R, Artigas J, Wedler A, Borst C, Roa MA. Reachability and Dexterity: Analysis and Applications for Space Robotics. In: Astra 2015. German Aerospace Center (DLR); 2015. .

[26] Porges O, Stouraitis T, Borst C, Roa MA. Reachability and Capability Analysis for Manipulation Tasks. In: ROBOT2013: First Iberian Robotics Conference. Springer; 2014. p. 703-18.

[27] Edelberg K, Wai D, Reid J, Kulczycki E, Backes P. Workspace and Reachability Analysis of a Robotic Arm for Sample Cache Retrieval from a Mars Rover. In: AIAA SPACE 2015 Conference and Exposition; 2015. .

[28] Cordes F, Oekermann C, Babu A, Kuehn D, Stark T, Kirchner F. An Active Suspension System for a Planetary Rover.

[29] Cordes F, Babu A. SherpaTT: A Versatile Hybrid Wheeled-Leg Rover.

[30] JPL Robotics: The ATHLETE Rover;. Available from: https://www-robotics.jpl.nasa.gov/how-we-do-it/systems/the-athlete-rover/?view=default.

[31] Wilcox BH, Litwin T, Biesiadecki J, Matthews J, Heverly M, Morrison J, et al. ATHLETE: A Cargo Handling and Manipulation Robot for the Moon. Journal of Field Robotics. 2007;24(5):421-34.

[32] GmbH D. Sherpa - Expandable Rover for Planetary Applications;. Available from: https://robotik.dfki-bremen.de/en/research/robot-systems/sherpa.

[33] Reid W, Paton M, Karumanchi S, Chamberlain-Simon B, Emanuel B, Meirion-Griffith G. Autonomous Navigation over Europa Analogue Terrain for an Actively Articulated Wheel-on-Limb Rover. In: 2020 IEEE/RSJ International Conference on Intelligent Robots and Systems (IROS); 2020. p. 1939-46. ISSN: 2153-0866. Available from: https://ieeexplore.ieee.org/document/9341234.

[34] Zhu B, He J, Gao F. Stiffness optimization design of wheeled-legged rover integrating active and passive compliance capabilities. Mechanism and Machine Theory. 2024 Nov;202:105758. Available from: https://www.sciencedirect.com/science/article/pii/S0094114X2400185X.

[35] Townsend J, Biesiadecki J, Collins C. ATHLETE mobility performance with active terrain compliance. In: 2010 IEEE Aerospace Conference; 2010. p. 1-7. ISSN: 1095-323X. Available from: https://ieeexplore.ieee.org/document/5446992/.

[36] Backes P, Diaz-Calderon A, Robinson M, Bajracharya M, Helmick D. Automated rover positioning and instrument placement. In: 2005 IEEE Aerospace Conference. Big Sky, MT, USA: IEEE; 2005. p. 60-71. Available from: http://ieeexplore.ieee.org/document/1559299/.

[37] Arm P, Waibel G, Preisig J, Tuna T, Zhou R, Bickel V, et al. Scientific Exploration of Challenging Planetary Analog Environments with a Team of Legged Robots. Science Robotics. 2023 Jul;8(80):eade9548. Available from: http://arxiv.org/abs/2307.10079.

[38] Belmonte-Baeza A, Cazorla M, García GJ, Pérez-Del-Pulgar CJ, Pomares J. Autonomous Legged Mobile Manipulation for Lunar Surface Operations via Constrained Reinforcement Learning. arXiv; 2025. Available from: http://arxiv.org/abs/2510.12684.

[39] Zhu X, Chen Y, Sun L, Niroui F, Le Cleac'h S, Wang J, et al. Versatile Loco-Manipulation through Flexible Interlimb Coordination. In: Proceedings of The 9th Conference on Robot Learning. PMLR; 2025. p. 610-32. Available from: https://proceedings.mlr.press/v305/zhu25a.html.

[40] Liu M, Chen Z, Cheng X, Ji Y, Qiu RZ, Yang R, et al.. Visual Whole-Body Control for Legged Loco-Manipulation. arXiv; 2024. Available from: http://arxiv.org/abs/2403.16967.

[41] Molnar L, Cheng J, Fadini G, Kang D, Zargarbashi F, Coros S. Whole-Body Inverse Dynamics MPC for Legged Loco-Manipulation. arXiv; 2025. Available from: http://arxiv.org/abs/2511.19709.

[42] Risiglione M, Abdalla A, Barasuol V, Ly KT, Havoutis I, Semini C. RAKOMO: Reachability-Aware K-Order Markov Path Optimization for Quadrupedal Loco-Manipulation. arXiv; 2025. Available from: http://arxiv.org/abs/2507.19652.

[43] Dadiotis I, Laurenzi A, Tsagarakis N. Whole-body MPC for highly redundant legged manipulators: experimental evaluation with a 37 DoF dual-arm quadruped. In: 2023 IEEE-RAS 22nd International Conference on Humanoid Robots (Humanoids); 2023. p. 1-8. Available from: http://arxiv.org/abs/2310.02907.

[44] Boston Dynamics. Spot Robot: Technical Specifications; 2024. https://bostondynamics.com/products/spot/.

[45] Boston Dynamics. Spot Arm Payload Specifications; 2024. https://bostondynamics.com/wp-content/uploads/2020/10/spot-arm.pdf.

[46] Schenker PS, Pirjanian P, Balaram B, Ali KS, Trebi-Ollennu A, Huntsberger TL, et al. Robot Manipulator Technologies for Planetary Exploration. Proceedings of SPIE. 1999;3839:180-91.

[47] Siciliano B, Sciavicco L, Villani L, Oriolo G. Robotics: Modelling, Planning and Control. London: Springer; 2008.

[48] Baumgartner ET, Bonitz RG, Melko JP, Shiraishi LR, Leger PC. The Mars Exploration Rover Instrument Positioning System. In: Proceedings of the IEEE Aerospace Conference. Big Sky, Montana: IEEE; 2005. p. 1-20.

[49] Billing R, Fleischner R, Sheridan S, et al. Mars Science Laboratory Robotic Arm. In: Proceedings of the 14th European Space Mechanisms and Tribology Symposium (ESMATS). Constance, Germany; 2011. p. 363-70.

[50] Trebi-Ollennu A, Baumgartner ET, Leger PC, Bonitz RG. Robotic Arm In-Situ Operations for the Mars Exploration Rovers Surface Mission. In: Proceedings of the IEEE International Conference on Systems, Man and Cybernetics. IEEE; 2005. p. 1799-806.

[51] Vago JL, Westall F, Pasteur Instrument Teams, et al. Habitability on Early Mars and the Search for Biosignatures with the ExoMars Rover. Astrobiology. 2017;17(6–7):471-510.

[52] Airbus Defence and Space. VISPA – Versatile In-Space and Planetary Arm; 2022. Accessed: 2026-03-06. https://www.airbus.com/en/newsroom/news/2022-05-in-space-manufacturing-and-assembly.

[53] Airbus Defence and Space. VISPA URDF – Unified Robot Description Format; 2022. Open-source, Apache 2.0 licence. Accessed: 2026-03-06. https://github.com/AirbusDefenceAndSpace/vispa.

[54] National Aeronautics and Space Administration. NASA's Lunar Exploration Program Overview. NASA; 2020. NP-2020-05-2853-HQ.

[55] Yoshikawa T. Manipulability of Robotic Mechanisms. The International Journal of Robotics Research. 1985;4(2):3-9.

[56] Backes P, Diaz-Calderon A, Robinson M, Bajracharya M, Helmick D. Automated Rover Positioning and Instrument Placement. In: Proceedings of the IEEE Aerospace Conference. Big Sky, Montana: IEEE; 2005. .

[57] Jet Propulsion Laboratory. Whole Rover–Arm Coordination; 2023. Accessed: 2026-02-26. https://www-robotics.jpl.nasa.gov/what-we-do/research-tasks/whole-rover-arm-coordination/.

[58] Rosenburg MA, Aharonson O, Head J, Kreslavsky M, Mazarico E, Neumann GA, et al. Global surface slopes and roughness of the Moon from the Lunar Orbiter Laser Altimeter. Journal of Geophysical Research: Planets. 2011;116(E2).

[59] Henriksen M, Manheim M, Burns K, Seymour P, Speyerer E, Deran A, et al. Extracting accurate and precise topography from LROC narrow angle camera stereo observations. Icarus. 2017;283:122-37.

[60] Adler I, Trombka J, Gerard J, Lowman P, Schmadebeck R, Blodget H, et al. Apollo 15 geochemical X-ray fluorescence experiment: Preliminary report. Science. 1972;175(4020):436-40.

[61] Diaz-Calderon A, Kelly A. On-Line Stability Margin and Attitude Estimation for Dynamic Articulating Mobile Robots. The International Journal of Robotics Research. 2005;24(10):845-66.

[62] Papadopoulos E, Rey DA. The Force-Angle Measure of Tipover Stability Margin for Mobile Manipulators. Vehicle System Dynamics. 2000 Jan;33(1):29-48. _eprint: https://www.tandfonline.com/doi/pdf/10.1076/0042-3114%28200001%2933%3A1%3B1-5%3BFT029. Available from: https://www.tandfonline.com/doi/abs/10.1076/0042-3114%28200001%2933%3A1%3B1-5%3BFT029.

[63] Xie Z, Li L, Luo X. A foot-ground interaction model based on contact stability optimization for legged robot. Journal of Mechanical Science and Technology. 2022 Feb;36(2):921-32. Available from: https://doi.org/10.1007/s12206-022-0139-1.

[64] Hendrik K, Manuel B, Christian G, Marco H. Scalability Analysis of Legged Robots for Space Exploration; 2017. .

[65] Zhu B, He J, Sun J. Kinematic modeling and hybrid motion planning for wheeled-legged rovers to traverse challenging terrains. Robotica. 2024 Jan;42(1):153-78. Available from: https://www.cambridge.org/core/journals/robotica/article/kinematic-modeling-and-hybrid-motion-planning-for-wheeledlegged-rovers-to-traverse-challenging-terrains/F608C7259FD9E8FEFE77115FBC213116.

[66] Boston Dynamics. Geometry and Frames; 2024. https://dev.bostondynamics.com/docs/concepts/geometry_and_frames.html.

[67] heuristicus/spot_ros contributors. Spot URDF Description Files; 2023. https://github.com/heuristicus/spot_ros.

[68] Boston Dynamics. Supplemental Data – Joint Control API; 2024. https://dev.bostondynamics.com/docs/concepts/joint_control/supplemental_data.html.

[69] Boston Dynamics. Arm Services; 2024. https://dev.bostondynamics.com/docs/concepts/arm/arm_services.html.

[70] Toupet O, et al . Curiosity Rover Mobility Trends During the First Seven Years. Journal of Field Robotics. 2020;37(8):1307-35. Copyright 2020 California Institute of Technology. U.S. Government sponsorship acknowledged.

[71] NASA - National Aeronautics and Space Administration. Curiosity Rover 3D Model; 2023. Accessed: 2026-03-26. NASA Science Resources. Available from: https://science.nasa.gov/resource/curiosity-rover-3d-model/.

Appendix A

Simulation Platform Functional Overview

The developed platform provides an integrated environment for large-scale evaluation of rover–manipulator systems. Its functionality is organised into several core modules, as summarised below.

A.1 Data Management

The platform provides an interactive data management interface for exploring large-scale simulation results.

- large-scale configuration datasets can be efficiently browsed and queried
- multi-dimensional filtering enables selection based on rover type, arm configuration, terrain condition, and evaluation outcomes
- algorithm strategies can be switched dynamically to compare reachability- and stability-oriented results
- filtered datasets can be exported for external analysis
- each configuration entry provides access to detailed visualisation, including 3D system representations

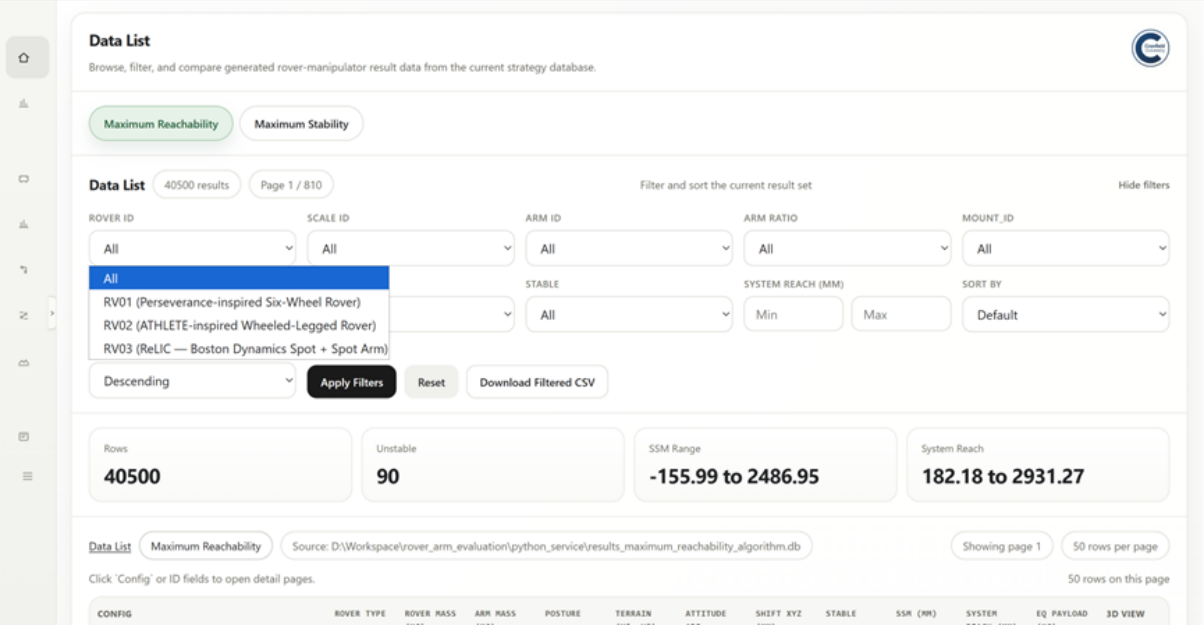

Figure A.1: Tabulated simulation results with multi-parameter attributes, including rover type, arm configuration, terrain condition, stability metrics, and reachability performance, enabling detailed inspection and comparison of configurations.

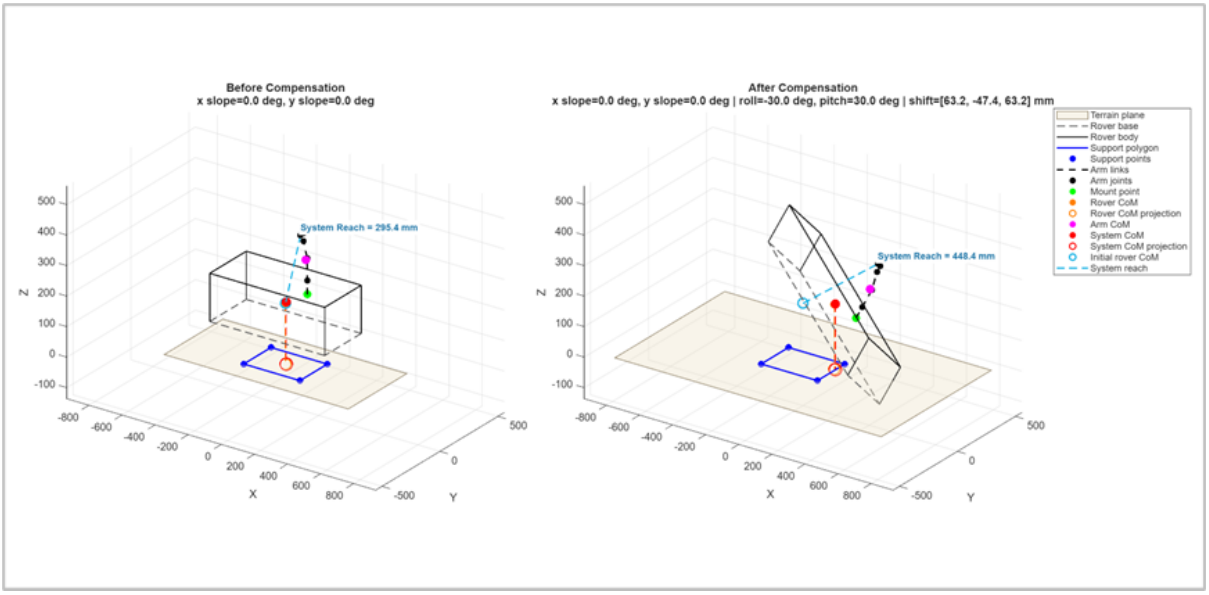

Figure A.2: Detailed configuration view of a selected rover–manipulator setup, presenting integrated system parameters, geometric properties, and evaluation results within a unified interface

A.2 Statistical Analysis

The platform provides integrated statistical analysis tools for interpreting large-scale simulation results and identifying key performance trends across rover–manipulator configurations.

- aggregated performance metrics are visualised across different system architectures to support comparative analysis
- terrain sensitivity analysis evaluates the impact of environmental conditions on system stability
- manipulator mass ratio sensitivity analysis quantifies the influence of arm scaling on performance
- reachability–stability trade-offs are analysed to identify optimal configuration regions
- MATLAB-generated analytical figures are integrated for interactive exploration

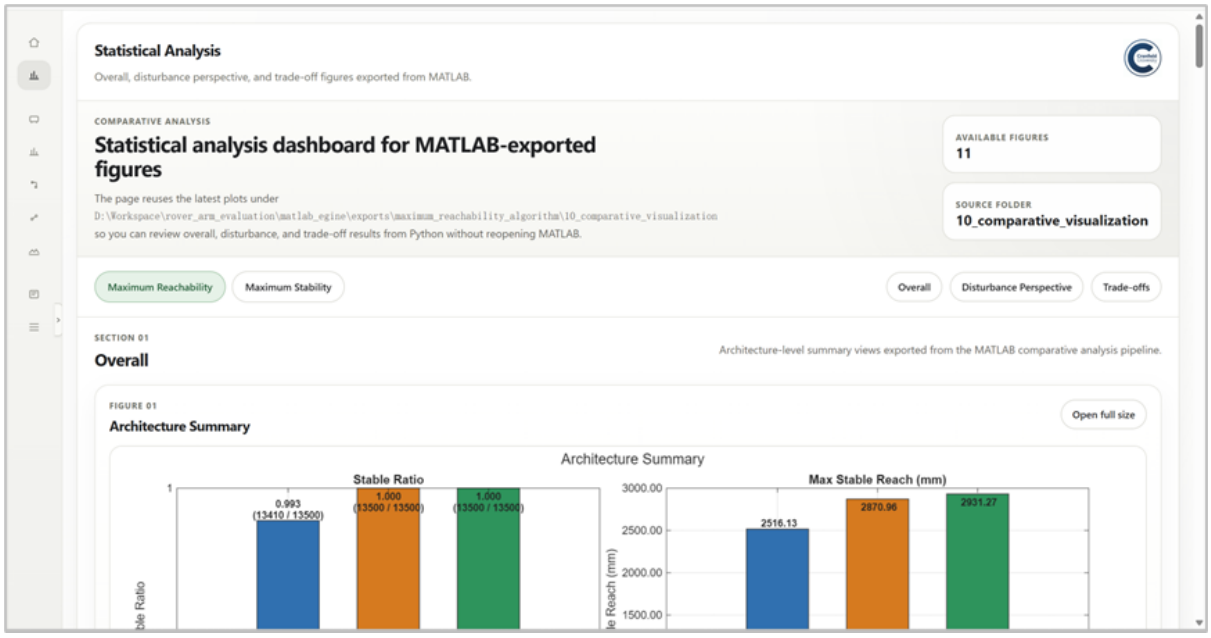

Figure A.3: Statistical analysis dashboard integrating MATLAB-generated results, providing aggregated performance comparisons across different rover–manipulator architectures.

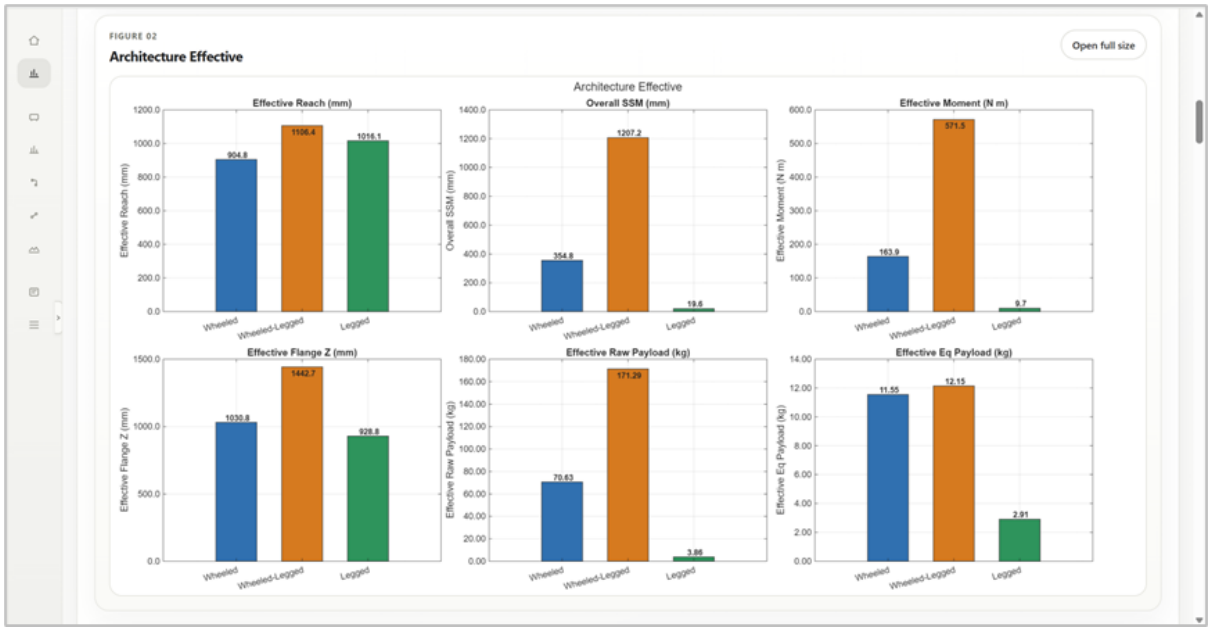

Figure A.4: Comparative evaluation of architecture performance metrics, including effective reach, stability, payload capacity, and moment, enabling quantitative assessment of different system designs

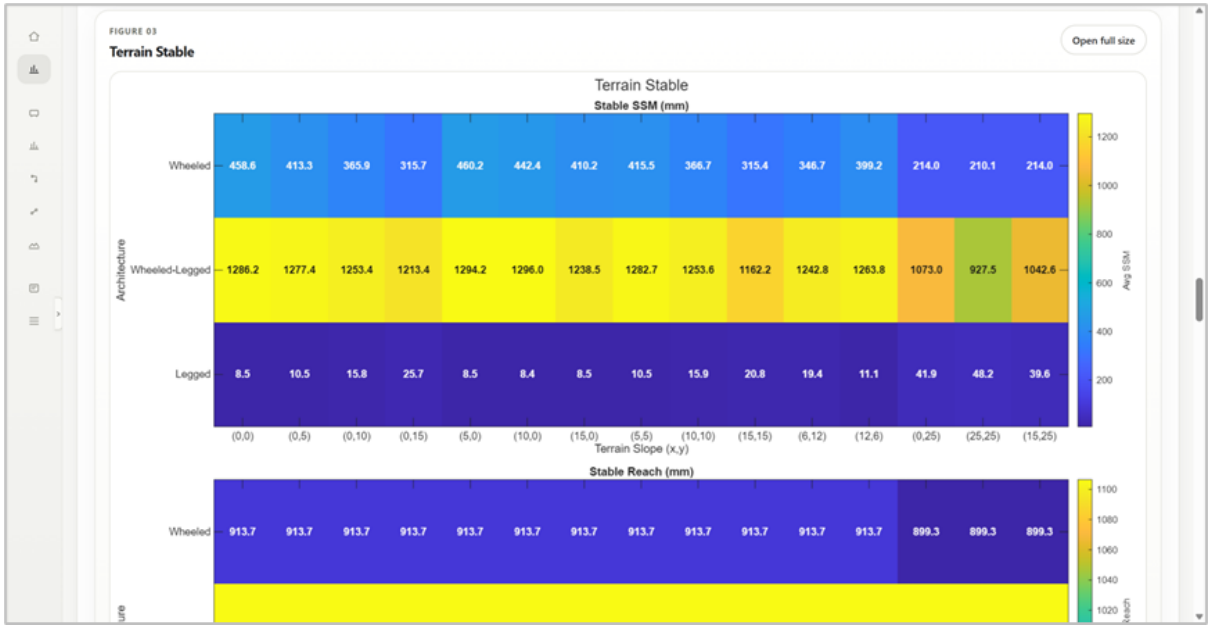

Figure A.5: Terrain sensitivity analysis showing stability variation across different slope conditions and rover mobility types, highlighting the impact of terrain inclination on system stability

A.3 Configuration Management

The configuration module defines a structured parameter space for systematic generation of rover–manipulator configurations, including geometry, scaling, and environmental

conditions.

A.3.1 Geometry Definition

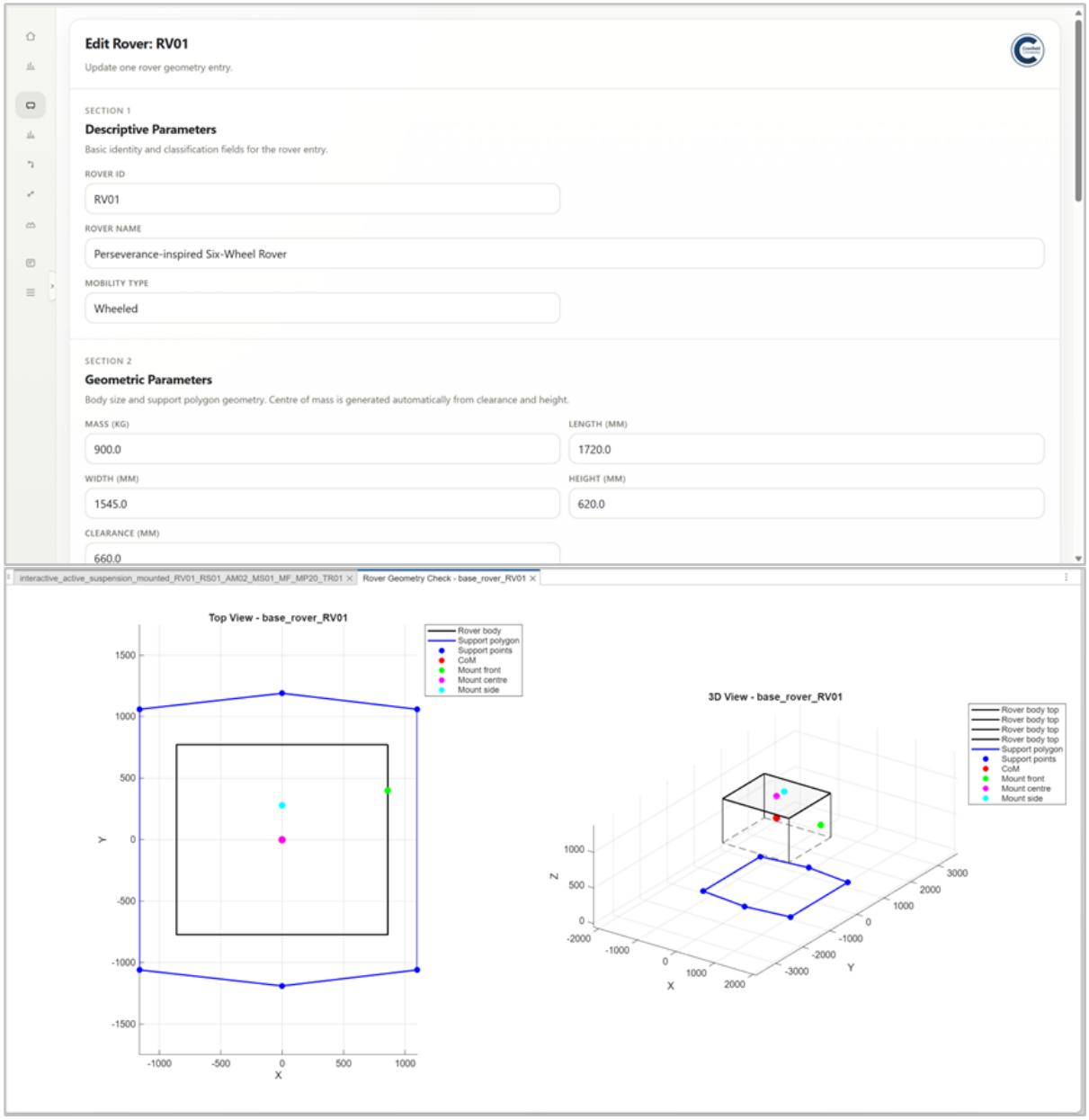

Figure A.6: Rover geometry definition interface and corresponding geometric validation visualisation, showing body dimensions, support polygon, and centre of mass representation in both top and 3D views

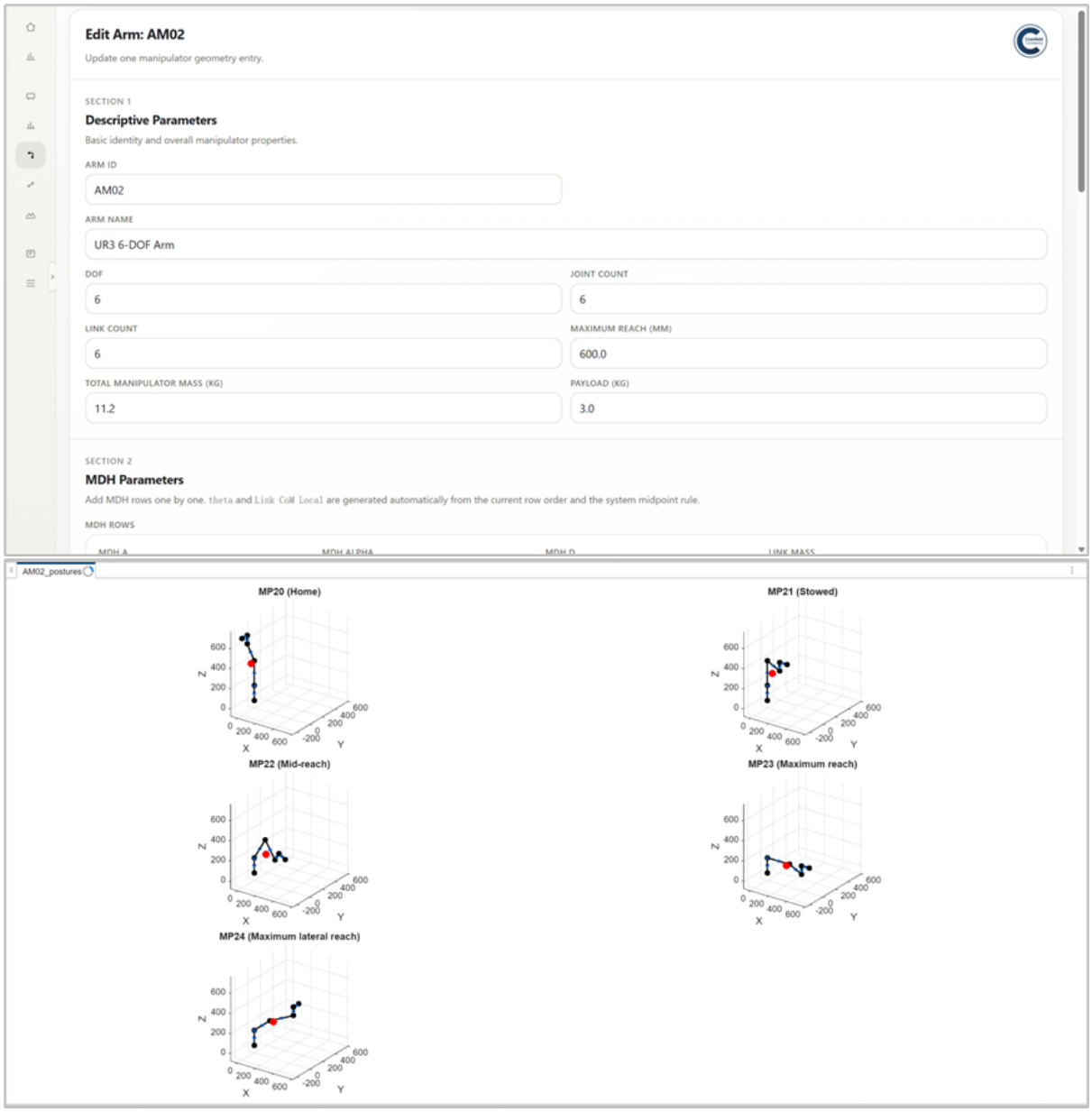

Figure A.7: Manipulator configuration interface and pose visualisations, illustrating multiple predefined arm configurations (e.g., home, stowed, and extended poses) used for reachability and stability evaluation

A.3.2 Scaling Mechanism

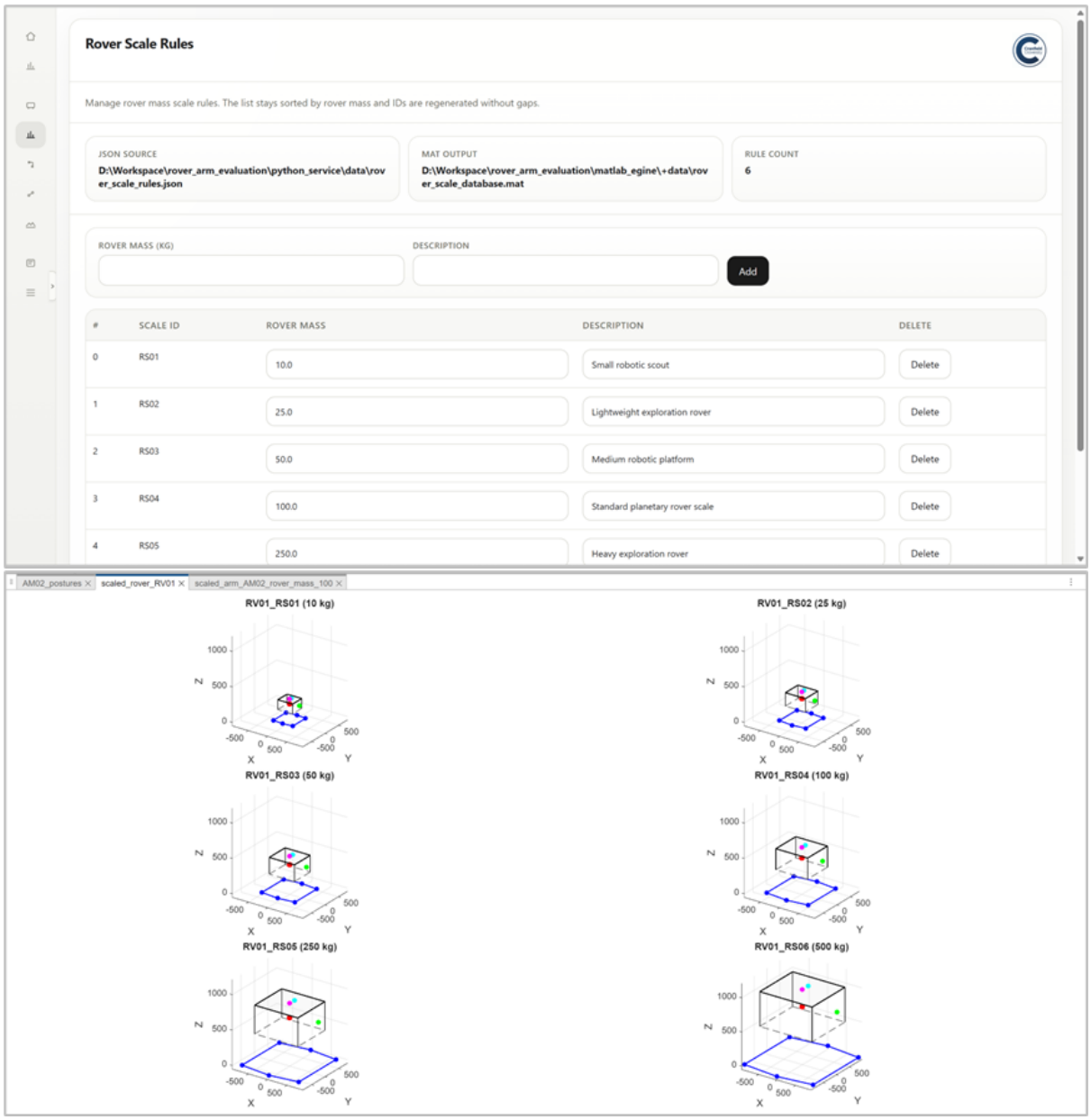

Figure A.8: Rover scaling mechanism and geometric effects. (a) Definition of rover mass scale rules; (b–g) resulting geometric configurations across different scale levels, illustrating variations in support polygon and centre of mass distribution

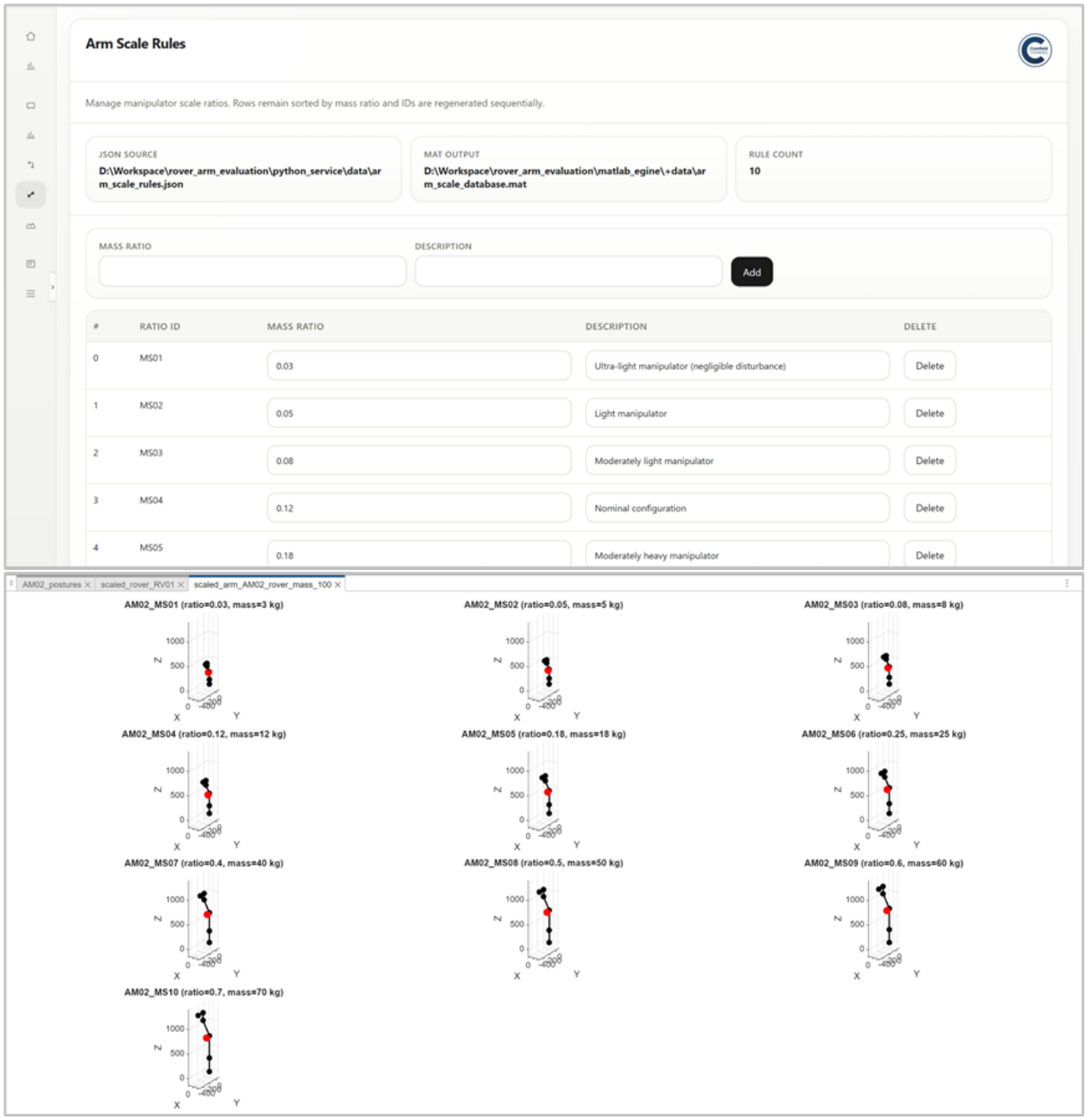

Figure A.9: Manipulator scaling mechanism based on mass ratio variation. (a) Definition of arm mass ratio rules; (b–h) corresponding manipulator configurations under different scaling conditions, demonstrating changes in kinematic structure and mass distribution

A.3.3 Environment and Posture Parameterisation

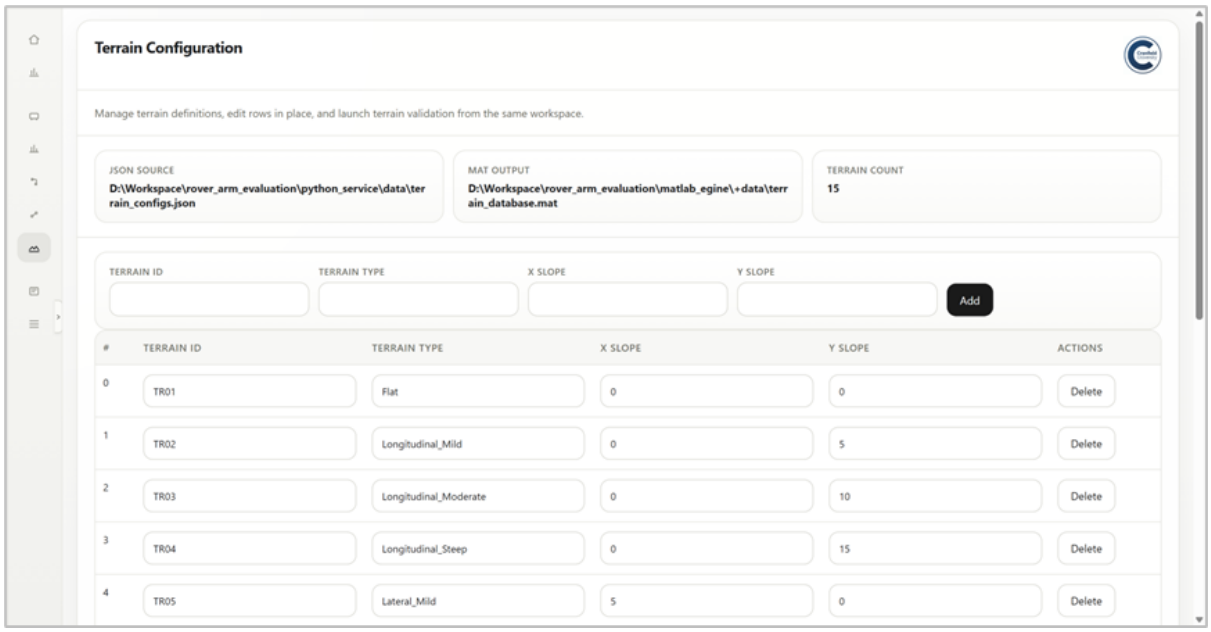

Figure A.10: Terrain configuration and 3D representation. (a) Terrain parameter definition interface specifying slope conditions; (b–j) resulting system configurations under varying terrain inclinations, illustrating the effect of slope on rover orientation and support geometry

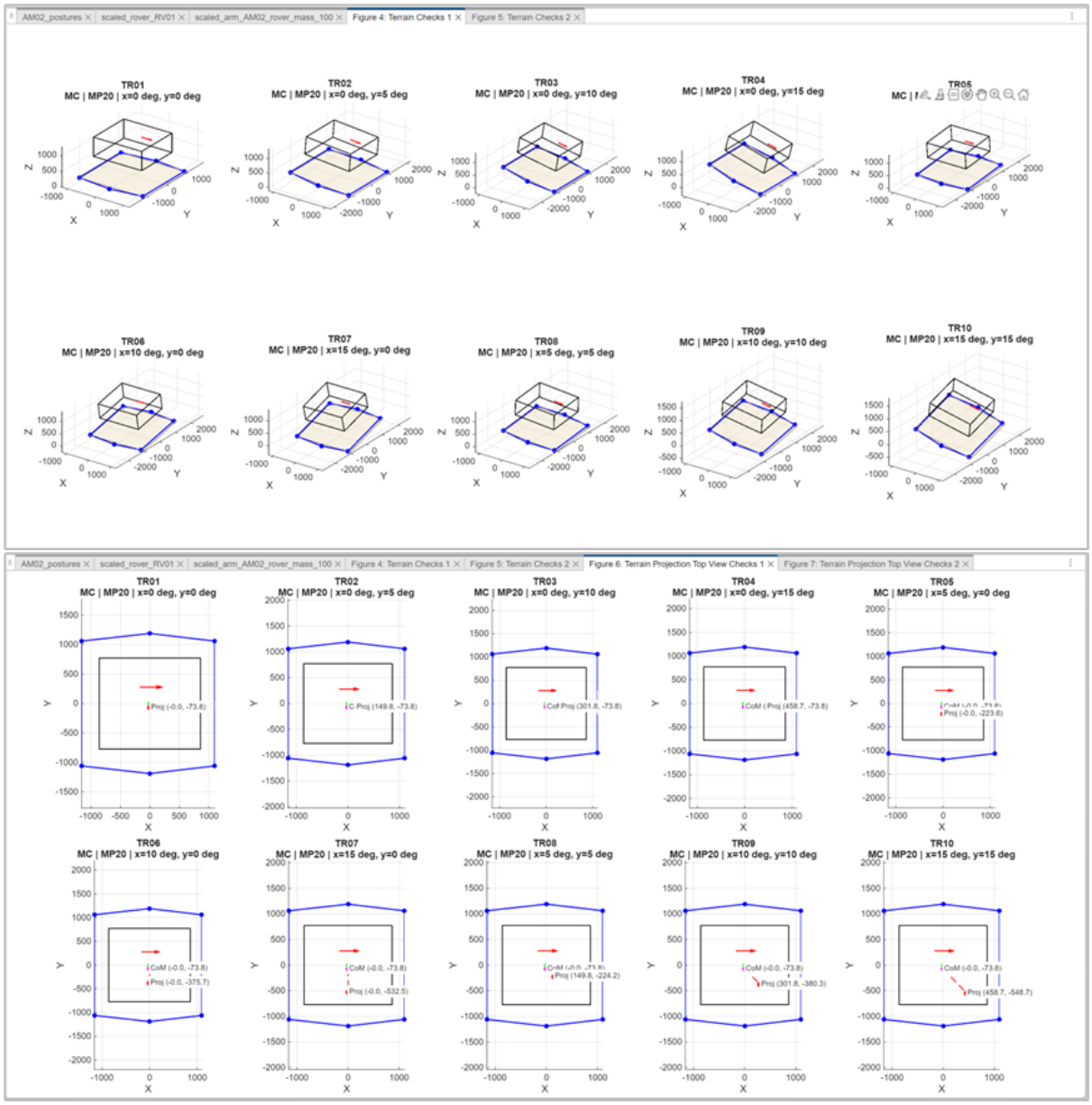

Figure A.11: Projection-based stability analysis under varying terrain conditions. Each subplot shows the centre of mass projection relative to the support polygon, highlighting stability variations across different slope configurations

A.4 Computational Engine

The computational engine orchestrates the execution of large-scale evaluation tasks through an integrated MATLAB-based analytical pipeline.

- configuration inputs are transformed into MATLAB-compatible parameters for simulation execution
- evaluation strategies can be adjusted through configurable algorithm parameters

- computation progress is monitored in real time, including execution stage and logging information
- simulation outputs are automatically processed and reconstructed into structured datasets
- analytical figures are generated and managed within the pipeline for subsequent statistical analysis

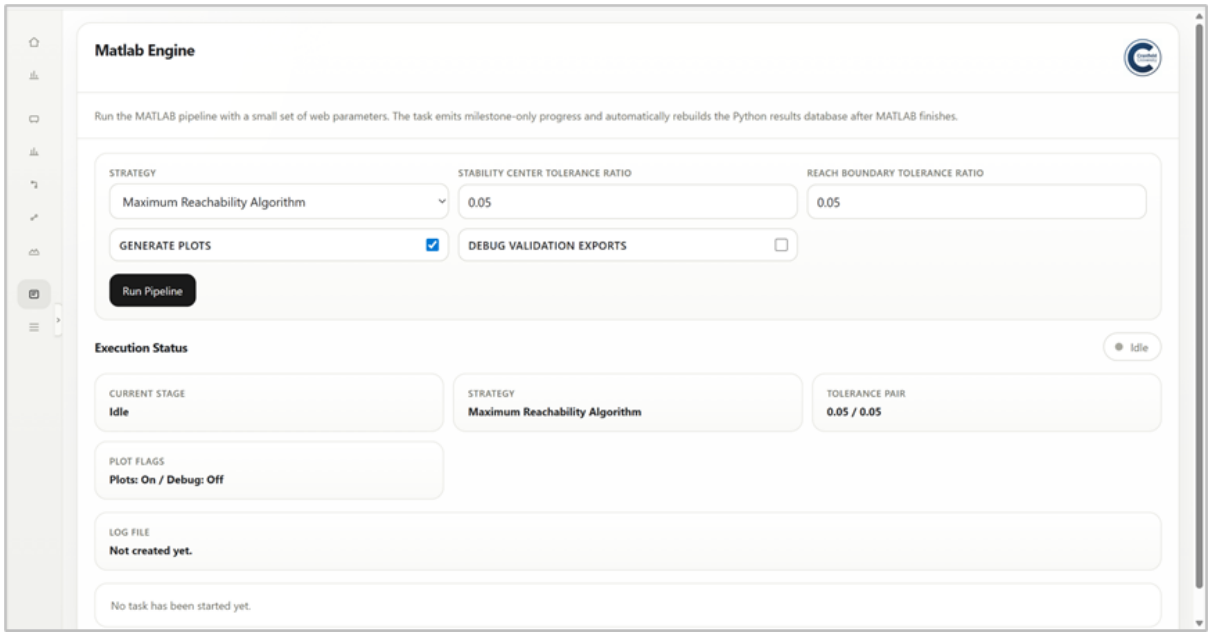

Figure A.12: Computational engine interface for executing the MATLAB-based evaluation pipeline, including strategy selection, parameter configuration, and real-time monitoring of computation status

A.5 System Integration

The platform integrates configuration generation, computational evaluation, and result visualisation into a unified workflow through coordinated data exchange between the Python interface and the MATLAB computational backend.

- configuration data are transformed into structured inputs compatible with the MATLAB evaluation pipeline
- bidirectional data flow enables seamless communication between the Python platform and MATLAB engine during execution and result retrieval
- multiple evaluation strategies are managed through consistent dataset structures, allowing direct comparison across different analytical approaches

- validation mechanisms ensure consistency and feasibility of configurations prior to computation
- batch processing supports large-scale evaluation of thousands of configurations in an automated manner

This integration enables an efficient end-to-end pipeline from configuration definition to performance evaluation and analytical visualisation.

Appendix B

Platform Testing Report

B.1 Testing Overview

The platform was functionally evaluated to assess its reliability and consistency in supporting configuration management and data interaction. The testing process aimed to verify core interaction workflows and identify potential inconsistencies across modules.

The validation covered three aspects: system structure exploration, representative functional testing, and cross-page behaviour consistency.

B.2 System Structure Discovery

The platform was explored to identify its primary functional modules, including configuration management, data querying, and analysis interfaces. Each module was examined for the presence of editable fields, input forms, and interactive controls.

The results confirm that the platform provides a structured and modular interface, enabling consistent interaction across different functional pages.

B.3 Representative Functional Validation

Representative configuration modules were selected to validate core interaction workflows, including parameter editing, data submission, and result retrieval.

Editing operations were successfully performed across multiple parameters, with updated values correctly reflected in subsequent queries. Different query modes, including ID-based search and general filtering, produced consistent and valid results.

These observations confirm the correctness of the editing–submission–persistence workflow and demonstrate stable behaviour across configuration modules.

B.4 Cross-Page Behaviour Analysis

Across all tested modules, the platform exhibits a consistent interaction pattern characterised by structured input submission, immediate data update, and predictable query–response behaviour.

This unified interaction model enhances system reliability and usability, ensuring consistent user experience across different functional components.

B.5 Validation Summary

The conducted validation confirms that the developed platform provides stable and consistent functionality for configuration management and data interaction. Core workflows, including parameter editing, data submission, and query execution, were verified to operate correctly across representative modules.

The platform exhibits a unified interaction pattern across different functional pages, ensuring predictable system responses and consistent data persistence. No critical inconsistencies or functional failures were identified during the testing process.

Overall, the results indicate that the platform is functionally reliable and suitable for supporting large-scale configuration exploration and analysis within the proposed framework. Further validation of advanced functionalities and edge cases remains part of ongoing development.

B.6 Limitations and Ongoing Work

While the testing confirms the functional stability of core modules, several aspects require further investigation, including extended validation of additional modules, integration-level testing, and robustness under complex workflows.

These areas are identified as part of ongoing development and future validation efforts.

B.7 Supporting Materials

A representative snapshot of the testing output is provided in Fig. B.1 to illustrate the validation process and confirm the execution of functional testing. Full testing logs are omitted for brevity.

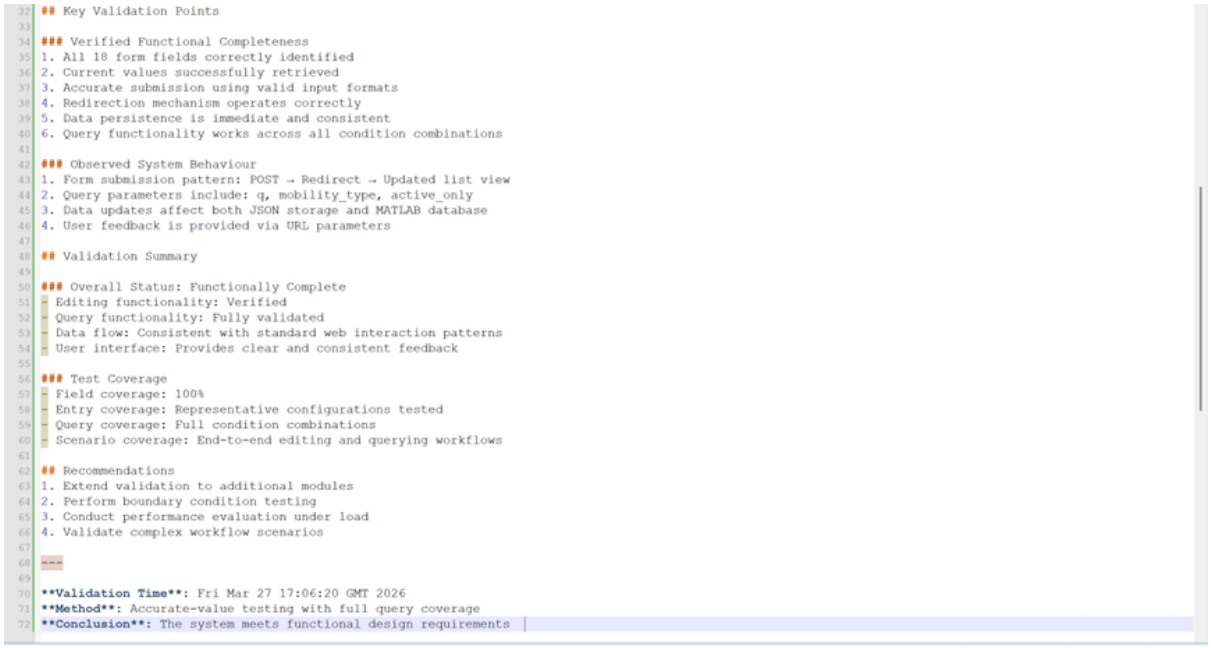

```
## Key Validation Points

### Verified Functional Completeness
1. All 18 form fields correctly identified
2. Current values successfully retrieved
3. Accurate submission using valid input formats
4. Redirection mechanism operates correctly
5. Data persistence is immediate and consistent
6. Query functionality works across all condition combinations

### Observed System Behaviour
1. Form submission pattern: POST → Redirect → Updated list view
2. Query parameters include: q, mobility_type, active_only
3. Data updates affect both JSON storage and MATLAB database
4. User feedback is provided via URL parameters

## Validation Summary

### Overall Status: Functionally Complete
- Editing functionality: Verified
- Query functionality: Fully validated
- Data flow: Consistent with standard web interaction patterns
- User interface: Provides clear and consistent feedback

### Test Coverage
- Field coverage: 100%
- Entry coverage: Representative configurations tested
- Query coverage: Full condition combinations
- Scenario coverage: End-to-end editing and querying workflows

## Recommendations
1. Extend validation to additional modules
2. Perform boundary condition testing
3. Conduct performance evaluation under load
4. Validate complex workflow scenarios

---

**Validation Time**: Fri Mar 27 17:06:20 GMT 2026
**Method**: Accurate-value testing with full query coverage
**Conclusion**: The system meets functional design requirements
```

Figure B.1: Representative snapshot of the functional testing output, provided as evidence of the validation process covering configuration editing, query operations, and system behaviour

Appendix C

Ethical Approval Letter

25 February 2026

Dear Lt Guimaraes Correa ,

Reference: CURES/27247/2026
Project ID: 30741
Title: Whole rover-arm manipulation for increased reachability

We are pleased to inform you that you have successfully declared that your research project is a **Literature Review – based solely on openly available literature which is in the public domain, and you are undertaking desk-based research not involving any other form of data or information.**

You have also confirmed that your project **does not meet** any of the literature review specified exceptions, listed both within the relevant section of the CURES form and below:

1) Your supervisor has requested that you apply for approval through CURES because:

- The journals or data are in a sensitive area (please discuss this with your supervisor)
- The project will be embargoed **i.e. will not be publicly available via the Cranfield library immediately or longer term**

2) Approval is/will be specifically required by another external body e.g. journal publishers

Therefore, **you do not require ethical approval** and your CURES application will be automatically closed.

Please keep a copy of this letter safe, if this exception is in relation to your thesis project, you will need to include a copy with your final thesis submission.

If you have any queries, please contact CURES Support.

We wish you every success with your project.

Regards,

CURES Team